

Acid-Stable
Electrocatalysts for the
Solar Production of Fuels

Thesis by
Fadl Hussein Saadi

In Partial Fulfillment of the Requirements for
the degree of
Doctor of Philosophy

The logo for the California Institute of Technology (Caltech), featuring the word "Caltech" in a bold, orange, sans-serif font.

CALIFORNIA INSTITUTE OF TECHNOLOGY
Pasadena, California

2017
(Defended January 12, 2017)

© 2017

Fadl Hussein Saadi
ORCID: 0000-0003-3941-0464

ACKNOWLEDGEMENTS

The number of people I need to thank for helping me get here is immense. I have never been a solitary figure and the warmth and aid that so many people have shown me is, quite honestly, breathtaking.

I want to start off by thanking my committee: Harry Atwater, Harry Gray and Bill Goddard. You have been so helpful during my time here at Caltech. I know you are all very busy and I appreciate your willingness to be a part of my committee. I also want to thank you all for running such amazing research groups. Members of all of your groups have aided me during my time at Caltech and for that I am grateful. I also want to thank Harry Gray for leading the Solar Army. I very much enjoyed working with you, Michelle DeBoever and Siddharth Dasgupta, to help motivate high school students' interest in scientific research.

I have been blessed, even before joining Caltech with amazing mentors. Thank you Tom Jaramillo and Zhebo Chen for helping a naïve sophomore understand why three electrodes are better than two and for giving me ownership of my own project. I still remember both the frustration and exhilaration of having my first research project.

I had some great mentors at Caltech, which included Carl Koval, who was the Director of JCAP throughout much of my time at Caltech and whose open door policy I took advantage of. Thank you for all the effort you put into creating a friendly, scientific

atmosphere here at JCAP. Bruce Brunshwig, director of the MMRC, was also always there when I needed him and has a way of making sure everything runs smoothly both inside the MMRC and outside of it.

I would like to thank my officemates: Jack Baricuatro, Kyle Cummins, Alnald Javier, Youn-Geun Kim, Jean Sanabria Chinchilla, Guofeng Sun, Brian Chmielowiec, Dan Torelli and Chu Tsang for always being happy to see me even though they knew that it meant the productivity in the office was going to plummet for a few minutes. I want to especially thank Jack and Kyle, who were so generous with their time. Jack, your chemistry knowledge is something that inspires me to this day– thank you for walking me through so many diverse scientific concepts. Kyle, your help with UHV systems has been amazing. I truly doubt you can find more than a handful of people in this world with more extensive knowledge about these systems.

The Lewis group is unique in many ways. I don't think my time at Caltech would have been nearly as enjoyable had I not ended up in such a smart, silly and cohesive group. When I first joined I remember looking up to the senior members of the group: Leslie O'Leary, Emily Warren, Liz Santori, Ron Grimm, Bryce Sadtler, Rob Coridan, Craig Wiggernhorn, Shane Ardo, Josh Spurgeon, James McKone, Joseph Beardslee and Nick Strandwitz; and being astounded that they could follow and contribute to the various types of research being presented and have strived to follow in their footsteps. I was also fortunate enough to work with the graduate students in the years above me: Josh Wiensch,

Adam Nielander, Chris Roske, Amanda Shing, Adam Pietrick and Matt Shaner. Thank you for all your help and maintaining so many of the instruments that I have used during my time at Caltech! My year saw a large influx of graduate students joining the Lewis group with Noah Plymale, Azhar Carim, Micheal Lichterman, Nick Batara and Victoria Dix and I all joining the group and, as luck would have it, becoming good friends! The graduate students the years below us have also been fantastic and an absolute pleasure to work with. Thanks Pai Buabthong, Chance Crompton, Jingjing Jiang, Paul Kempler, Kyra Lee, Ivan Moreno, Paul Nunez, Stefan Omelchenko, Katherine Rinaldi, Jared Bruce, Billy Hale, Roc Montserrat, Ethan Simonoff, Annelise Thompson, Dan Torelli, Jonathan Thompson, Sisir Yalamanchili, Ellen Yan, Katie Hamann, Mike Mazza, Harold Fu, Weilai Yu and Xinghao Zhou! There were also a good number of post docs who joined the group and enriched it with their wisdom. Thanks James Blakemore, Mita Dasog, Betar Gallant, Sonja Francis, Shu Hu, Teddy Huang, Jimmy John, CX Xiang, Mike Walter, Qixi Mi, Miguel Caban-Acevedo, Carlos Read, Matthias Richter, Ke Sun and Matt McDowell. I also want to thank Barbara Miralles, Rena Becerra-Rasti and Kimberly Papadantonakis for keeping the Lewis group humming along. It would be a mess without you!

I want to take a moment to especially thank Azhar who was always thrilled to have people over— watching college football is going to be decidedly less fun next year. Grabbing coffee and trying our hand at sous vide along with Mike, Ethan and Jonathon were some of the highlights of this past year. I also want to thank Dan, Stefan, Kyra,

Adam, Kat, Sonja, Annelise and Paul for cheering me up when I was down. That goofy grin of mine whenever I spotted you guys sitting at your desks was always genuine.

I also wish to thank my Materials Science cohort. Getting through those classes in our first year was not easy but we soldiered on as a group and got through it together. Even after our first year, it has always been a comfort knowing that at noon there would be a lunch table with friendly, familiar faces that would be more than happy to chat about whatever topic popped up. In particular, I want to thank Renee McVay, Sam Johnson, Kevin Fiedler, Max Jones, Sunita Darbe, Andrew Hoff, Eric Verlage, Mark Harfouche, Ivan Papusha, Evan Miyazono and John Lloyd. Our lunch conversations were sometimes serious, often silly and always a great joy. I also want to thank Christy Jenstad for helping me navigate the bureaucracy of Caltech and always offering a couch where I plop down and grab some candy. Additionally I want to thank David Chen, Dennis Kim, Karthik Seetharaman and Anandh Swaminathan for grabbing (often really late) dinners and driving around LA looking for good Indian food.

I was thrilled to have the opportunity to spend several months at the Dow Centre for Sustainable Innovation at the University of Queensland in Australia where I was got to dabble with the techno-economic analysis of different energy systems. I was only able to accomplish this due to the generosity of Eric McFarland, Professor at UCSB, who invited me and mentored me during my time there and afterwards. I also want to thank Julia Mueller, Tom McConnaughy, Diego Lopez, Xiaoyu Wang, Sara Zadeh, Brett Parkinson,

Simon Smart, Callum Hickey, Celestien Warnaar-Notschaele, Khuong Vuong, Mojgan Zavareh and Leila Safavi-Tehrani for creating a fun office atmosphere and reminding me of many of the chemical engineering topics that I had forgotten.

Since moving to LA, a lot of my free time has been spent watching and performing improv with some of the smartest and most interesting people I know. I want to thank my two improv teams Direct to Video (Scott Tammel, Sasha Feiler, Sean Kearney, Will Saunders, Steven Cohen, Doug Schultheis and Trevor Rotenburg) and The Scoop (Jen Kleinrock, Joseph Gehart, Gregory Smith, Patrick Ehlers, Ryan Mogge, Heather Sundell, Rebecca Landman and Kristel Kovner) for providing me with a safe space for my creativity even when it often bordered close to insanity.

Ramya Parameswaran, Shashank Ravi and Pedro Hernandez: thank you for all your help in those chemical engineering classes throughout our time at Stanford and for remaining my close friends. I must also give a very special thanks to the Noe Crew: Khaled Al-Turkestani, Ziyad AbdelKhaleq, Lily Guo, Mohammad Islam, Noor Alnabelseya and Andres Morales. Even though I flew up to the Bay quite often you guys always welcomed me with open arms and multiple couches to sleep on and made me feel special. Just hanging out with you guys brings me joy. Here's to a hundred more Thanksgivings!

During my time at Caltech I had one official advisor but was blessed to have an unofficial one as well. To my unofficial advisor, Manny Soriaga, Professor Emeritus at Texas A&M and Research Professor at Caltech: thank you for taking me under your wing

and treating me like I was one of your own students— your mentorship and kindness have been invaluable. When things weren't working and I needed a second opinion I knew I could knock on your door and you would be more than willing to try and figure out what is happening in my experiments. My official advisor, and why I joined Caltech in the first place, has been Nate Lewis. Nate thank you so much for everything you have done for me - I couldn't have asked for a more supportive advisor. Thank you for giving me the academic freedom to try so many different projects and for cultivating a truly unique group culture. In the Lewis group we like to joke that we have a hard time relating to other graduate students because we rarely encounter the difficulties they do. We really appreciate the work you put into making that a reality.

Finally, I need to thank my family: Mom, Dad, Sarah and Ahmad. It's been really hard living so far away from you but your love and support easily traverses the thousands of miles between us. To my dearest Sarah: thank you for being my closest friend from literally day one- I'm so fortunate to have you as my twin. I wish everyone had a twin like you. Ahmad: I am so proud of you. You might not know this, but one of my favorite pastimes is bragging to my friends about how amazing a brother you are. Mom, Dad your support and encouragement is what gives me the strength and motivation to keep going. You are, and always have been, my inspiration. While I am proud of the work that I've done, my biggest source of pride will forever and always be being your son.

ABSTRACT

Sunlight is one of the few renewable resources that can meet global energy demand. Unfortunately, while solar energy has grown in the past few years, several economic and scientific constraints have hindered mass adoption. One of the main obstacles solar energy faces is the lack of economically competitive storage technologies. Artificial photosynthesis is a potential solution in which solar energy is directly converted into energy dense chemical bonds that can be easily stored and transported.

One impediment facing the commercialization of artificial photosynthesis is the use of expensive and rare precious metals as catalysts. This dissertation focuses on the achievements of the past five years in characterizing novel, earth-abundant, acid-stable hydrogen evolution catalysts. While nickel alloys have long been known as catalysts for the hydrogen evolution reaction in basic media, it has only been in the past decade that earth abundant catalysts that are stable in acidic media have been reported. These discoveries are critically important as the many proposed artificial photosynthetic devices require the use of acidic media.

In this dissertation we examine two families of hydrogen evolution catalysts: transition metal chalcogenides (namely molybdenum and cobalt selenide) as well as transition metal phosphides (cobalt phosphide). In addition to the electrochemical characterization of these catalysts, spectroscopic characterizations were performed in order to carefully

examine the chemical compositions of these catalysts before, after and during the hydrogen evolution reaction. This analysis elucidated both chemical, and structural changes that occurred after the catalysts had been subject to the hydrogen evolution reaction conditions.

The final chapter in this thesis delves into the techno-economic realities of energy transportation via different fuels. Due to the strong interest in renewable energy, several future energy transportation scenarios, including 100% grid electrification and widespread installation of hydrogen pipelines, have been proposed. In order to get a fuller understanding of such potential infrastructure alternatives, we report their differing energy transportation costs.

PUBLISHED CONTENT AND CONTRIBUTIONS

Saadi, F. H.; Carim, A. I.; Velazquez, J. M.; Baricuatro, J. H.; McCrory, C. C.; Soriaga, M. P.; Lewis, N. S. *ACS Catalysis* **2014**, *4*, 2866. DOI: <http://10.1021/cs500412u>

F.H.S participated in the conception of the project, performed the sample preparation, collected the majority of the data, performed the data analysis, and participated in writing the manuscript.

Carim, A. I.; **Saadi, F. H.**; Soriaga, M. P.; Lewis, N. S. *Journal of Materials Chemistry A* **2014**, *2*, 13835. DOI: 10.1039/C4TA02611J

F.H.S participated in the conception of the project, collected some of the data, performed data analysis, and participated in writing the manuscript.

Saadi, F. H.; Carim, A. I.; Verlage, E.; Hemminger, J. C.; Lewis, N. S.; Soriaga, M. P. *The Journal of Physical Chemistry C* **2014**, *118*, 29294. DOI: 10.1021/jp5054452

F.H.S participated in the conception of the project, performed the sample preparation, collected the majority of the data, performed the data analysis, and participated in writing the manuscript.

TABLE OF CONTENTS

Acknowledgements.....	iii
Abstract	ix
Published Content and Contributions.....	xi
Table of Contents.....	xii
List of Figures.....	xvi
List of Tables.....	xxiv
 Chapter 1: Introduction: Global Warming, Energy, and Artificial Photosynthesis	
1.1 Energy and the Climate	2
1.1.1 Global Energy Consumption	2
1.1.2 Carbon Dioxide Emission.....	4
1.1.3 Global Climate Change	6
1.2 Breaking the Energy & CO₂ Emission Bond	7
1.2.1 Carbon Capture and Storage (CCS)	7
1.2.2 Hydropower	8
1.2.3 Nuclear Fission	9
1.2.4 Wind Power	10
1.2.5 Photovoltaic Cells.....	11

1.2.6 Concentrated Solar Thermal.....	12
1.3 Artificial Photosynthesis	12
1.4 References	15
Chapter 2: Operando Synthesis of Macroporous Molybdenum Diselenide Films for the Hydrogen Evolution Reaction	18
2.1 Introduction and Motivation	18
2.2 Results.....	19
2.2.1 Characterization of as-deposited films	19
2.2.2 Conversion of the films to catalysts of the HER	30
2.3 Discussion	33
2.4 Conclusion	35
2.5 Experimental.....	36
2.6 References	42
Chapter 3: Electrocatalysis of the Hydrogen Evolution Reaction by Electrodeposited Amorphous Cobalt Selenide Films	46
3.1 Introduction	46
3.2 Cobalt selenide electrodeposition and characterization	47
3.3 Comparison with other HER Catalysts.....	54
3.4 Conclusion	55
3.5 Experimental.....	56
3.6 References	60

Chapter 4: CoP as an Acid-Stable Active Electrocatalyst for The Hydrogen-Evolution Reaction: Electrochemical Synthesis, Interfacial Characterization, and Performance Evaluation.....	63
4.1 Introduction	63
4.2 Cobalt phosphide electrodeposition and characterization	64
4.2.1 Characterization of films prior to electrocatalysis.....	64
4.2.2 Electrochemistry	68
4.2.3 Post-electrochemistry film characterization	70
4.3 Discussion	71
4.4 Conclusion	73
4.5 Experimental.....	74
4.6 References	78
Chapter 5: Operando Spectroscopic Analysis of CoP Films Electrocatalyzing the Hydrogen-Evolution Reaction	84
5.1 Introduction and Motivation	84
5.2 Characterization of CoP films.....	84
5.2.1 Potentiostatic and ex-situ characterization of CoP films.....	84
5.3 Conclusion	94
5.4 Experimental.....	95
5.5 References	100
Chapter 6: Costs of Transporting Electrical and Chemical Energy	102

6.1	Introduction	102
6.2	Costs of Energy Transport	104
6.2.1	Oil Pipelines	104
6.2.2	Natural Gas Pipelines	106
6.2.3	Hydrogen Pipelines	107
6.2.4	Pipelines for Alternative Chemicals	108
6.2.5	Oil Tankers	109
6.2.6	Liquefied Natural Gas Tankers	110
6.2.7	Electrical Transmission Lines	111
6.3	Overall Comparison, Comment, and Conclusion.....	113
6.4	References	115
	Publications.....	119

LIST OF FIGURES

FIGURE 1.1: WORLD TOTAL PRIMARY ENERGY SUPPLY (TPES) FROM 1971 TO 2014 BY FUEL (MTOE). ¹ © OECD/IEA 2016 KEY WORLD STATISTICS, IEA PUBLISHING. LICENSE: WWW.IEA.ORG/T&C	2
FIGURE 1.2: WORLD ELECTRICITY GENERATION FROM 1971 TO 2014 BY FUEL (TWH). ¹ © OECD/IEA 2016 KEY WORLD STATISTICS, IEA PUBLISHING. LICENSE: WWW.IEA.ORG/T&C	3
FIGURE 1.3: ANNUAL GLOBAL CARBON DIOXIDE EMISSIONS FROM 1965 TO 2014 (MILLION TONNES CO ₂). ⁶	4
FIGURE 1.4: MONTHLY MEAN ATMOSPHERIC CARBON DIOXIDE AT MAUNA LOA OBSERVATORY, HAWAII. PUBLICALLY AVAILABLE FROM NOAA. ⁹	5
FIGURE 1.5: ANOMALIES OF THE GLOBAL TEMPERATURE INDEX OF PROVIDED BY SEVERAL GROUPS IS DEPICTED FOR THE 1980 TO PRESENT TIME PERIOD. THE BASE PERIOD IS 1951-1980. THE BERKELEY BASELINE IS DEPICTED. PUBLICALLY AVAILABLE FROM THE BEST REPORT. ¹¹	6
FIGURE 1.6: HYDROELECTRICITY GENERATION IN TWH FROM 1965-2011. ¹³	9
FIGURE 1.7: NUCLEAR ENERGY GENERATION FROM 1965-2014 (TERRAWATT-HOURS). ⁶ ..	10
FIGURE 1.8: GLOBAL SOLAR PHOTOVOLTAIC GENERATION CAPACITY (GW). ⁶	11

FIGURE 2.1: SCANNING ELECTRON MICROGRAPHS OF THE FILMS BEFORE (A,B) AND AFTER (C,D) 10 CYCLES. (A) THE AS-DEPOSITED MIXED-COMPOSITION FILMS ON GLASSY CARBON SUBSTRATES WERE NON-UNIFORM, CONSISTING OF MULTIPLE ISLANDS ~ 100 μ M IN DIAMETER. (B) THE SURFACES OF THE ISLANDS WERE RELATIVELY SMOOTH. (C) THE ISLAND STRUCTURE WAS NOT VISIBLE AFTER ELECTROCATALYSIS, AND (D) AT HIGHER MAGNIFICATION THE ENTIRE SURFACE APPEARED POROUS. 21

FIGURE 2.2: HIGH-RESOLUTION X-RAY PHOTOELECTRON SPECTRA OF (A) THE Mo 3D REGION OF AN AS-DEPOSITED THIN FILM; (B) THE Se 3D REGION OF AN AS-DEPOSITED THIN FILM; (C) THE Mo 3D REGION AFTER 10 CYCLES; (D) THE Se 3D REGION AFTER 10 CYCLES. 24

FIGURE 2.3: HIGH-RESOLUTION X-RAY PHOTOELECTRON SPECTRA OF (A) THE Mo 3D REGION OF MoO₃; (B) THE O 1s REGION OF MoO₃; (C) THE Mo 3D REGION OF MoO₂; (D) THE O 1s REGION OF MoO₂; (E) THE O 1s REGION OF THE AS DEPOSITED FILM; (F) THE O 1s REGION AFTER 10 CYCLES. 25

FIGURE 2.4: RAMAN SPECTRA OF AN AS-DEPOSITED THIN FILM (SOLID) AND OF A FILM AFTER TEN CYCLES (DASHED). PRIOR TO VOLTAMMETRIC CYCLING, A BROAD, ASYMMETRIC BAND CENTERED AT 255 cm^{-1} AND A SMALLER SHOULDER AT 238 cm^{-1} WERE VISIBLE, AND ARE ASSIGNED TO A Se–Se STRETCH MODE IN GLASSY, LOOSELY PACKED POLYMER CHAINS AND TO A Se–Se STRETCH VIBRATION OF CLOSELY PACKED

CHAINS, RESPECTIVELY. THESE BANDS WERE NOT OBSERVED AFTER VOLTAMMETRIC CYCLING. 27

FIGURE 2.5: ELECTROCHEMICALLY ACTIVE SURFACE AREA MEASUREMENTS BEFORE (PRE-CYCLING) AND AFTER (POST-CYCLING) THE ELECTROCATALYSIS EXPERIMENTS SHOWN IN FIGURE 2.6. (A) CYCLIC NON-FARADAIC-CURRENT VS POTENTIAL CURVES AT PRE-SELECTED SCAN RATES; (B) NON-FARADAIC CURRENT AS A FUNCTION OF THE POTENTIAL SCAN RATE. 29

FIGURE 2.6: (A) CYCLIC VOLTAMMETRIC DATA FOR MOLYBDENUM SELENIDE THIN FILMS ON GLASSY CARBON IN 0.10 M $\text{H}_2\text{SO}_4(\text{AQ})$. IN THE FIRST CYCLE, THE INITIAL CATHODIC PORTION SHOWED A LOWER CURRENT DENSITY THAN THE RETURN ANODIC HALF-CYCLE. THE CURRENT DENSITY INCREASES IN SUBSEQUENT CYCLES, UNTIL THE TENTH CYCLE WHEN THE CURRENT DENSITY REACHED STEADY-STATE. (B) CURRENT-POTENTIAL PLOT FOR THE GLASSY CARBON SUBSTRATE (DOTTED CURVE) AND IMMEDIATELY AFTER THE TENTH (SOLID CURVE) CYCLE. (C) TAFEL PLOT OF THE CURRENT-POTENTIAL DATA IN (B); (D) A PLOT OF THE OVERPOTENTIAL NEEDED TO PRODUCE A CURRENT DENSITY OF 10 mA cm^{-2} DATA AS A FUNCTION OF TIME. 31

FIGURE 2.7: CURRENT DENSITY-POTENTIAL PROFILE OF THE PREPARED FILM BEFORE (PRE-CYCLING) AND AFTER (POST-CYCLING) ELECTROLYSIS. NORMALIZATION OF THE CURRENT DENSITY TO THE ELECTROCHEMICALLY ACTIVE SURFACE AREA GIVES RISE

TO TWO DISTINCT POLARIZATION CURVES THAT SHOW FUNDAMENTAL DIFFERENCES IN THE CATALYTIC ACTIVITY OF MoSe_3 AND MoSe_2	32
FIGURE 3.1: REPRESENTATIVE (A) SCANNING ELECTRON MICROGRAPH AND (B) RAMAN SPECTRUM OF AN ELECTROCHEMICALLY PREPARED COBALT SELENIDE FILM.	48
FIGURE 3.2: TOP: REPRESENTATIVE X-RAY DIFFRACTION PATTERN COLLECTED FROM A COBALT SELENIDE FILM. BOTTOM: STANDARD LINES FOR POLYCRYSTALLINE TI (JCPDS 65-9622).	49
FIGURE 3.3: REPRESENTATIVE HIGH-RESOLUTION X-RAY PHOTOELECTRON SPECTRA OF AN ELECTROCHEMICALLY PREPARED COBALT SELENIDE FILM IN THE (A) Co 2P AND (B) Se 3D REGIONS.	50
FIGURE 3.4: (A) CATHODIC POLARIZATION CURVES OF TITANIUM FOIL AND OF A COBALT SELENIDE FILM IN 0.500 M H_2SO_4 SATURATED WITH $\text{H}_2(\text{G})$ (INSET HIGHLIGHTS BEHAVIOR AT LOW OVERPOTENTIALS). (B) TAFEL PLOT DERIVED FROM DATA IN (A).51	
FIGURE 3.5: TURNOVER FREQUENCY OF COBALT SELENIDE FILMS AS FUNCTION OF OVERPOTENTIAL FOR THE HYDROGEN-EVOLUTION REACTION IN 0.500 M H_2SO_4 SATURATED WITH $\text{H}_2(\text{G})$ DERIVED FROM THE VOLTAMMETRIC DATA IN FIGURE 3.4A.52	
FIGURE 3.6: (A) POTENTIAL APPLIED TO A COBALT SELENIDE FILM AS A FUNCTION OF TIME DURING GALVANOSTATIC ELECTROLYSIS AT -10 mA cm^{-2} IN 0.500 M H_2SO_4 (B) POLARIZATION CURVES OF A COBALT SELENIDE FILM ACQUIRED BEFORE AND AFTER	

1000 ACCELERATED FULL POTENTIAL CYCLES BETWEEN 0.100 V AND -0.175 V VS. RHE.....	54
FIGURE 4.1: SCANNING-ELECTRON MICROGRAPHS OF THE FILMS BEFORE (A, B AND C) AND AFTER (D, E AND F) VOLTAMMETRY. A: AN AS-DEPOSITED THIN FILM SHOWED THE PRESENCE OF QUASI-SPHERICAL CLUSTERS ON THE SURFACE. B AND C: THE FILM UNDERNEATH THE PARTICLES APPEARED UNIFORMLY ROUGHENED. D: POST-ELECTROLYSIS FILM SHOWED CLOSE-PACKED PLATEAU-TOPPED ISLANDS ON THE SURFACE. E AND F: THE TOPS OF THE MESA-LIKE ISLANDS WERE FLAT AND RELATIVELY SMOOTH.....	64
FIGURE 4.2: ENERGY-DISPERSIVE X-RAY SPECTROSCOPY OF THE FILMS BEFORE AND AFTER VOLTAMMETRY. THE CO:P ATOMIC RATIO DECREASED FROM 20:1 TO 1:1 AFTER THE VOLTAMMETRIC EXPERIMENTS.	65
FIGURE 4.3: HIGH-RESOLUTION X-RAY PHOTOELECTRON SPECTRA OF (A) CO 2P REGION OF THE AS-DEPOSITED THIN FILM; (B) P 2P REGION OF THE AS-DEPOSITED THIN FILM; (C) CO 2P REGION AFTER VOLTAMMETRY; (D) P 2P REGION AFTER VOLTAMMETRY.	67
FIGURE 4.4: RAMAN SPECTRA BEFORE AND AFTER VOLTAMMETRY. THE PEAKS AT CA. 600 CM^{-1} CORRESPOND TO CO-O VIBRATIONAL MODES, WHEREAS THOSE AT CA. 1100 CM^{-1} ARE ATTRIBUTABLE TO P-O MODES.	68
FIGURE 4.5: (A) CYCLIC VOLTAMMETRIC DATA FOR COBALT PHOSPHIDE THIN FILMS ON GLASSY CARBON IN AQUEOUS 0.50 $M\text{H}_2\text{SO}_4$. (B) CURRENT DENSITY VS POTENTIAL	

DATA FOR Pt (GRAY), THE THIRD SCAN OF CoP (BLACK), Co (BLUE) AND Cu (RED).

(C) TAFEL PLOT OF CoP FROM THE CURRENT DENSITY VS POTENTIAL DATA IN (B). (D)

TAFEL PLOTS THAT COMPARE THE ACTIVITY OF THE FILM IN 0.50 M H₂SO₄ WITH THAT

OF Pt,²¹ CoP NANOPARTICLES,²¹ Ni₂P NANOPARTICLES,²⁰ CoSe THIN FILMS,⁴¹ MoSe₂

THIN FILMS,⁴² AND MoS₂ THIN FILMS.⁹ 69

FIGURE 4.6: (A) CURRENT DENSITY VS POTENTIAL DATA IN 0.50 M H₂SO₄, FOR THE FIRST CYCLE AND AFTER UNINTERRUPTED SCANS OVER 24 H. (B) CHRONOPOTENTIOMETRY IN 0.50 M H₂SO₄ AT A CONSTANT CURRENT DENSITY OF 10 mA cm⁻². 70

FIGURE 5.1: CATHODIC POLARIZATION BEHAVIOR OF A CoP FILM IN 0.500 M H₂SO₄(AQ). 85

FIGURE 5.2: RAMAN SPECTRA OF CoP FILMS ACQUIRED UNDER THE INDICATED CONDITIONS. (A) EX-SITU SPECTRUM OF A CoP FILM PRIOR TO CONTACT WITH H₂SO₄(AQ) (AIR AMBIENT, EX-SITU). (B) CoP FILM IN 0.500 M H₂SO₄(AQ) AT OPEN CIRCUIT (IN-SITU). (C) SAME AS (B) BUT AT AN APPLIED POTENTIAL OF -0.300 V VS. SCE (OPERANDO). 86

FIGURE 5.3: Co K-EDGE X-RAY ABSORBANCE SPECTRA OF BOTH CoP FILMS UNDER THE INDICATED CONDITIONS AND RELATED SPECTRAL STANDARDS. (A) EX-SITU SPECTRUM OF A CoP FILM PRIOR TO CONTACT WITH H₂SO₄(AQ) (AIR AMBIENT, EX-SITU). (B) CoP FILM IN 0.500 M H₂SO₄(AQ) AT OPEN CIRCUIT (IN-SITU). (C) SAME AS (B) BUT AT AN

APPLIED POTENTIAL OF -0.300 V vs. SCE (OPERANDO). (D) Co STANDARD. (E) CoO STANDARD. 88

FIGURE 5.4: Co K-EDGE XAS OF CoP FILMS UNDER THE FOLLOWING CONDITIONS: (A) SPECTRUM OF A CoP FILM IN 0.500 M H_2SO_4 (AQ) AT AN APPLIED POTENTIAL OF -0.300 V vs. SCE (OPERANDO). (B) SPECTRUM OF A CoP FILM EXPOSED TO AIR AFTER OPERANDO CONDITIONS. (C) REFERENCE SPECTRUM OF AQUEOUS $CoCl_2$ 89

FIGURE 5.5: FOURIER-TRANSFORMED Co K-EDGE EXAFS OF CoP FILMS UNDER THE INDICATED CONDITIONS COMPARED TO CoO AND Co FOIL STANDARDS, PLOTTED AS APPARENT DISTANCE (TYPICALLY ~ 0.5 Å SHORTER THAN THE REAL DISTANCE). (A) EX-SITU SPECTRUM OF A CoP FILM PRIOR TO CONTACT WITH H_2SO_4 ELECTROLYTE (AIR AMBIENT, EX-SITU). (B) CoP FILM IN 0.500 M H_2SO_4 (AQ) AT OPEN CIRCUIT (IN-SITU). (C) SAME AS (B) BUT AT AN APPLIED POTENTIAL OF -0.300 V vs. SCE (OPERANDO). (D) CoP FILM AFTER OPERATION AND EXPOSURE TO AIR. (E) CoO STANDARD. (F) Co FOIL STANDARD. 91

FIGURE 5.6: P K-EDGE X-RAY ABSORBANCE SPECTRA OF BOTH CoP FILMS UNDER THE INDICATED CONDITIONS AND RELATED SPECTRAL STANDARDS. (A) EX-SITU SPECTRUM OF A CoP FILM PRIOR TO CONTACT WITH H_2SO_4 ELECTROLYTE (AIR AMBIENT, EX-SITU). (B) CoP FILM IN 0.500 M H_2SO_4 (AQ) AT OPEN CIRCUIT (IN-SITU). (C) SAME AS (B) BUT AT AN APPLIED POTENTIAL OF -0.300 V vs. SCE (OPERANDO). (D) K_3PO_4 STANDARD. (E) $NaPO_2H_2$ STANDARD. (F) GAP STANDARD..... 93

FIGURE 6.1: CAPITAL COST BREAKDOWN FOR OIL PIPELINES 105

FIGURE 6.2: CAPITAL COST BREAKDOWN FOR ELECTRICAL TRANSMISSION LINES..... 112

FIGURE 6.3: SUMMARY OF THE COST OF TRANSPORTATION ENERGY RESOURCES IN
DIFFERENT FORMS..... 114

LIST OF TABLES

TABLE 6.1: COST OF TRANSPORTING OIL IN PIPELINES	105
TABLE 6.2: COST OF TRANSPORTING NATURAL GAS BY PIPELINE	106
TABLE 6.3: COST OF TRANSPORTING HYDROGEN IN PIPELINES	107
TABLE 6.4: COST OF TRANSPORTING ENERGY AS REDOX FLOW BATTERY ELECTROLYTE BY PIPELINE.....	109
TABLE 6.5: COST OF TRANSPORTING OIL BY TANKER	110
TABLE 6.6: TRANSPORTATION COSTS FOR LIQUEFIED NATURAL GAS (LNG) BY TANKER	111
TABLE 6.7: ESTIMATED COST OF TRANSPORTING ELECTRICITY	113

Chapter 1

INTRODUCTION: GLOBAL WARMING, ENERGY AND ARTIFICIAL PHOTOSYNTHESIS

Though I cannot recall exactly when and what piqued my interest in global climate change and energy systems, by my senior year of high school my fascination was advanced enough that one of my Stanford undergraduate application essays focused on the (then) recent developments and improvements in hydrogen fuel vehicles. I remember thinking then (as I do now) that moving to vehicles that only emitted water from their exhaust pipes would be truly transformational. Thus it surprised no one that by my sophomore year of college I had joined the newly established lab of Professor Thomas Jaramillo and started investigating novel protection layers for photoelectrochemical water splitting devices. This interest in solar driven chemical syntheses would follow me throughout my time at both Stanford and Caltech and has included explorations into many different aspects of such systems including light absorbers, catalysts, systems integration, and their economic viability. Now, nearly a decade later, though I have a much broader, nuanced, and perhaps more pessimistic understanding of the energy ecosystem, I remain just as committed to working on finding new and disruptive ways to change it. This introductory chapter serves as a short primer on the current state of energy production, global warming, and photoelectrochemical cells.

1.1 Energy and the Climate

1.1.1 Global Energy Consumption

In the past several decades, global energy consumption has increased tremendously, more than doubling since 1971 (Figure 1.1) reaching ~14000 millions of tonnes of oil equivalent (Mtoe) in 2014. Though the amount of energy consumed has increased markedly, our main energy sources have remained remarkably consistent with over 80% of our energy coming solely from three fossil-fuel sources (oil, natural gas, and coal). Electricity production shows a similar trend with electricity generation increasing almost six fold since 1971 with the main source remaining fossil fuels (Figure 1.2).¹

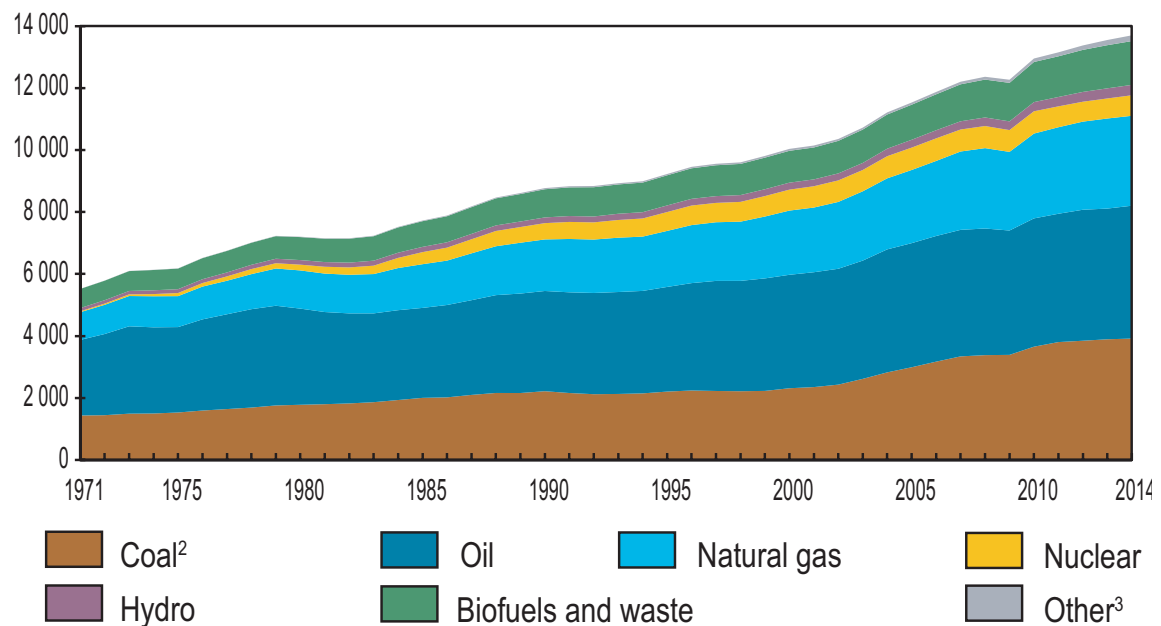


Figure 1.1: World total primary energy supply (TPES) from 1971 to 2014 by fuel (Mtoe).¹ © OECD/IEA 2016 Key World Statistics, IEA Publishing. License: www.iea.org/t&c

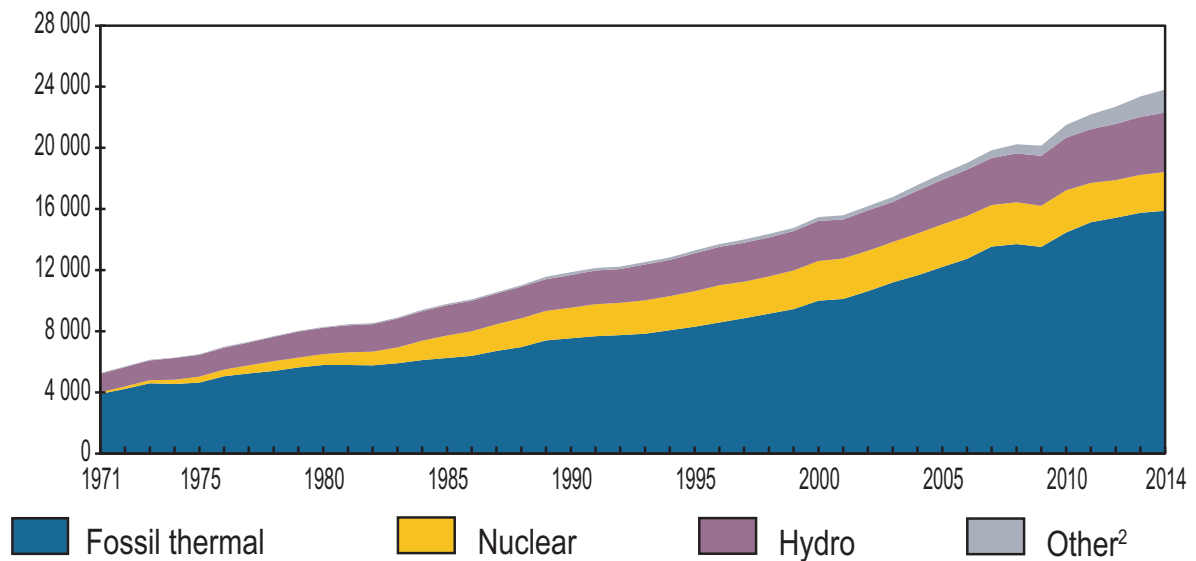


Figure 1.2: World electricity generation from 1971 to 2014 by fuel (TWh).¹ © OECD/IEA 2016 Key World Statistics, IEA Publishing. License: www.iea.org/t&c

Furthermore, global energy consumption is expected to continue rising in the future reaching ~21000 Mtoe by 2050.² This increase in energy consumption has been coupled with tremendous global economic growth, with global GDP per capita increasing ten-fold from \$866 in 1971 to over \$10,000 in 2014 (inflation adjusted).³ Unfortunately, while this increase in energy consumption, particularly in developing nations, has come with several benefits, the burning fossil fuels also leads to the direct emission of carbon dioxide and other pollutants into the atmosphere. These pollutants, including NO_x and SO_x, have been shown to adversely affect the environment and global ecosystem causing effects such as acid rain and smog.⁴ With total energy consumption expected to rise, decisions about where we obtain our energy will be ever more important.

1.1.2 Carbon Dioxide Emission

Since 1971, the amount of anthropogenic carbon dioxide emitted globally has more than doubled (Figure 1.3). This increase in global carbon dioxide emission is largely due to the increase in fossil fuel combustion, which accounts for ~80% of anthropogenic carbon dioxide emission.⁵

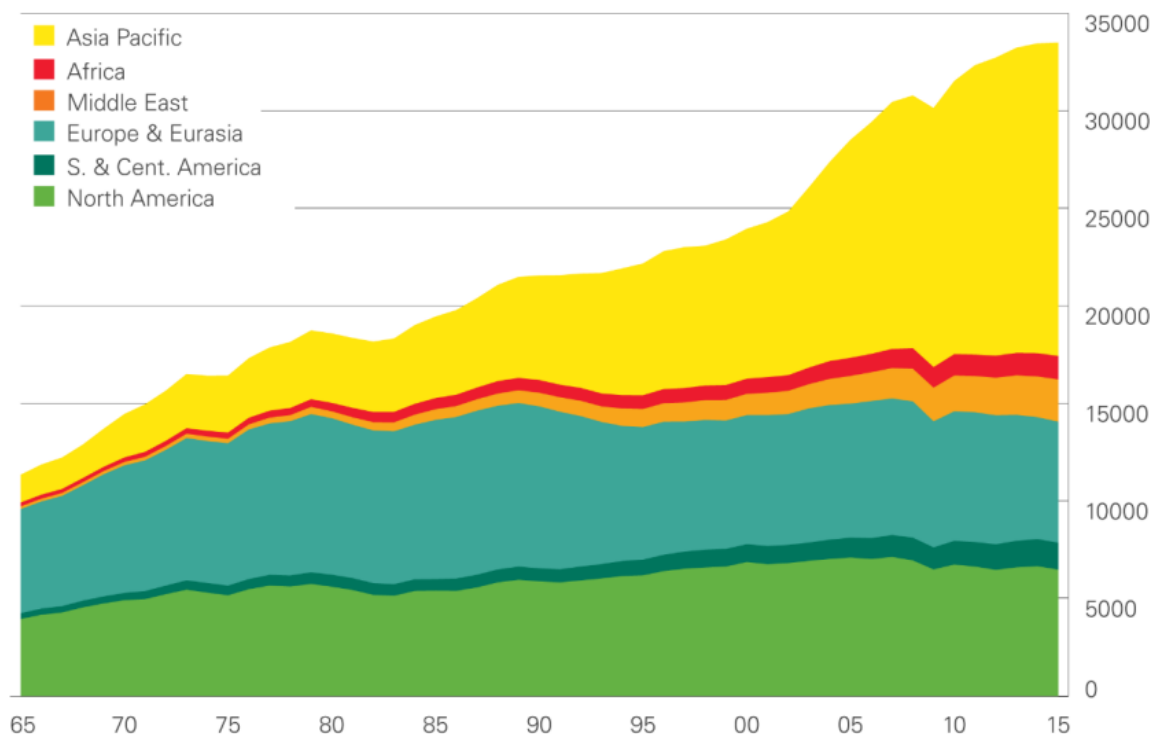


Figure 1.3: Annual global carbon dioxide emissions from 1965 to 2014 (million tonnes CO₂).⁶

It is estimated that approximately 60% of anthropogenic emission of carbon dioxide is released into the atmosphere with the majority of the rest being absorbed by oceans.⁷ While anthropogenic carbon emissions are relatively small compared to the overall magnitude of the carbon cycle, their net effect has been quite significant. The

anthropogenic carbon dioxide absorbed by the oceans has led to an ocean acidification of ~ 0.1 pH and significant damage to the health of marine ecosystems, in particular to coral reef health.⁸ Additionally, the level of carbon dioxide in the atmosphere has increased rapidly from 320 ppm in 1960 to over 400 ppm by 2014 (Figure 1.4), a rate hitherto unobserved.

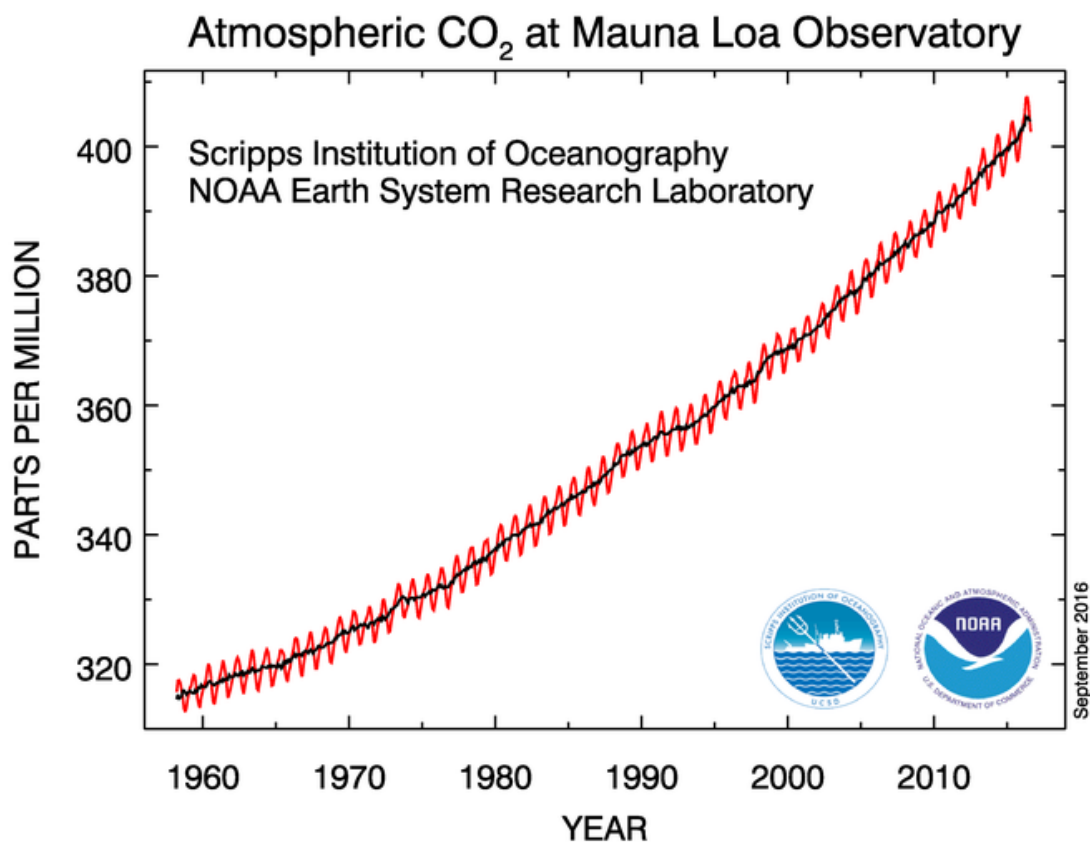


Figure 1.4: Monthly mean atmospheric carbon dioxide at Mauna Loa Observatory, Hawaii. Publically available from NOAA.⁹

1.1.3 Global Climate Change

Over the past fifty years, there has been a clear increase in both land and ocean average surface temperature (Figure 1.5). The increase in atmospheric carbon dioxide, as well as light hydrocarbons, is believed to contribute significantly to this increase in temperature through a process commonly known as the greenhouse effect. Though often considered controversial, it is estimated that 97% of climate change scientists believe in anthropogenic global warming.¹⁰

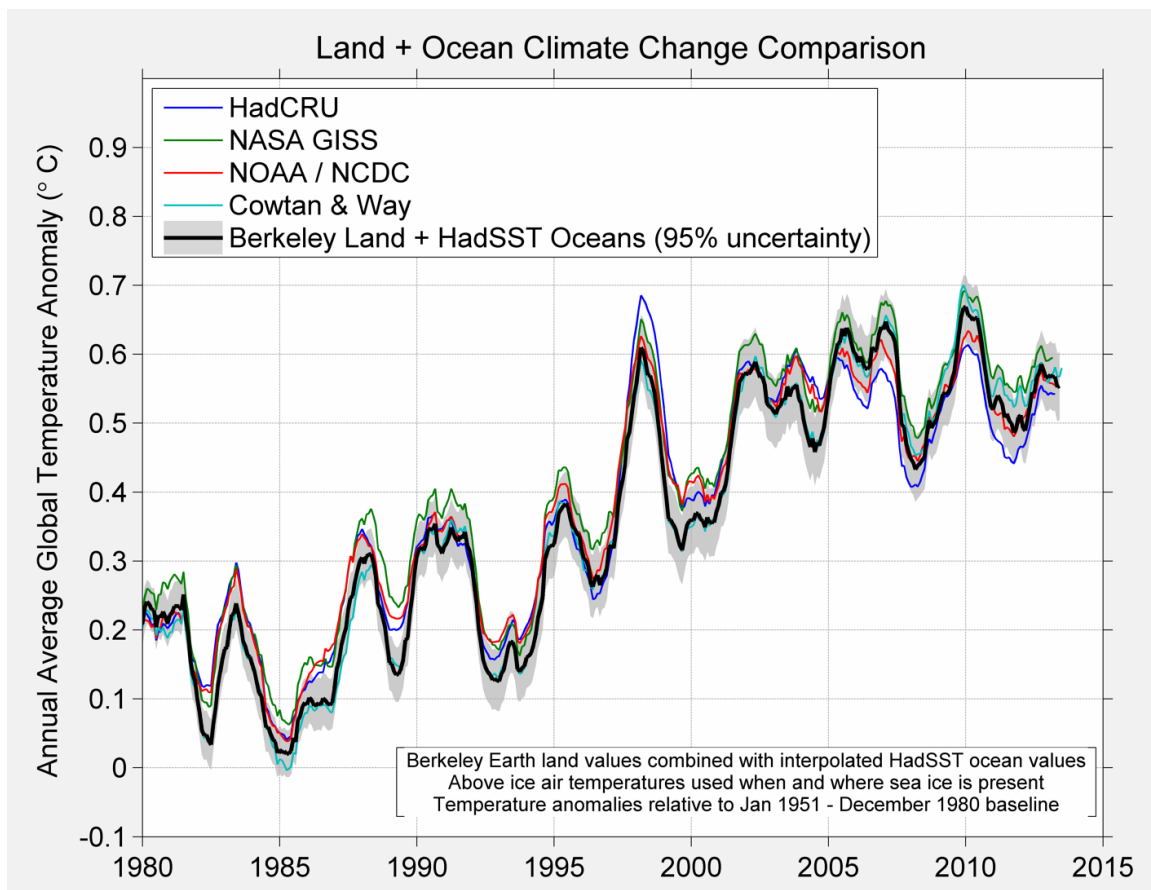


Figure 1.5: Anomalies of the global temperature index of provided by several groups is depicted for the 1980 to present time period. The base period is 1951-1980. The Berkeley baseline is depicted. Publically available from the BEST report.¹¹

While there are many studies that attempt to estimate future effects of anthropogenic carbon emissions, evaluating climate models goes beyond the scope of this introduction. Instead I will simply assert that we have already managed to increase atmospheric CO₂ and decrease ocean acidity to levels unseen for hundreds of thousands of years.⁸

1.2 Breaking the Energy & CO₂ Emission Bond

So far in this chapter we have seen that increased energy use has led to both improved economic prosperity as well as increased anthropogenic carbon emissions. These emissions have been shown to cause significant and lasting effects to our environment and health. That is the global emissions problem that we are currently facing. The only way to break this pattern is by decoupling energy consumption and carbon emissions. This can be done by two main ways: shifting to energy sources that are carbon-neutral or sequestering the carbon dioxide so that it does not escape into the atmosphere or bleed into the oceans. While there are many different energy sources that can be used in lieu of fossil fuels, several of these energy sources can only supply a small fraction of total energy needed. In the proceeding sections we will look into some of the more abundant sources of alternative energy and assess their future potential focusing primarily on the main scope of this thesis, photoelectrochemical water splitting.

1.2.1 Carbon Capture and Storage (CCS)

Carbon capture and storage is a process in which carbon dioxide, generated from a large waste source (usually a power plant or cement plant), is captured and stored underground where it cannot escape into the atmosphere. While not all anthropogenic carbon can be captured that way, this would allow us to continue using fossil fuels without increasing carbon dioxide emissions. While it has proven difficult to estimate the cost of

CCS, the U.S. Congressional Budget Office (CBO) has projected that the levelized cost of electricity produced from a supercritical pulverized coal plant would increase by ~70-80% if CCS is implemented.¹² Such high costs for CCS make it very difficult for it to be economically competitive in today's energy climate. Recently several proposed CCS projects such as the FutureGen 2.0 project in Meredosia, Illinois, the Hydrogen Energy California Project in Bakersfield, California and the Texas Clean Energy Project in Penwell, Texas have either been cancelled or put on indefinite hold. It remains to be seen if cost cutting measures and technological innovations will be able to make CCS competitive.

1.2.2 Hydropower

Currently hydropower is the largest alternative energy source accounting for ~16% of global electricity generation (Figure 1.6).¹ It currently supplies over 3000 TWh of electricity annually and has a technical potential estimated to be ~16000 TWh/yr.¹³

There are several benefits for hydroelectricity including its low cost (levelized cost of electricity for hydropower is estimated between 0.05 and 0.1 \$/kWh) as well as the ability to use hydro plants a cheap ways to store energy.¹⁴ Unfortunately, hydroelectricity is geographically unevenly distributed preventing certain countries from being able to utilize it significantly. Additionally, the total hydro capacity, while not insignificant, would only be able to supply ~15% of total energy demanded in 2015 and, seeing as energy consumption is expected to grow significantly in the next few decades, would constitute an even smaller potential share of the energy market in the future. Thus while hydropower will almost certainly play a crucial role in the future, the majority of energy will need to be supplied from other sources.

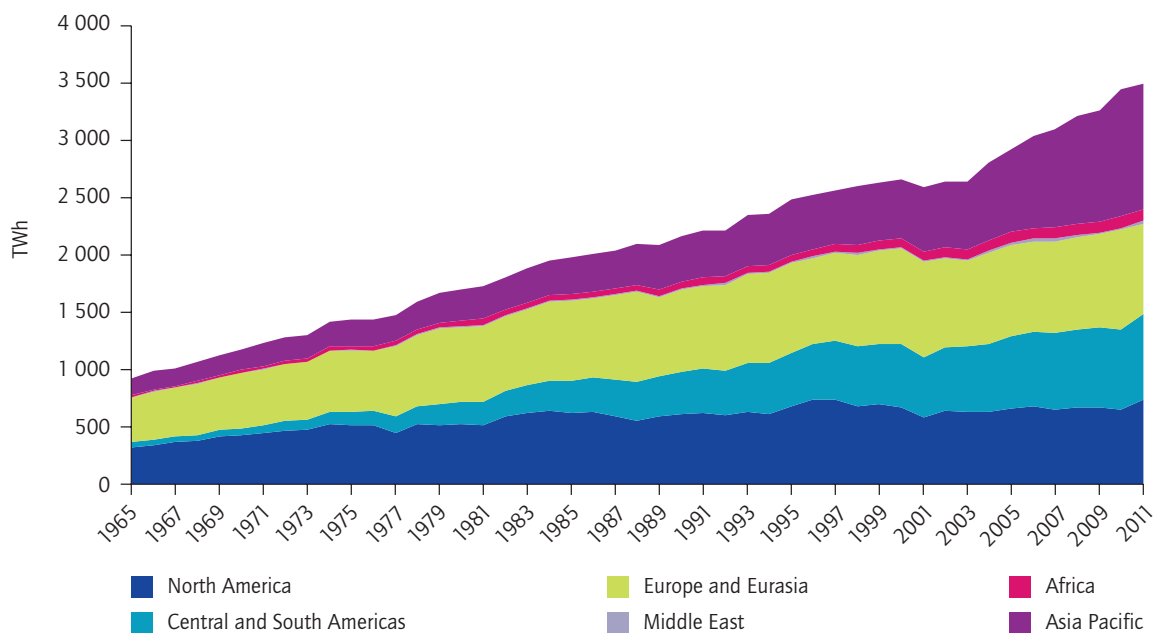


Figure 1.6: Hydroelectricity generation in TWh from 1965-2011.¹³

1.2.3 Nuclear Fission

Though there are many different types of nuclear power plants, they all work by harnessing the thermal energy generated from nuclear fission reactions of fissile material. Nuclear fission is the fifth most commonly used energy source and accounts for ~10% of global electricity generation (~2600 TWh).⁶ The levelized cost of electricity from new capacity nuclear is ~0.1 \$/kWh.¹⁵

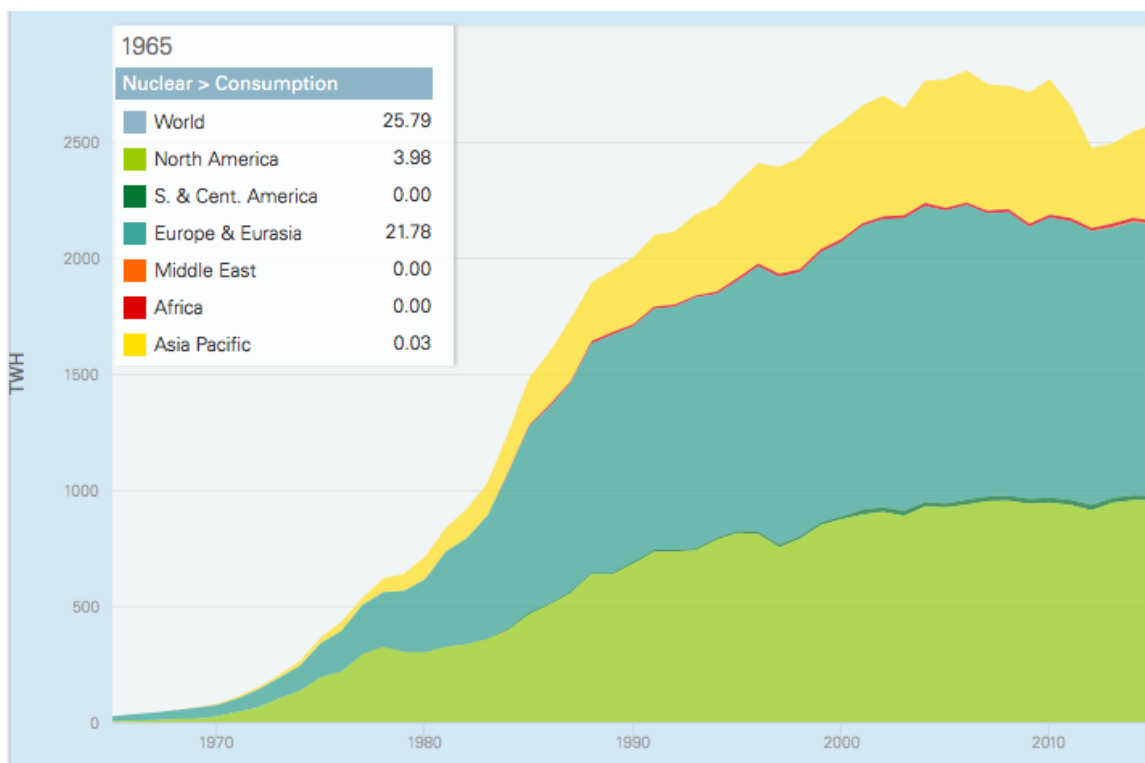


Figure 1.7: Nuclear energy generation from 1965-2014 (Terrawatt-hours).⁶

While nuclear has certain advantages, such as higher capacity factors, compared to many other carbon-neutral energy sources, the growth of nuclear energy has been essentially stalled since 1996.⁶ For nuclear fission to remain a prominent part of our energy economy, new power plants will need to be constructed at a much faster rate² especially as ~50% of all reactors are over 30 years old and will likely be decommissioned in the next two decades.

1.2.4 Wind Power

The most common way wind power is harnessed is by using airflow to mechanically power large turbines and generate electricity. Encouragingly, the total amount of wind potential has been calculated to be large enough for a significant amount of

global energy to be derived from it.¹⁶ Since 2006, the amount of installed wind generation capacity has grown five-fold and is now approximately 435 GW and an annual energy generation of ~841 TWh.⁶ Additionally, the levelized cost of wind electricity has decreased significantly in the past three decades with current analyses estimating the cost at significantly less than 0.10 \$/kWh for onshore wind and ~0.15 \$/kWh for offshore wind.¹⁵

1.2.5 Photovoltaic Cells

While quite diffuse, the largest available energy resource is sunlight with more solar energy striking the earth in 90 minutes than the total energy consumed in 2015.² Photovoltaic cells directly convert solar energy into electricity by harnessing the electrical potential in semiconductor junctions. While there are several semiconducting materials that can be used in solar panels including CIGS, CdTe, GaAs, and perovskites, silicon-based photovoltaics accounted for ~90% of total photovoltaic production in 2013.¹⁷ By 2015, over 200 GW of photovoltaics had been deployed globally and capital costs had fallen to ~2 \$/W¹⁷ with levelized costs lower than 0.1 \$/kWh for utility scale photovoltaics.¹⁵ While photovoltaic capacity has grown rapidly in the past decade, from ~5 GW in 2005 to over 200 GW in 2015, it still accounts for less than 1% of global electricity generation.⁶

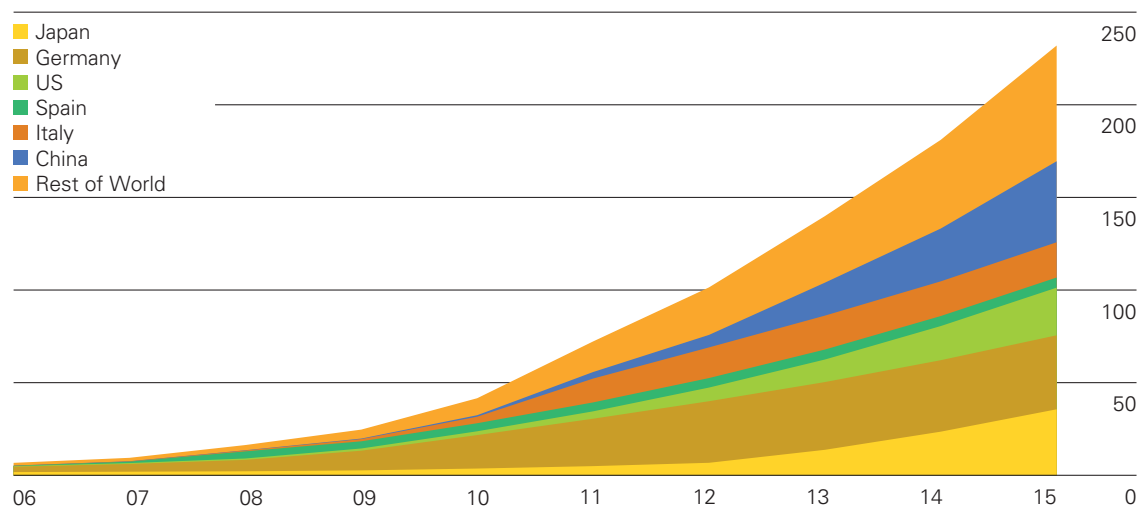


Figure 1.8: Global solar photovoltaic generation capacity (GW).⁶

1.2.6 Concentrated Solar Thermal

Solar thermal is another way to harness solar energy. Solar thermal plants use mirrors or lenses to concentrate solar energy onto a small area and convert it to heat. The four main types of concentrators are parabolic trough collectors, linear Fresnel reflectors, power towers, and dish-engine systems.¹⁷ The concentrated solar energy is converted to heat in either an oil or molten salt and is subsequently transferred to steam that is used to drive an engine and generate electricity. By 2014, less than 5 GW of concentrated solar power had been deployed globally making its market share significantly smaller than that of photovoltaics.¹⁷

1.3 Artificial Photosynthesis

As previously mentioned, the levelized costs of electricity from wind turbines and photovoltaics are quite low and can even, at times, undercut those of fossil fuels. Given that fact, one may wonder why governments, eager for energy independence, are not investing massive amount of money into solar and wind. The answer lies in these technologies' intermittent nature. The inability to run photovoltaics at night or wind turbines when it is not windy means that if a significant amount of the energy supply comes from those sources, energy storage in cheap and efficient ways is necessary. While there are several different technologies available for energy storage including pumped hydro, compressed air, and several different types of batteries, currently none of them have enough capacity and are cheap enough for them to be viable on a commercial scale.¹⁴

Artificial photosynthesis is an alternative method to harness solar energy, one which converts solar energy directly into a chemical fuel. Converting solar energy to chemical fuels instead of to electricity has several advantages including lower cost of energy transportation (see Chapter 6), higher energy density allowing for use in transportation vehicles that cannot be electrified and, for certain fuels, the ability to be integrated into existing infrastructure. Additionally, in contrast with photosynthetic

organisms which have a yearly efficiency of $<1\%$ ¹⁸, artificial photosynthetic devices are theoretically capable of much higher efficiencies.¹⁹

One of the simplest artificial photosynthetic devices is a photoelectrochemical water splitting device in which solar energy is used to split water into hydrogen and oxygen. Though studied for many years, no commercially viable photoelectrochemical device has been developed. This is partially due to the fact that such a device requires the optimization and integration of several different components including the light absorbing materials in which convert the solar energy into excited electron-hole pairs, the membranes which separate the oxygen and hydrogen gases, and the catalysts. For a more in-depth description of photoelectrochemical systems, I refer the reader to recent reviews published by the Lewis group.^{20, 21}

Although the free-energy change required to split one molecule of water corresponds to $E^0 = 1.23$ V per electron transferred, the electrolysis of water typically requires the application of an overpotential to drive the kinetically rate-limiting steps involved with the multistep oxidation and reduction half-reactions. Catalysts can improve the kinetics and efficiencies of the cathodic (hydrogen-evolution reaction, HER) and anodic (oxygen-evolution reaction, OER) half-reactions. While I have collaborated on several projects during my time at Caltech, my primary focus was on synthesizing and characterizing new acid stable catalysts for the hydrogen evolution reaction.

When I started, and even to this day, the most efficient water-splitting catalysts contain scarce metals like platinum (for the HER)^{20, 22-25} and iridium (for the OER).²⁰ For photoelectrochemical water splitting to be commercially viable in the terawatt scale, the HER and OER catalysts used in such a system must be made from earth-abundant elements.

Previously, the catalysis of the HER has been demonstrated using materials made from earth-abundant elements such as nickel alloys.²⁶⁻³⁰ In particular, nickel-molybdenum alloys require the application of only ~ 50 mV of overpotential to catalyze

the HER at a current density of -10 mA cm^{-2} .²⁷⁻³³ However, nickel-molybdenum alloys are unstable in strongly acidic solutions,^{27, 34} where proton-exchange membranes are operational and where the voltage loss due to the formation of a pH gradient across the membrane can be minimized.^{34, 35}

This thesis will focus on the work I have done to synthesize and characterize new acid stable hydrogen evolution catalysts. When I first joined the Lewis group, molybdenum disulfide had recently been reported as an acid stable HER catalyst. In consultation with Nate, my first project focused on expanding our understanding of the catalytic activity of related group VI chalcogenides, primarily molybdenum diselenide. I then collaborated with Azhar Carim on assessing the activity of another chalcogenide, cobalt selenide. Though these catalysts were found to be quite promising, the transition metal phosphide family, first characterized by the Schaak and Lewis groups, showed even greater potential. Intrigued by these new catalysts, I devised a new method to electrodeposit transition metal phosphides and decided to focus my efforts on understanding their *operando* chemical composition. In addition to that work, I have also included a chapter on the cost of energy transportation via different fuels, which was work that originated during my fellowship at the Dow Centre for Sustainable Innovation and was done to get a better sense of the economic feasibility of future energy transportation landscapes.

1.4 References

1. I. E. Agency, *Key world energy statistics*, 2016.
2. N. S. Lewis and D. G. Nocera, *Proceedings of the National Academy of Sciences*, 2006, **103**, 15729-15735.
3. C.-C. Lee, *Energy Economics*, 2005, **27**, 415-427.
4. A. Singh and M. Agrawal, *Journal of environmental biology*, 2007, **29**, 15.
5. U. S. E. P. Agency, *Inventory of U.S. Greenhouse Gas Emissions and Sinks: 1990-2014*, 2016.
6. BP, *BP Statistical Review of World Energy June 2016*, 2016.
7. I. P. o. C. Change, Cambridge University Press, 2007.
8. O. Hoegh-Guldberg, P. J. Mumby, A. J. Hooten, R. S. Steneck, P. Greenfield, E. Gomez, C. D. Harvell, P. F. Sale, A. J. Edwards, K. Caldeira, N. Knowlton, C. M. Eakin, R. Iglesias-Prieto, N. Muthiga, R. H. Bradbury, A. Dubi and M. E. Hatzitolos, *Science*, 2007, **318**, 1737-1742.
9. E. W. Team, 2005.
10. C. John, N. Dana, A. G. Sarah, R. Mark, W. Bärbel, P. Rob, W. Robert, J. Peter and S. Andrew, *Environmental Research Letters*, 2013, **8**, 024024.
11. Berkeley Earth Surface Temperature, Summary of Results.
12. C. o. t. U. S. C. B. Office, *Federal Efforts to Reduce the Cost of Capturing and Storing Carbon Dioxide*, 2012.
13. I. E. Agency, *Technology Roadmap: Hydropower*, 2012.
14. N. Singh and E. W. McFarland, *Journal of Power Sources*, 2015, **288**, 187-198.

15. U. S. E. I. Administration, Levelized Cost and Levelized Avoided Cost of New Generation Resources in the Annual Energy Outlook 2016, 2016.
16. M. Z. Jacobson and C. L. Archer, *Proceedings of the National Academy of Sciences*, 2012, **109**, 15679-15684.
17. N. S. Lewis, *Science*, 2016, **351**.
18. JASON, Engineering Microorganism for Energy Production, 2006.
19. S. Hu, C. Xiang, S. Haussener, A. D. Berger and N. S. Lewis, *Energy & Environmental Science*, 2013, **6**, 2984-2993.
20. M. G. Walter, E. L. Warren, J. R. McKone, S. W. Boettcher, Q. Mi, E. A. Santori and N. S. Lewis, *Chemical Reviews*, 2010, **110**, 6446-6473.
21. J. R. McKone, N. S. Lewis and H. B. Gray, *Chemistry of Materials*, 2013, **26**, 407-414.
22. H. B. Gray, *Nat Chem*, 2009, **1**, 7-7.
23. D. Merki and X. Hu, *Energy Environ. Sci.*, 2011, **4**, 3878-3888.
24. A. B. Laursen, S. Kegnæs, S. Dahl and I. Chorkendorff, *Energy Environ. Sci.*, 2012, **5**, 5577-5591.
25. T. Bak, J. Nowotny, M. Rekas and C. C. Sorrell, *Int. J. Hydrogen Energy*, 2002, **27**, 991-1022.
26. I. Paseka, *Electrochim. Acta*, 1995, **40**, 1633-1640.
27. J. R. McKone, B. F. Sadtler, C. A. Werlang, N. S. Lewis and H. B. Gray, *ACS Catal.*, 2012, **3**, 166-169.
28. D. E. Brown, M. N. Mahmood, M. C. M. Man and A. K. Turner, *Electrochim. Acta*, 1984, **29**, 1551-1556.

29. D. E. Brown, M. N. Mahmood, A. K. Turner, S. M. Hall and P. O. Fogarty, *Int. J. Hydrogen Energy*, 1982, **7**, 405-410.
30. I. A. Raj and K. I. Vasu, *J. Appl. Electrochem.*, 1990, **20**, 32-38.
31. D. Merki, S. Fierro, H. Vrubel and X. Hu, *Chem. Sci.*, 2011, **2**, 1262-1267.
32. N. V. Krstajić, V. D. Jović, L. Gajić-Krstajić, B. M. Jović, A. L. Antozzi and G. N. Martelli, *Int. J. Hydrogen Energy*, 2008, **33**, 3676-3687.
33. J. R. McKone, E. L. Warren, M. J. Bierman, S. W. Boettcher, B. S. Brunschwig, N. S. Lewis and H. B. Gray, *Energy Environ. Sci.*, 2011, **4**, 3573-3583.
34. E. J. Popczun, J. R. McKone, C. G. Read, A. J. Baccchi, A. M. Wiltrout, N. S. Lewis and R. E. Schaak, *J. Am. Chem. Soc.*, 2013, **135**, 9267-9270.
35. E. A. Hernandez-Pagan, N. M. Vargas-Barbosa, T. Wang, Y. Zhao, E. S. Smotkin and T. E. Mallouk, *Energy Environ. Sci.*, 2012, **5**, 7582-7589.

Chapter 2

OPERANDO SYNTHESIS OF MACROPOROUS MOLYBDENUM DISELENIDE FILMS FOR THE ELECTROCATALYSIS OF THE HYDROGEN-EVOLUTION REACTION

Saadi, F. H.; Carim, A. I.; Velazquez, J. M.; Baricuatro, J. H.; McCrory, C. C.; Soriaga, M. P.; Lewis, N. S. *ACS Catalysis* **2014**, *4*, 2866. DOI: <http://10.1021/cs500412u>

2.1 Introduction and Motivation

Shortly before I began my doctorate, Group VI chalcogenides were discovered as promising catalysts for the hydrogen evolution reaction and stable in acidic media.¹ Group VI chalcogenides such as molybdenum disulfide (MoS₂), molybdenum diselenide (MoSe₂), tungsten disulfide (WS₂), and tungsten diselenide (WSe₂) are comprised of earth-abundant elements, are stable in strong acid, and catalyze the HER with reported overpotentials of ~200-350 mV to produce current densities of -10 mA cm⁻².¹⁻²⁵ Theoretical^{3, 11} and experimental¹ studies of MoS₂ crystals suggest that the <10 $\bar{1}$ 0> edge sites are the active sites for hydrogen evolution. Many methods of preparing catalytically active MoS₂ have been developed, including sulfurization of molybdenum,¹⁹ electrochemical deposition from ammonium thiomolybdate,^{22, 26} wet-chemical

techniques⁵, and *ex crystallum* mechanical exfoliation.^{17, 27} In contrast, relatively few methods of preparing catalytically active MoSe₂, such as the selenization of metallic molybdenum, have been disclosed.^{19, 20}

In this chapter, we describe a two-step method for the synthesis of MoSe₂ films that are stable in acid and capable of catalyzing the HER. This method extends to MoSe₂, a synthetic route that has been reported for MoS₂.^{5, 8} In the first step, wet-chemical techniques are used to form a mixed-composition precipitate, which is then deposited as a film onto electrodes. The film-covered electrodes are then introduced into aqueous acid and used to drive the HER. The as-prepared films exhibited low catalytic activity, but the activity improved under the conditions of the HER, which convert the mixed-composition film into a macroporous film of MoSe₂.

2.2 Results

2.2.1 Characterization of as-deposited films

Figure 2.1A and 2.1B show scanning electron micrographs (SEMs) of a mixed-composition film on a glassy carbon substrate. The deposition was non-uniform and consisted of multiple islands ~100 μm in diameter separated by crevices up to 50 μm in width. Each island, however, was smooth and nonporous.

In comparison, Figures 2.1C and 2.1D show SEMs after reductive conversion of the films to HER catalysts during the electrochemical experiments. Substantial changes to the surface terrain were evident relative to the terrain in the pre-electrochemistry images. The island structures that were prominent at low levels of magnification prior to

conversion of the films were no longer visible, and the film appeared to be smooth. However, a macroporous structure that was absent prior to conversion of the films was apparent at higher magnification levels, and covered the entire sample. The pore sizes were estimated to be ~ 200 nm in diameter.

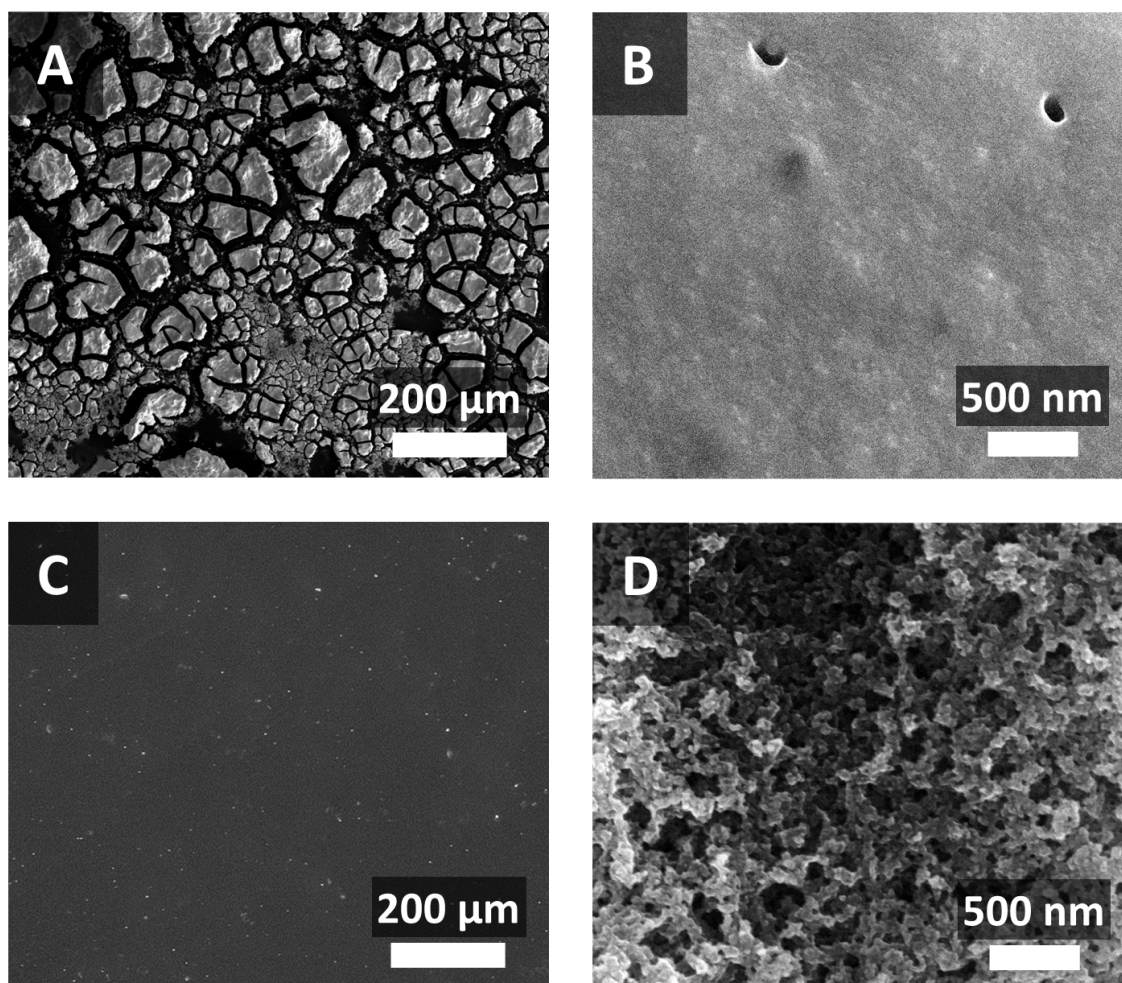


Figure 2.1: Scanning electron micrographs of the films before (A,B) and after (C,D) 10 cycles. (A) The as-deposited mixed-composition films on glassy carbon substrates were non-uniform, consisting of multiple islands $\sim 100 \mu\text{m}$ in diameter. (B) The surfaces of the islands were relatively smooth. (C) The island structure was not visible after electrocatalysis, and (D) at higher magnification, the entire surface appeared porous.

Figure 2.2A and 2.2B present high-resolution composite XPS spectra of the samples in the Mo and Se regions. Two sets of doublet peaks for Mo were observed (Figure 2.2A). The first doublet consisted of signals for Mo $3d_{5/2}$ at 233 eV and Mo $3d_{3/2}$ at 236 eV, and is characteristic of MoO_3 .^{4, 28} The second doublet consisted of peaks for Mo $3d_{5/2}$ at 232 eV and Mo $3d_{3/2}$ at 235 eV, and was located in a region typically associated with Mo^{6+} .²⁹ The single peak at 230 eV is characteristic of Se 3s. Figure 2.2B displays the Se region with two sets of 3d doublets: the higher-energy doublet ascribable to Se^0 and the lower-energy doublet ascribable to Se^{2-} .^{30, 31} Quantitation of the Mo $3d_{5/2}$ peak at 232 eV and the Se^{2-} 3d peak at 54 eV yields a Mo:Se ratio of 1:3.

The high-resolution X-ray photoelectron spectra of the Mo 3d and Se 3d regions for the converted films are displayed in Figures 2.2C and 2.2D. The Se 3s signal at 230 eV remained unchanged from the pre-conversion spectra, but the rest of the peak profile in Figure 2.2C was clearly different after the electrochemistry. The intensities of the Mo^{6+} doublet at 232 eV and 235 eV were significantly reduced, and the Mo^{4+} doublet³⁰ predominated the spectrum at 228.6 eV and 232 eV. More significantly, the Mo^{6+} peaks ascribed to MoO_3 were extinguished after electrolysis. The Se^{2-} species in Figure 2.2D were, therefore, associated with both Mo^{4+} and Mo^{6+} species in the form of MoSe_2 and MoSe_3 . The Se^0 doublet, which was prominent in the pre-conversion spectra (Figure 2.2B), decreased significantly after electrolysis, whereas the doublet attributed to Se^{2-} increased.

It is important to note that, before electrolysis, the O 1s peak (Figure 2.3E) appeared at 530.7 eV; the same O 1s peak was observed for both the oxidized molybdenum standards, MoO_3 (Figure 2.3B) and MoO_2 (Figure 2.3D). After electrolysis, the O 1s peak

shifted positively to 532 eV, implying the presence of adventitious oxygen, not of oxygen associated with oxidized molybdenum species.

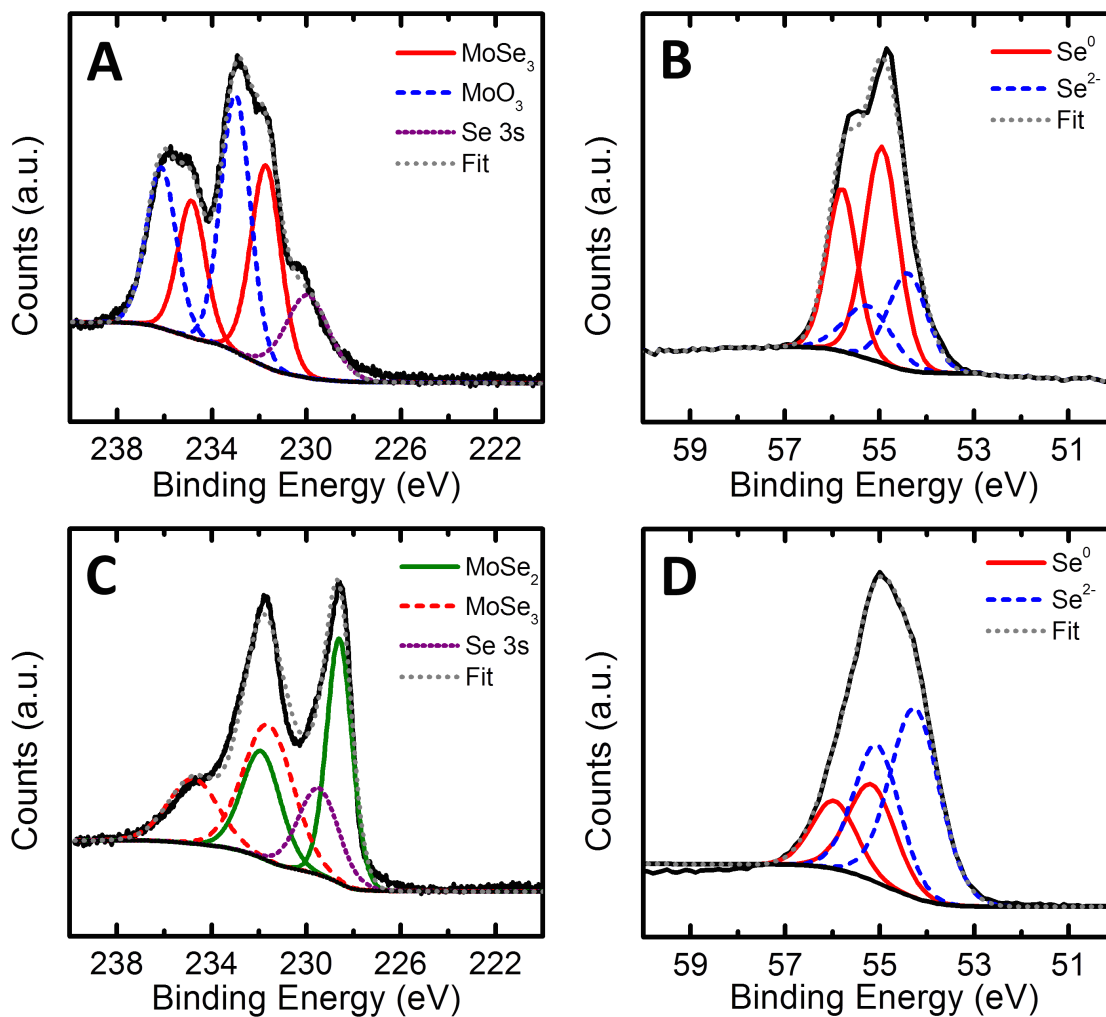


Figure 2.2: High-resolution X-ray photoelectron spectra of (A) the Mo 3d region of an as-deposited thin film; (B) the Se 3d region of an as-deposited thin film; (C) the Mo 3d region after 10 cycles; (D) the Se 3d region after 10 cycles.

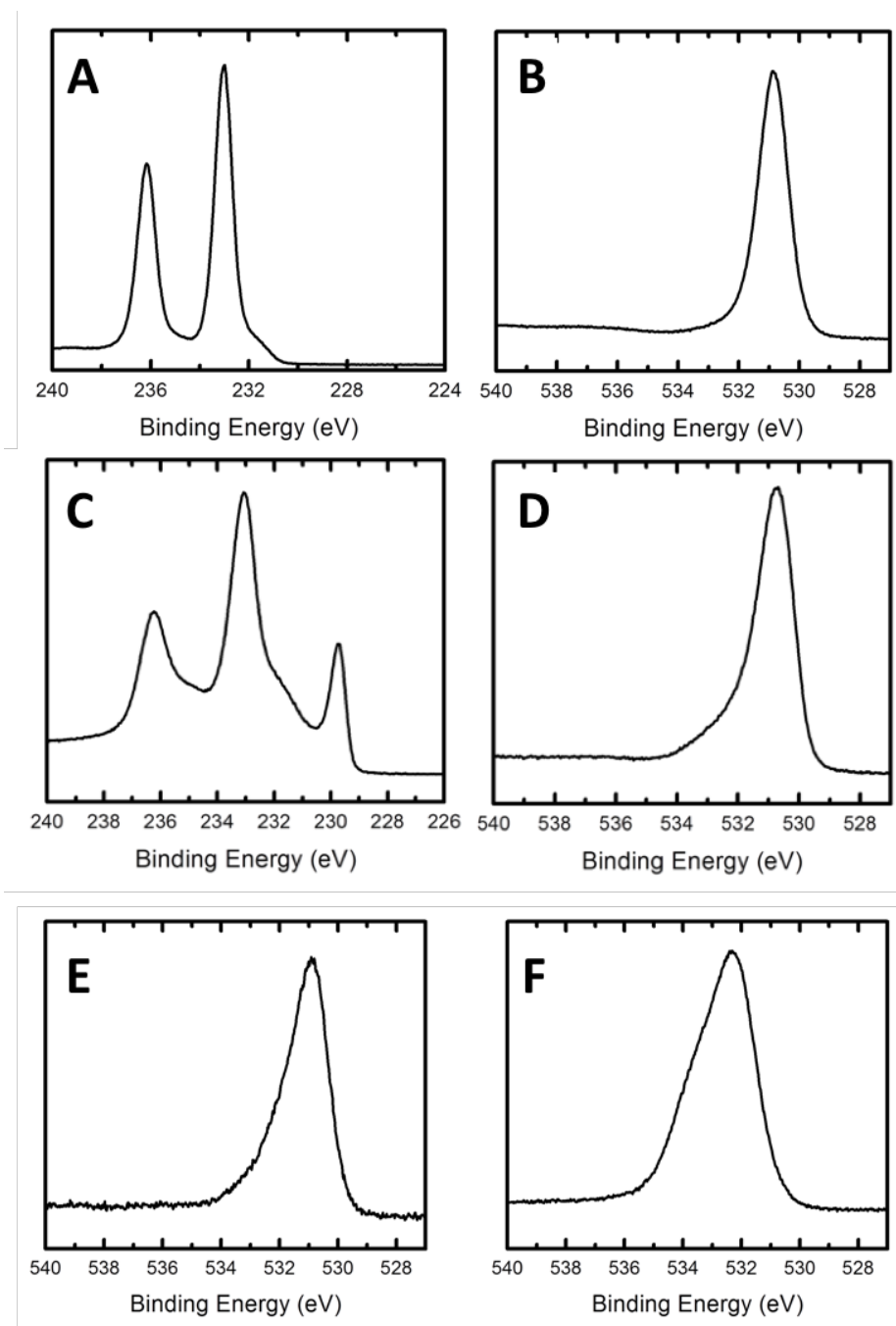


Figure 2.3: High-resolution X-ray photoelectron spectra of (A) the Mo 3d region of MoO₃; (B) the O 1s region of MoO₃; (C) the Mo 3d region of MoO₂; (D) the O 1s region of MoO₂; (E) the O 1s region of the as deposited film; (F) the O 1s region after 10 cycles.

The Raman spectrum of the as-deposited thin film exhibited a broad, asymmetric band centered at 255 cm^{-1} and a shoulder at $\sim 238\text{ cm}^{-1}$ (Figure 2.4). The prominent, higher-frequency peak is characteristic of a Se–Se stretch mode in glassy, loosely packed polymer chains, whereas the lower-energy shoulder is also due to a Se–Se stretch vibration, but indicates closely packed chains in which the local microscopic structure resembles that of crystalline (trigonal) Se.³²

After electrochemistry, the Raman spectra also exhibited significant (Figure 2.4). The vibrational band centered at $\sim 255\text{ cm}^{-1}$, which was prominent in the as-prepared films, was not observed for the converted films, suggesting that the amorphous polymeric chains of elemental Se were removed from the film during the reductive conversion process. No vibrational peaks characteristic of crystalline molybdenum selenide were detected for the converted films, suggesting that the films remained non-crystalline.

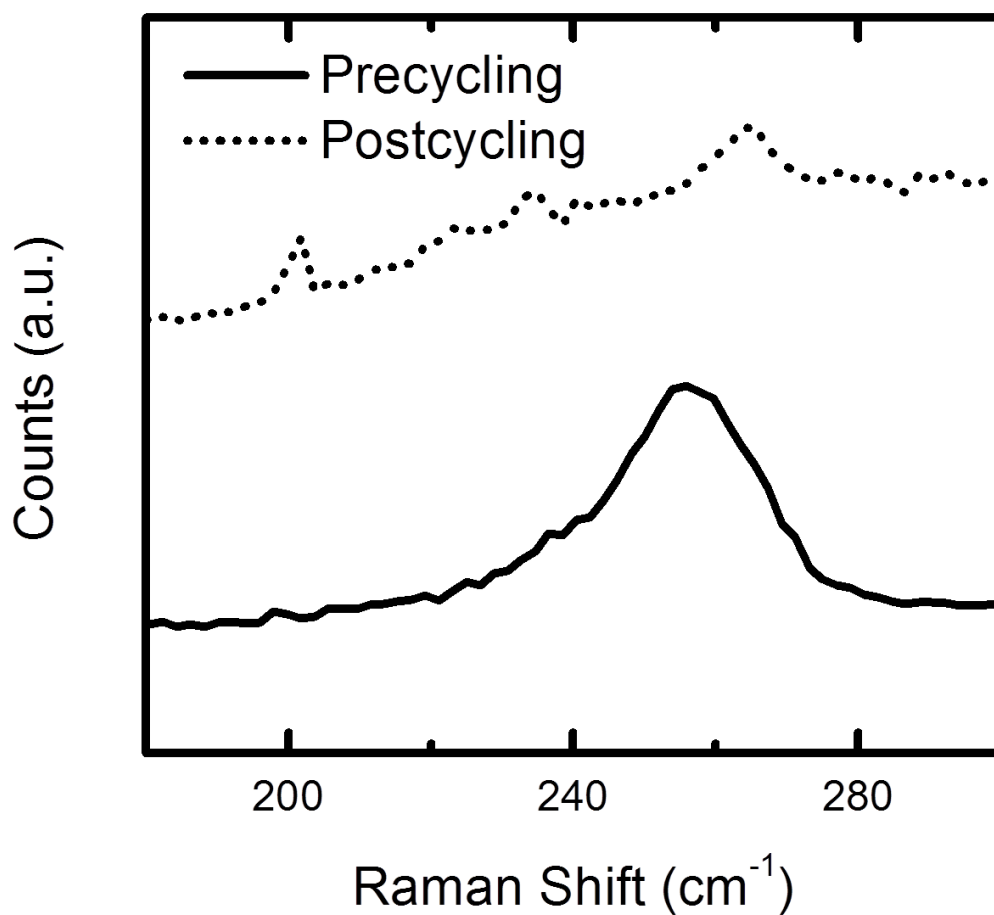


Figure 2.4: Raman spectra of an as-deposited thin film (solid) and of a film after ten cycles (dashed). Prior to voltammetric cycling, a broad, asymmetric band centered at 255 cm^{-1} and a smaller shoulder at 238 cm^{-1} were visible, and are assigned to a Se–Se stretch mode in glassy, loosely packed polymer chains and to a Se–Se stretch vibration of closely packed chains, respectively. These bands were not observed after voltammetric cycling.

Figure 2.5 shows the current density versus scan rate data that were used to calculate the geometric capacitance of a typical mixed-composition thin film and the converted films. The geometric capacitance of the film mixed-composition thin was $120 \mu\text{F cm}^{-2}$ and the roughness factor of the film was ~ 2 . The geometric capacitance of the converted film was $1200 \mu\text{F cm}^{-2}$ and the roughness factor of the film was ~ 20 , an order of magnitude larger than that measured in the as-deposited thin film.

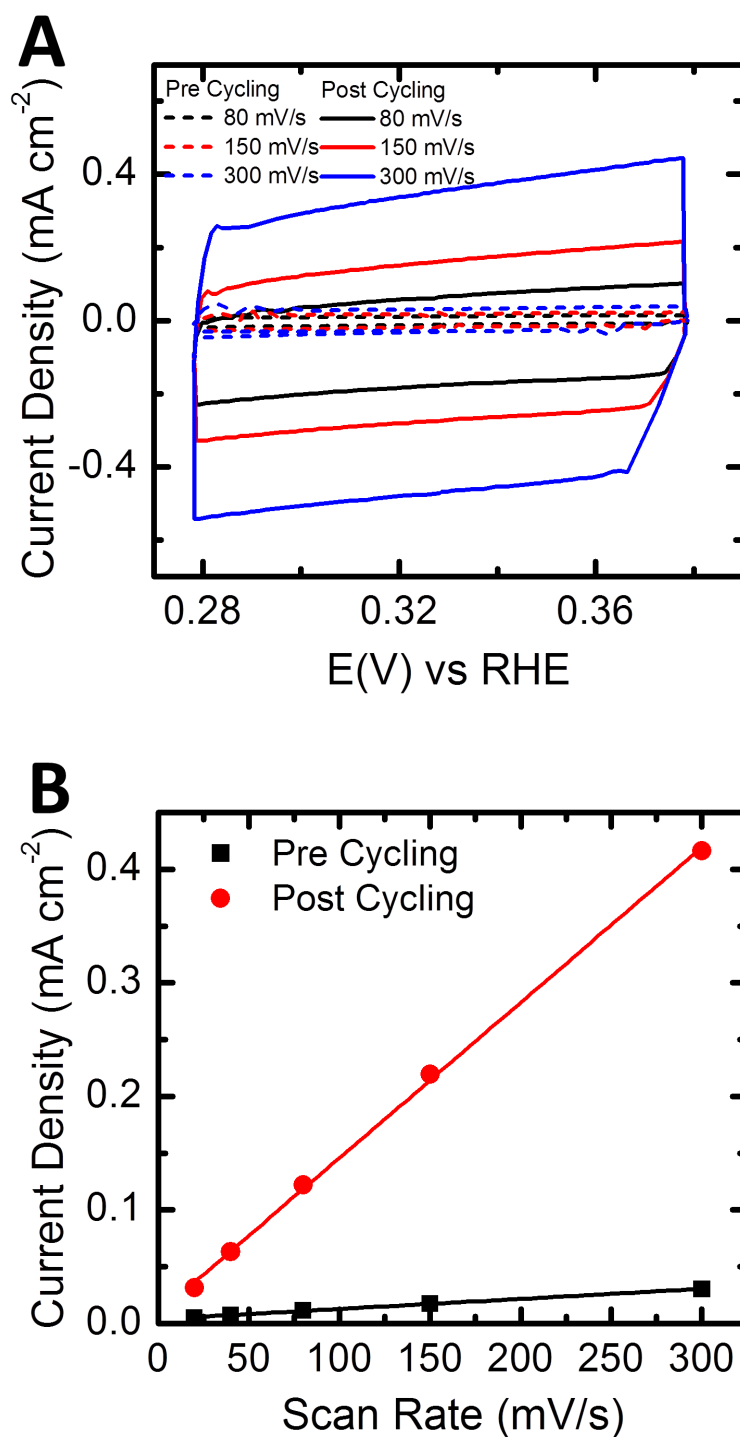


Figure 2.5: Electrochemically active surface area measurements before (pre-cycling) and after (post-cycling) the electrocatalysis experiments shown in Figure 2.6. (A) Cyclic non-

faradaic-current vs potential curves at pre-selected scan rates; (B) Non-faradaic current as a function of the potential scan rate.

2.2.2 Conversion of the films to catalysts of the HER

Figure 2.6A shows the first and tenth cyclic voltammetric cycles obtained using the film-coated glassy carbon RDEs. The onset for hydrogen evolution clearly shifted to less negative potentials between the first and tenth cycles. A steady state was reached by the tenth cycle, at which point 250 mV of overpotential was needed to produce a current density of -10 mA cm^{-2} . Based on the steady-state negative potential sweep data illustrated in Figure 2.5B, the Tafel slope was determined to be 80 mV dec^{-1} with an exchange current density of $1 \times 10^{-5} \text{ mA cm}^{-2}$ (Figure 2.6C).

The stability of the prepared film was characterized by plotting the overpotential required to produce a current density of 10 mA cm^{-2} for each cyclic voltammetric sweep performed during 48 h. As shown in Figure 2.6D, the overpotential to produce -10 mA cm^{-2} for the HER increased by $\sim 50 \text{ mV}$ over 48 h of operation.

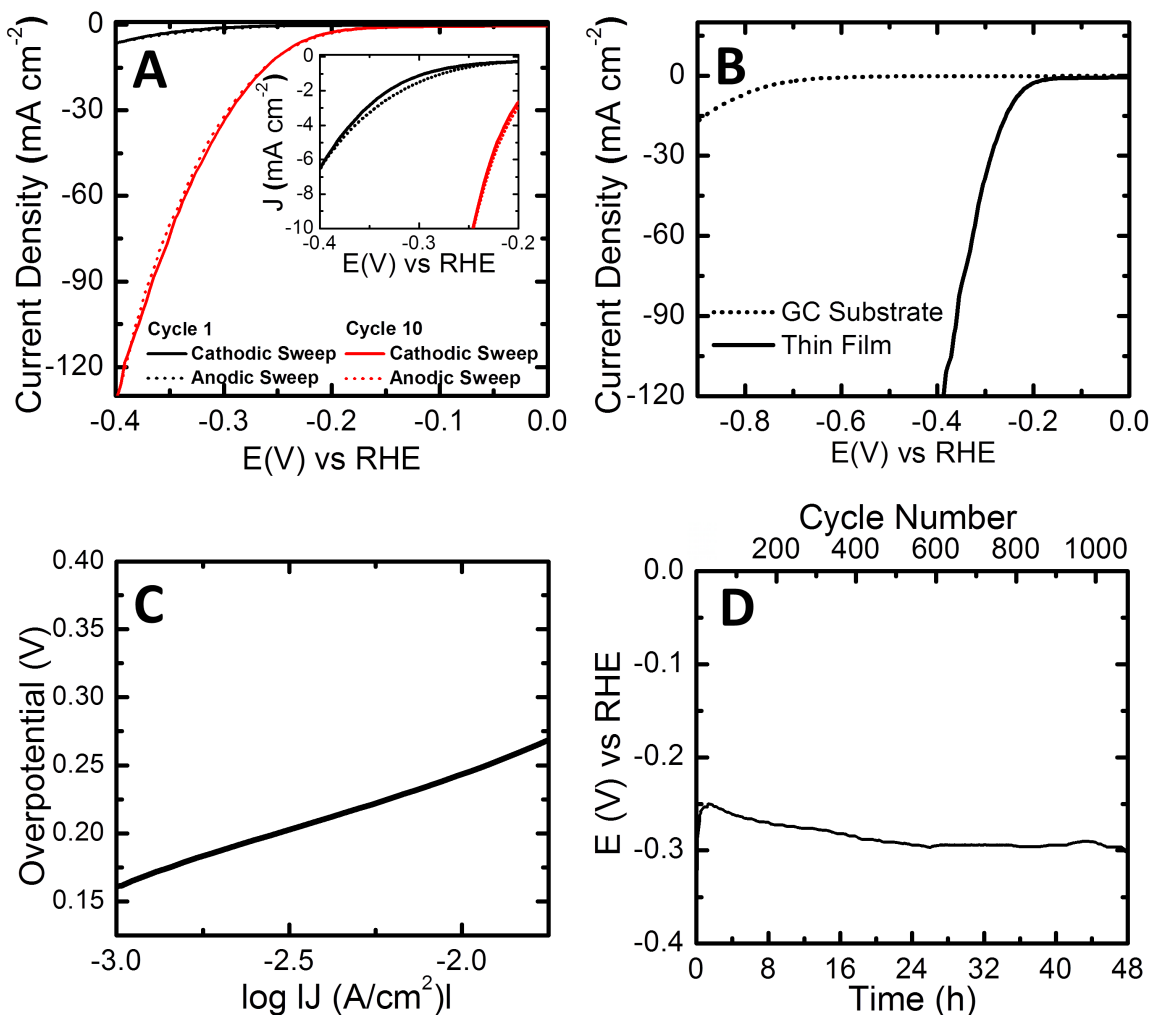


Figure 2.6: (A) Cyclic voltammetric data for molybdenum selenide thin films on glassy carbon in 0.10 M H₂SO₄(aq). In the first cycle, the initial cathodic portion showed a lower current density than the return anodic half-cycle. The current density increases in subsequent cycles, until the tenth cycle when the current density reached steady-state. (B) Current-potential plot for the glassy carbon substrate (dotted curve) and immediately after the tenth (solid curve) cycle. (C) Tafel plot of the current-potential data in (B); (D) A plot of the overpotential needed to produce a current density of 10 mA cm⁻² data as a function of time.

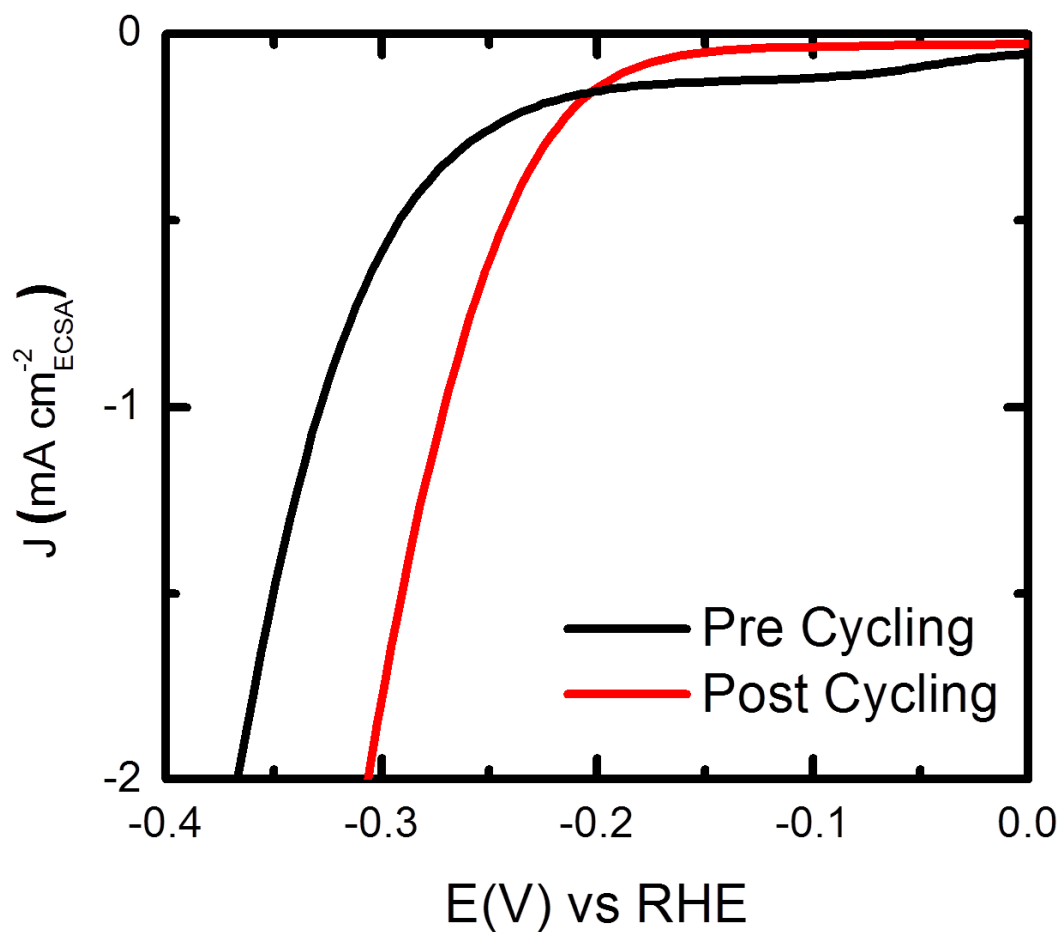
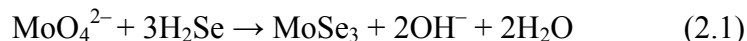


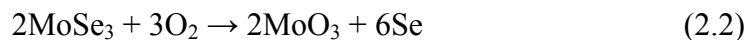
Figure 2.7: Current density-potential profile of the prepared film before (pre-cycling) and after (post-cycling) electrolysis. Normalization of the current density to the electrochemically active surface area gives rise to two distinct polarization curves that show fundamental differences in the catalytic activity of MoSe_3 and MoSe_2 .

2.3 Discussion

Reaction pathways directly analogous to those reported³³⁻³⁵ for MoS₂ likely apply to the wet-chemical synthesis of the mixed-composition precipitate. In aqueous solutions, ammonium heptamolybdate, (NH₄)₆Mo₇O₂₄·H₂O, exists as ammonium orthomolybdate, (NH₄)₂MoO₄, a strong electrolyte.³⁶ Mo is hexavalent in both of these structures. Thus, when sodium selenide is added to an acidic solution of (NH₄)₆Mo₇O₂₄·H₂O, the reaction that generates the black precipitate is likely to be:



where MoSe₃ is the black solid. The XPS data (Figures 2.2A and 2.2B) support the presence of Mo⁶⁺ and Se²⁻ in the as-prepared films. The same set of XPS data also indicates the presence of MoO₃, which may be formed either under the present synthesis conditions or by exposure of the synthesized MoSe₃ to air:



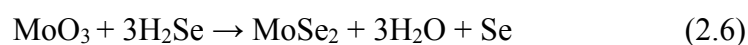
Equation (2.1) may also be accompanied, to a small extent, by the decomposition of MoSe₃:



The Se produced from reactions (2.2) and (2.3) was detected by the XPS and Raman spectroscopy.

MoSe₂, which is believed to be an active catalyst for the HER, is present only at very low concentrations, if at all, in the unconverted films, which consist of a mixture of MoSe₃, MoO₃, and Se. The as-prepared films are therefore relatively inactive HER catalysts. Reductive cycling significantly improved the catalytic activity of the films

(Figure 2.6A), and a steady state was achieved after ten cycles. This behavior is consistent with a process in which exposure of the multicomponent film to negative potentials, and consequent reductive generation of $\text{H}_2(\text{g})$, also served to concentrate MoSe_2 , based on a combination of three interfacial reactions that are analogous to the known reactions of MoS_2 and H_2S :^{33, 37, 38}



These reaction schemes are supported by the post-electrochemistry surface analysis: (i) the XPS results (Figure 2.2C and 2.2D) showed a decrease of the MoO_3 and MoSe_3 peaks and an emergence of the MoSe_2 signal, and (ii) the Raman spectrum (Figure 2.3) did not exhibit the vibrational mode for amorphous elemental Se.

The observed increase in the porosity and surface area of the film (Figure 2.4) may be due to several factors such as the expulsion of gases like H_2 and H_2Se . The release of H_2Se , represented in reaction (2.4), is analogous to the formation of H_2S that accompanies the reduction of MoS_3 to MoS_2 ^{39, 40}. Material loss due to the dissolution of MoO_3 could also contribute to the observed porosity.

Figure 2.7 plots the current divided by electrochemically active surface area versus potential of the samples before and after ten cyclic voltammograms. Notably, the improvement in catalytic activity of the material cannot be attributed solely to the increase in internal surface area of the film; i.e., the catalytic activity of the film was still superior after voltammetry even when increase in electrochemically active surface area was accounted for.

The overpotential for the onset for hydrogen evolution was measured to be ~150 mV (Figure 2.6A). The overpotential necessary to effect a HER current density of -10 mA cm^{-2} , a heuristic benchmark to assess catalytic activity in solar fuels applications under unconcentrated sunlight, was $<250 \text{ mV}$ (Figure 2.6B), and is within the range that has been reported for MoS_2 HER catalysts ($\sim 200\text{--}350 \text{ mV}$).^{4-6, 8, 9, 19, 26} The porous MoSe_2 films had higher catalytic activity and a lower Tafel slope than thin films of MoSe_2 synthesized via the selenization of Mo on glassy carbon, which required an overpotential of 430 mV to achieve a current density of -8 mA cm^{-2} , reported a Tafel slope of 105-120 mV dec^{-1} and stability for over 1000 cycles.^{19, 20}

Although Faradaic yields have not been determined directly, competing cathodic processes are unlikely. Stoichiometric reactions involving Mo or Se cannot have contributed more than 1 % to the charge passed during a 24 h chronoamperometric experiment as detailed in the experimental section.

The macroporous MoSe_2 thin films were stable catalysts of the HER in acidic media, and the overpotential required to sustain a current density of -10 mA cm^{-2} only increased by 50 mV over 48 h. Although a comparison of stability across catalysts is not straightforward, due to the wide range of results that have been reported, the macroporous thin film MoSe_2 catalysts appear to be at least as stable over the same time period as MoS_2 HER catalysts.⁵

2.4 Conclusion

The catalytically inactive components of a $\text{MoSe}_3/\text{MoO}_3$ film have been converted, through an *operando* method of synthesis, to produce a catalyst for the HER

while the film is catalyzing the HER. The addition of excess sodium selenide to ammonium heptamolybdate in aqueous sulfuric acid resulted in the spontaneous formation of a black precipitate that consisted primarily of molybdenum triselenide (MoSe_3) with small amounts of elemental Se. Molybdenum trioxide (MoO_3) was also formed upon exposure of the triselenide to atmospheric oxygen. The multicomponent thin film cast onto glassy carbon was relative inactive for the HER during initial voltammetric cycles, because the active catalyst, MoSe_2 , was either not present or was present only at very low concentrations. Further voltammetric cycling of the electrode in the potential region where the HER occurs led to substantial increases in the catalytic activity. By the tenth cycle, the overpotential needed to drive a catalytic current of -10 mA cm^{-2} had decreased from $\sim 450 \text{ mV}$ to 250 mV . The improvement in the catalytic activity occurred because, under HER conditions, the catalytically inactive components of the film were reductively converted to MoSe_2 . An *operando* synthesis of MoSe_2 was thus established. An amorphous, macroporous MoSe_2 framework was also generated in the synthesis and the MoSe_2 film exhibited long-term stability with only a 50 mV increase in overpotential after 48 h of continuous operation. The porous MoSe_2 films appear to hold promise as a catalyst for the HER in aqueous acidic electrolytes.

2.5 Experimental

All chemicals and materials were used as received, and all experiments were performed under ambient laboratory conditions, except where otherwise noted. Water was obtained from a Barnstead Nanopure purification system (Thermo Scientific,

Asheville, NC) and had a resistivity $\geq 18.2 \text{ M}\Omega\cdot\text{cm}$. All glassware was thoroughly cleaned in hot chromic acid (3% potassium dichromate in 10 M H_2SO_4).

Mixed-composition suspension. 0.60 g (5.2×10^{-4} mol) of ammonium heptamolybdate, $(\text{NH}_4)_6\text{Mo}_7\text{O}_{24}\cdot 4\text{H}_2\text{O}$, (99.98%, Sigma Aldrich, St. Louis, MO) was dissolved in 12 mL of a 0.20 M H_2SO_4 solution prepared by diluting 18 M H_2SO_4 (Sigma Aldrich) with H_2O . A separate solution was prepared by dissolving 0.15 g (1.2×10^{-3} mol) of sodium selenide, Na_2Se , (99.8%, Alfa Aesar, Ward Hill, MA) in 12 mL of H_2O . Inside a fume hood, the first solution was quickly poured into the second solution, and a black precipitate formed upon mixing.

The suspension was transferred to a centrifuge tube and centrifuged at 12,000 rpm for 30 min using a JA-17 rotor (Beckman Coulter, Brea, CA). A black precipitate collected at the bottom of the centrifuge tube. The yield was calculated to be 70%. The clear supernatant liquid was discarded and the precipitate was rinsed with several 15 mL aliquots of isopropanol (99.7%, Macron Chemicals, Center Valley, PA). A final 15 mL of isopropanol was then added to the centrifuge tube, which was then subjected to 30 min of sonication. This process resulted in suspension of the black solid in the isopropanol.

Preparation of film-coated rotating-disk electrodes (RDEs). Glassy carbon discs (HTW Hochtemperatur-Werkstoff GmbH, Thierhaupten, Germany), 5 mm in diameter and 4 mm thick, were polished on a LaboPol-5 polishing wheel (Struers, Inc., Cleveland, OH), first with a 600-grit CarbiMet SiC grinding paper (Buehler, Lake Bluff, IL) for 30 s, and subsequently with diamond slurries (Buehler) of 9, 6, 3, 1, and 0.1 μm diamond particle size, also for 30 s each. The carbon disks were then cleaned by sonication for 5

min *seriatim* in isopropanol (Macron Chemicals), acetone (ACS grade, Sigma Aldrich) and water.

A 30 μL drop (mass loading of 1.36 mg cm^{-2}) of the mixed-composition suspension was placed onto the polished side of a glassy carbon disk. The disk was then dried for 12 h in a vacuum desiccator with an internal pressure of 5000 Pa (50 mbar).

Electrochemistry. A 0.10 M solution of H_2SO_4 was used as the electrolyte for electrochemical experiments. A 250 mL four-port glass cell was filled with electrolyte and equipped with a film-coated rotating disk electrode (RDE), a graphite rod (99% pure, Alfa Aesar) that served as a counter electrode, and a Ag/AgCl reference electrode (CH Instruments, Austin, TX). The Ag/AgCl electrode consisted of a Ag wire in 1.0 M KCl and had been calibrated against a reversible hydrogen electrode (RHE) prior to use in these experiments, with the Ag/AgCl electrode having a potential of $280 \pm 2 \text{ mV}$ vs RHE. Potentiostatic control was accomplished using a BioLogic SP-200 potentiostat (Biologic, Grenoble, France). The uncompensated cell resistance was determined from a single-point high-frequency impedance measurement and was 85% compensated by the BioLogic positive-feedback software. The RDE was rotated at a rate of 1600 rpm during the experiments. During all of the HER-catalysis experiments, the cell was saturated with H_2 (99.999%, Air Liquide, Plumsteadville, PA) by bubbling the gas through the solution.

Cyclic voltammetric scans were obtained by sweeping the applied voltage between 0.0 and -0.40 V vs RHE at a scan rate of 5 mV s^{-1} . To evaluate the stability of the films, the cyclic voltammetric scans were performed continuously over a 48 h period. The physical characterization of the films was performed after ten cycles.

The surface roughness factors for the thin films were calculated from double-layer capacitance measurements.⁴²⁻⁴⁴ Current density vs potential data were acquired by sweeping the applied potential at various scan rates (20, 40, 80, 150, and 300 mV s⁻¹) in a potential range within which no Faradaic electron-transfer processes were observed (0.28–0.38 V versus RHE). The geometric capacitance of the thin films was calculated as the slope of a plot of scan rate vs current density at 0.34 V, which is the midpoint potential of the non-Faradaic region. The surface roughness factors for the thin films were calculated by dividing the measured geometric capacitance by the specific capacitance of MoS₂, which was taken as 60 μF cm⁻².^{21, 42-44}

Scanning electron microscopy. Scanning electron micrographs were acquired with an FEI Nova electron microscope (FEI, Hillsboro, OR) at a working distance of 5.0 mm. Low-magnification micrographs (field width > 100 μm) were obtained at an accelerating voltage of 10 kV with an Everhart-Thornley detector, whereas higher magnification experiments utilized an accelerating voltage of 15 kV and a through-the-lens detector.

X-ray photoelectron spectroscopy. X-ray photoelectron spectroscopic (XPS) data for elemental composition and valence information were collected with an Axis Ultra X-ray photoelectron spectrometer (Kratos, Manchester, United Kingdom) at a base pressure < 10⁻⁹ Torr. Data were obtained with a monochromatic Al Kα source (1486.7 eV) and a concentric hemispherical analyzer with a pass energy of 20 eV, with the photoelectrons captured normal to the surface. Binding energies were calibrated against the “adventitious” C 1s peak (taken as 284.65 eV). Peak fitting was performed using CasaXPS software (CASA Ltd, Teignmouth, United Kingdom) assuming a Shirley background⁴⁵ and symmetric Voigt line shapes comprised of Gaussian (70%) and

Lorentzian (30%) functions. The peak fitting was constrained to maintain a 2:3 ratio between the areas of the Mo 3d_{3/2} and Mo 3d_{5/2} peaks and to maintain a 3.15 eV separation between the binding energies of those two peaks. The possibility of Se to exist in the bridging Se₂²⁻ form, analogous to what has been reported for S in MoS₃,²⁷ was not considered here in the interpretation of the Se XPS spectra.

Raman Spectroscopy. Raman spectra of the films were obtained with a Renishaw inVia Raman microprobe (Renishaw, Wotton Under Edge, United Kingdom) equipped with a Leica DM 2500M microscope, a Leica N Plan 50x objective (Leica, Wetzlar, Germany) (numerical aperture = 0.75), a 1800 lines/mm grating and a CCD detector configured in a 180° backscatter geometry. A 532-nm diode-pumped solid-state laser (Renishaw RL532C50) was used as the excitation and delivered a 20 μW radiant flux at the surface of the sample.

High-Resolution Transmission Electron Microscopy (HRTEM). HRTEM was performed with a Tecnai F30ST system (FEI, Hillsboro, OR) run at a voltage of 300 kV. The films were prepared by pipetting the particle suspension onto 300-mesh carbon-coated Cu grids and allowing the suspension to evaporate.

X-Ray Diffraction (XRD). XRD measurement patterns were recorded on a Bruker D8 Discover with Vantec500 area detector using Cu Kα radiation ($\lambda = 1.5418 \text{ \AA}$) at 50W. XRD was performed on a powder of molybdenum selenide that was synthesized by drying the precipitant of the centrifuged products.

Faradaic Efficiency Calculations. Chronopotentiometric data from the stability studies show that the total number of electrons passed in 24 hours at 10 mA cm⁻² is 1.75 x 10⁻³ mol of electrons. Assuming a competing 2e⁻ process involving all the Mo atoms in

the film [e.g. the reduction of Mo(VI) to Mo(IV)], only 1.1×10^{-6} mol of e^- would be consumed; thus, the current associated with this side reaction is less than 0.1% of the total measured current. Even in the extreme hypothetical case of a competing $6e^-$ process, the side reaction would still constitute less than 0.2% of the total measured current. Thus, the faradaic yield is greater than 99%.

2.6 References

1. T. F. Jaramillo, K. P. Jorgensen, J. Bonde, J. H. Nielsen, S. Horch and I. Chorkendorff, *Science*, 2007, **317**, 100-102.
2. T. F. Jaramillo, J. Bonde, J. Zhang, B.-L. Ooi, K. Andersson, J. Ulstrup and I. Chorkendorff, *J. Phys. Chem. C*, 2008, **112**, 17492-17498.
3. J. Bonde, P. G. Moses, T. F. Jaramillo, J. K. Nørskov and I. Chorkendorff, *Faraday Discuss.*, 2009, **140**, 219-231.
4. Z. Chen, D. Cummins, B. N. Reinecke, E. Clark, M. K. Sunkara and T. F. Jaramillo, *Nano Lett.*, 2011, **11**, 4168-4175.
5. J. D. Benck, Z. Chen, L. Y. Kuritzky, A. J. Forman and T. F. Jaramillo, *ACS Catal.*, 2012, **2**, 1916-1923.
6. J. Kibsgaard, Z. Chen, B. N. Reinecke and T. F. Jaramillo, *Nat. Mater.*, 2012, **11**, 963-969.
7. D. Merki, H. Vrubel, L. Rovelli, S. Fierro and X. Hu, *Chem. Sci.*, 2012, **3**, 2515-2525.
8. H. Vrubel, D. Merki and X. Hu, *Energy Environ. Sci.*, 2012, **5**, 6136-6144.
9. H. Vrubel and X. Hu, *ACS Catal.*, 2013, 2002-2011.
10. H. Vrubel, T. Moehl, M. Gratzel and X. Hu, *Chem Commun.*, 2013, **49**, 8985-8987.
11. B. Hinnemann, P. G. Moses, J. Bonde, K. P. Jørgensen, J. H. Nielsen, S. Horch, I. Chorkendorff and J. K. Nørskov, *J. Am. Chem. Soc.*, 2005, **127**, 5308-5309.

12. J. H. Nielsen, L. Bech, K. Nielsen, Y. Tison, K. P. Jørgensen, J. L. Bonde, S. Horch, T. F. Jaramillo and I. Chorkendorff, *Surf. Sci.*, 2009, **603**, 1182-1189.
13. Y. Hou, B. L. Abrams, P. C. K. Vesborg, M. E. Björketun, K. Herbst, L. Bech, A. M. Setti, C. D. Damsgaard, T. Pedersen, O. Hansen, J. Rossmeisl, S. Dahl, J. K. Nørskov and I. Chorkendorff, *Nat. Mater.*, 2011, **10**, 434-438.
14. A. B. Laursen, S. Kegnæs, S. Dahl and I. Chorkendorff, *Energy Environ. Sci.*, 2012, **5**, 5577-5591.
15. B. Seger, A. B. Laursen, P. C. K. Vesborg, T. Pedersen, O. Hansen, S. Dahl and I. Chorkendorff, *Angew. Chem., Int. Ed.*, 2012, **51**, 9128-9131.
16. Z. Wu, B. Fang, Z. Wang, C. Wang, Z. Liu, F. Liu, W. Wang, A. Alfantazi, D. Wang and D. P. Wilkinson, *ACS Catal.*, 2013, 2101-2107.
17. M. A. Lukowski, A. S. Daniel, F. Meng, A. Forticaux, L. Li and S. Jin, *J. Am. Chem. Soc.*, 2013, **135**, 10274-10277.
18. Y. Li, H. Wang, L. Xie, Y. Liang, G. Hong and H. Dai, *J. Am. Chem. Soc.*, 2011, **133**, 7296-7299.
19. D. Kong, H. Wang, J. J. Cha, M. Pasta, K. J. Koski, J. Yao and Y. Cui, *Nano Lett.*, 2013, **13**, 1341-1347.
20. H. Wang, D. Kong, P. Johanes, J. J. Cha, G. Zheng, K. Yan, N. Liu and Y. Cui, *Nano Lett.*, 2013, **13**, 3426-3433.
21. Y. H. Chang, C. T. Lin, T. Y. Chen, C. L. Hsu, Y. H. Lee, W. Zhang, K. H. Wei and L. J. Li, *Adv. Mater.*, 2013, **25**, 756-760.
22. S. Murugesan, A. Akkineni, B. P. Chou, M. S. Glaz, D. A. Vanden Bout and K. J. Stevenson, *ACS Nano*, 2013.

23. M. L. Tang, D. C. Grauer, B. Lassalle-Kaiser, V. K. Yachandra, L. Amirav, J. R. Long, J. Yano and A. P. Alivisatos, *Angew. Chem., Int. Ed.*, 2011, **50**, 10203-10207.
24. D. Merki, S. Fierro, H. Vrubel and X. Hu, *Chem. Sci.*, 2011, **2**, 1262-1267.
25. J. M. Velazquez, F. H. Saadi, A. P. Pieterick, J. M. Spurgeon, M. P. Soriaga, B. S. Brunshwig and N. S. Lewis, *J. Electroanal. Chem.*, 2014, **716**, 45-48.
26. D. Merki and X. Hu, *Energy Environ. Sci.*, 2011, **4**, 3878-3888.
27. D. Voiry, H. Yamaguchi, J. Li, R. Silva, D. C. B. Alves, T. Fujita, M. Chen, T. Asefa, V. B. Shenoy, G. Eda and M. Chhowalla, *Nat. Mater.*, 2013, **12**, 850-855.
28. P. A. Spevack and N. S. McIntyre, *J. Phys. Chem.*, 1993, **97**, 11031-11036.
29. W. Swartz and D. M. Hercules, *Anal. Chem.*, 1971, **43**, 1774-1779.
30. W. e. Abdallah and A. E. Nelson, *J. Mater. Sci.*, 2005, **40**, 2679-2681.
31. M. Shenasa, S. Sainkar and D. Lichtman, *J. Electron Spectrosc. Relat. Phenom.*, 1986, **40**, 329-337.
32. S. N. Yannopoulos and K. S. Andrikopoulos, *J. Chem. Phys.*, 2004, **121**, 4747-4758.
33. A. Müller, E. Diemann, R. Jostes and H. Bögge, *Angew. Chem. Int. Edit.*, 1981, **20**, 934-955.
34. H. W. Wang, P. Skeldon, G. E. Thompson and G. C. Wood, *J. Mater. Sci.*, 1997, **32**, 497-502.
35. A. F. W. Holleman, Egon; Wiberg, Nils, *Lehrbuch der Anorganischen Chemie.*, Walter de Gruyter, 1985.
36. F. A. W. Cotton, Geoffrey; Murillo, Carlos A.; Bochmann, Manfred *Advanced Inorganic Chemistry (6th ed.)*, Wiley-Interscience, New York, 1999.

37. S. K. Srivastava and B. N. Avasthi, *J. Mater. Sci.*, 1993, **28**, 5032-5035.
38. F. Faraji, I. Safarik, O. P. Strausz, M. E. Torres and E. Yildirim, *Ind. Eng. Chem. Res.*, 1996, **35**, 3854-3860.
39. K. Hu, X. Hu, Y. Xu and J. Sun, *J. Mater. Sci.*, 2010, **45**, 2640-2648.
40. J. L. Brito, M. Ilija and P. Hernández, *Thermochim. Acta*, 1995, **256**, 325-338.
41. B. A. Bilal and H. Tributsch, *J. Appl. Electrochem.*, 1998, **28**, 1073-1081.
42. S. Trasatti and O. A. Petrii, *Pure Appl. Chem.*, 1991, **63**, 711-734.
43. B. E. Conway, V. Birss and J. Wojtowicz, *J. Power Sources*, 1997, **66**, 1-14.
44. R. Kötz and M. Carlen, *Electrochim. Acta*, 2000, **45**, 2483-2498.
45. D. A. Shirley, *Physical Review B*, 1972, **5**, 4709-4714.

Chapter 3

ELECTROCATALYSIS OF THE HYDROGEN-EVOLUTION REACTION BY ELECTRODEPOSITED AMORPHOUS COBALT SELENIDE FILMS

Carim, A. I.; Saadi, F. H.; Soriaga, M. P.; Lewis, N. S. *Journal of Materials Chemistry A* **2014**, 2, 13835. DOI: 10.1039/C4TA02611J

3.1 Introduction

Our work in Chapter 2 focused on a simple wet chemical synthesis of catalytic molybdenum selenide which resulted in a mesoporous structure that exhibited overpotentials of ~250 mV for HER current densities of -10 mA cm^{-2} . In this chapter we extend our exploration of acid stable hydrogen evolution catalysts to cobalt chalcogenides.

The binary Co chalcogenides have not been investigated as thoroughly as their Mo analogues for catalysis of the HER, but several catalytically active preparations have been reported.¹⁻⁴ Nanocrystalline thin films of CoS_2 and CoSe_2 synthesized by treating metallic Co films with S vapor at 550 °C or Se vapor at 450 °C have achieved a current density of -4 mA cm^{-2} at overpotentials of ~ 220 mV and 200 mV, respectively, in N_2 -dearated 0.5 M H_2SO_4 . Nanoparticle films of CoSe_2 fabricated by treating CoO nanoparticles (initially formed by pyrolysis of an ink containing $\text{Co}(\text{NO}_3)_2 \cdot 6\text{H}_2\text{O}$ at 600 °C) with Se vapor at 450 °C required an overpotential of ~ 210 mV to effect a current

density of -10 mA cm^{-2} in $0.5 \text{ M H}_2\text{SO}_4$. Amorphous films of Co-S, composed of Co and S in a $\sim 1 : 1.4$ atomic ratio, produced via electrodeposition followed by thermal annealing at $300 \text{ }^\circ\text{C}$ required an overpotential of $\sim 160 \text{ mV}$ to reach -10 mA cm^{-2} in phosphate buffer at $\text{pH} = 7$, but rapidly deactivated in $0.5 \text{ M H}_2\text{SO}_4$. Ni/NiO/CoSe₂ nanocomposites fabricated utilizing several hydrothermal, solvothermal, and annealing steps at temperatures between 180 and $250 \text{ }^\circ\text{C}$ have been shown to reach -10 mA cm^{-2} with an overpotential $< 100 \text{ mV}$ in Ar-saturated $0.5 \text{ M H}_2\text{SO}_4$, but are unstable in such media. Methods that employ solution-based techniques for catalyst synthesis and assembly under ambient conditions are preferable to high temperature and/or vapor-based techniques because solution-based techniques require relatively low energy inputs and provide increased compatibility with substrates. We describe herein an electrochemical method for the preparation of catalytically active, amorphous cobalt selenide films, from fully oxidized precursors in aqueous solution under ambient conditions.

3.2 Cobalt selenide electrodeposition and characterization

The cobalt selenide films were electrodeposited from an aqueous solution of $\text{Co}(\text{C}_2\text{H}_3\text{O}_2)_2$ and SeO_2 using potentiostatic electrolysis, and were then conditioned in $0.500 \text{ M H}_2\text{SO}_4$ using galvanostatic electrolysis in the HER regime (see section 3.5 for experimental methods). The cobalt selenide films were characterized by scanning electron microscopy (SEM), energy-dispersive X-ray spectroscopy (EDS), Raman spectroscopy, powder X-ray diffraction (XRD), and X-ray photoelectron spectroscopy (XPS).^{5, 6} Figure 3.1A shows a scanning-electron micrograph of an electrochemically

prepared film. The films were mesoporous and contained pores estimated to be ~ 20 nm in diameter. Measurements made using EDS indicated a Co:Se atomic ratio of 1:2. The Raman spectra (Figure 3.1B) displayed no signatures of crystalline CoSe_2 nor of Se,^{7, 8} but contained a broad band centered at ~ 233 cm^{-1} indicative of the stretching of Se–Se bonds in glassy selenium comprised of close-packed chains in which the local microscopic structure resembles that of crystalline, trigonal Se.⁹ The Raman spectra also exhibited a less intense, lower frequency feature, centered at ~ 166 cm^{-1} , consistent with expectations for the bending of the Se–Se bonds in the close-packed chains as well as the presence of disordered CoSe.^{10, 11}

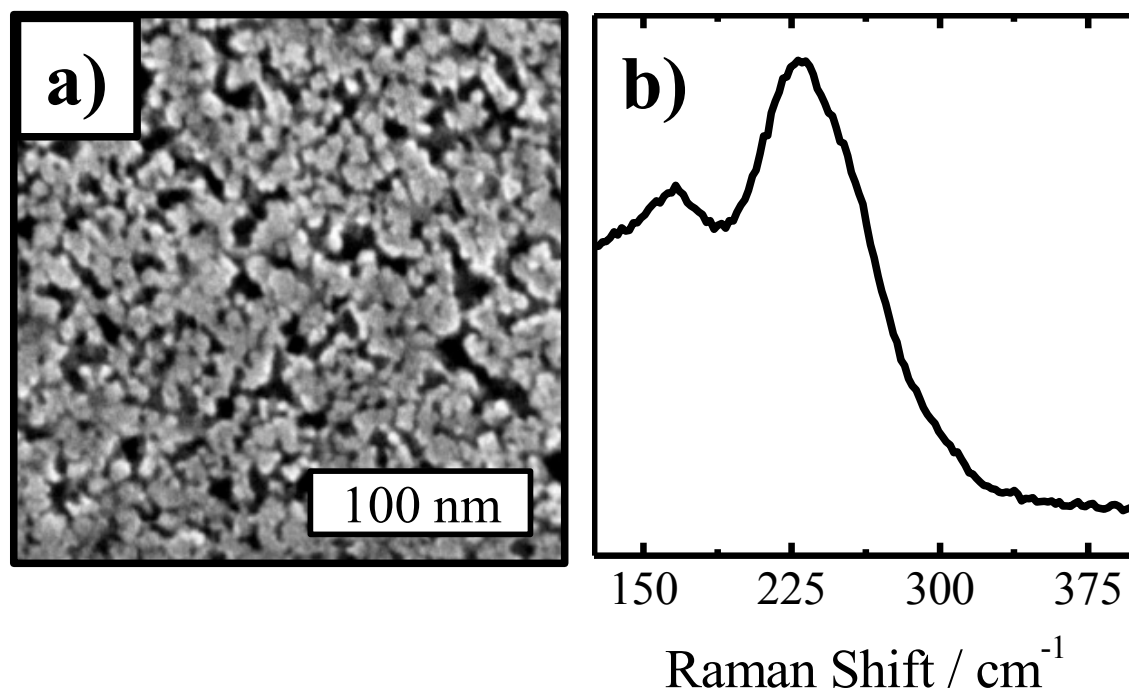


Figure 3.1: Representative (A) scanning electron micrograph and (B) Raman spectrum of an electrochemically prepared cobalt selenide film.

No signals were observed from oxygenated cobalt species.¹²⁻¹⁴ The Raman spectra were consistent with the XRD pattern obtained for the film (Figure 3.2), which only exhibited reflections that corresponded to the Ti substrate and did not show reflections that corresponded to any crystalline cobalt selenide species.

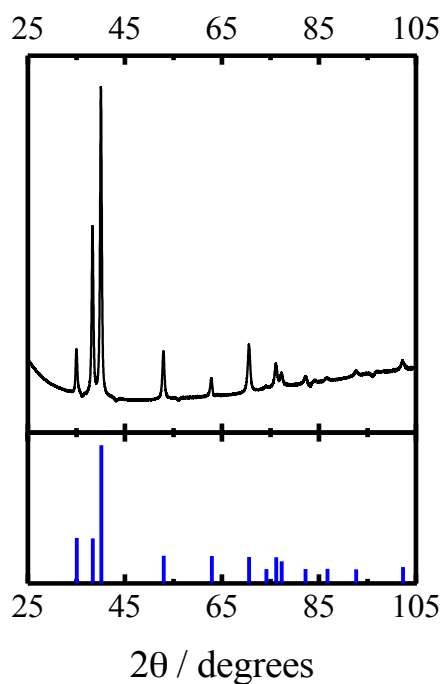


Figure 3.2: Top: Representative X-ray diffraction pattern collected from a cobalt selenide film. Bottom: Standard lines for polycrystalline Ti (JCPDS 65-9622).

High-resolution XPS analysis of the Co 2p region (Figure 3.3A) displayed an intense Co 2p_{3/2} line at 781.5 eV which was not consistent with expectations for CoSe₂.¹⁵ XPS analysis of the Se 3d region (Figure 3.3B) revealed the presence of Se in both the Se⁰ and Se²⁻ oxidation states. Thus, the cumulative data suggest that the films were composed of disordered CoSe in a polymeric Se matrix.

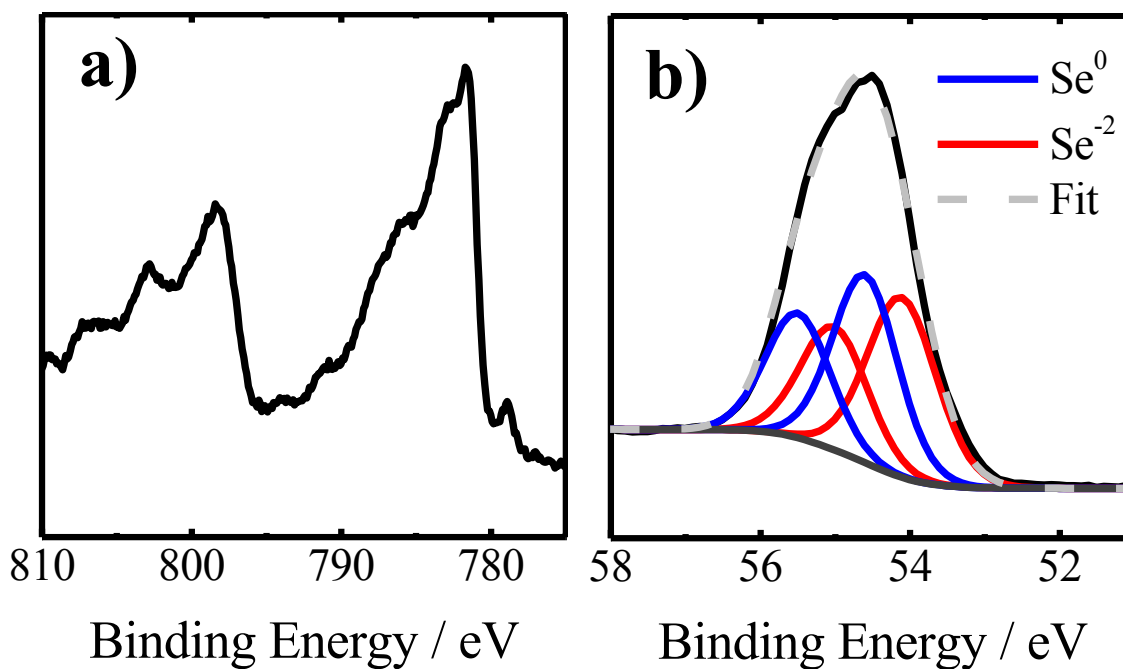


Figure 3.3: Representative high-resolution X-ray photoelectron spectra of an electrochemically prepared cobalt selenide film in the (A) Co 2p and (B) Se 3d regions.

Figure 3.4A presents the cathodic polarization behavior of a cobalt selenide film, as well as that of a bare titanium substrate, in a three-electrode voltammetric configuration in an aqueous solution of 0.500 M H₂SO₄ that was saturated with 1 atm of H₂ (g). The overpotentials required to produce current densities of -10 mA cm⁻² and -25 mA cm⁻² at a cobalt selenide film were 135 ± 2 mV and 160 ± 3 mV (mean ± s.d.), respectively, based on six independently prepared films. The Ti substrate exhibited negligible current densities throughout the interrogated potential window. Titanium is an ineffective HER catalyst and thus provides a clean background for interrogating the HER activity of other materials. Figure 3.4B presents a Tafel plot (overpotential versus log [[current density]]) derived from the voltammetric data of Figure 3.4A. A Tafel slope of

62 mV dec⁻¹ and an exchange current density of 6.4×10^{-2} mA cm⁻² were derived from the region between 110 and 180 mV in overpotential. The 62 mV dec⁻¹ Tafel slope is inconsistent with the predicted values for the HER in acidic solution at room temperature characteristic of the Volmer (~ 120 mV dec⁻¹), Heyrovsky (~ 40 mV dec⁻¹) or Tafel (~ 30 mV dec⁻¹) elementary reactions.^{16, 17} Slopes of ~ 60 mV dec⁻¹ may be observed when either the Heyrovsky or the Tafel reaction is rate-limiting if the adsorption of hydrogen atoms onto the electrode requires an activation energy.¹⁸ The ~ 60 mV dec⁻¹ Tafel slope is consistent with the value observed for several amorphous molybdenum sulfide catalysts.⁵

6

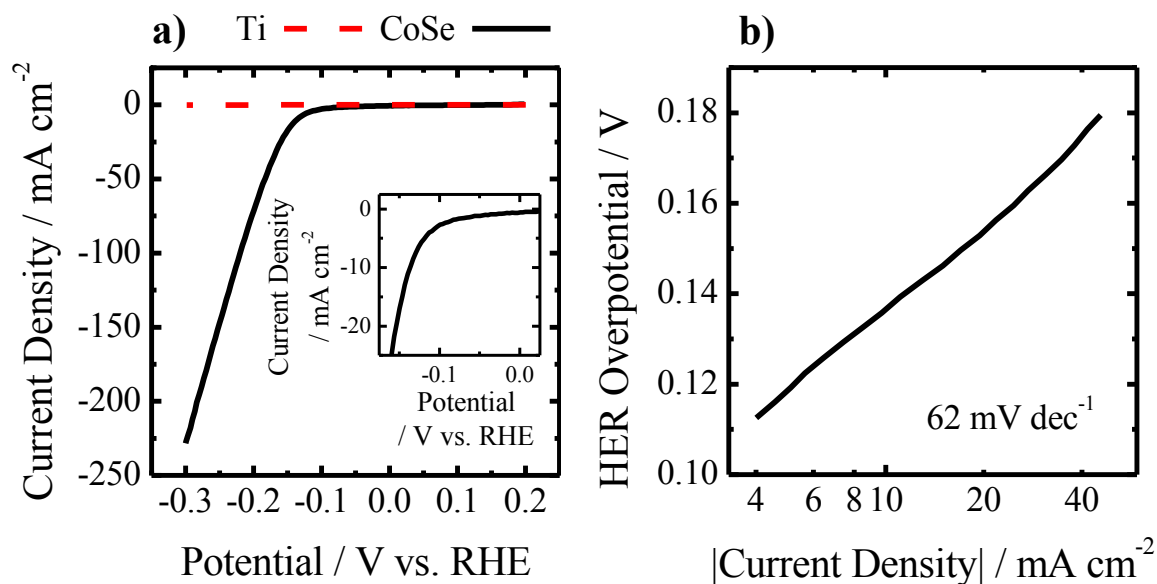


Figure 3.4: (A) Cathodic polarization curves of titanium foil and of a cobalt selenide film in 0.500 M H₂SO₄ saturated with H₂(g) (inset highlights behavior at low overpotentials). (B) Tafel plot derived from data in (A).

Turnover frequencies (TOFs) exhibited by the cobalt selenide films for the HER were derived from the voltammetric data by a method previously reported for an amorphous molybdenum sulfide film (see the experimental section for calculation details).⁶ A plot of the TOF as a function of HER overpotential is presented in Figure 3.5. TOF values were estimated to be 1 s^{-1} at an overpotential of 100 mV and of 5 s^{-1} at an overpotential of 150 mV.

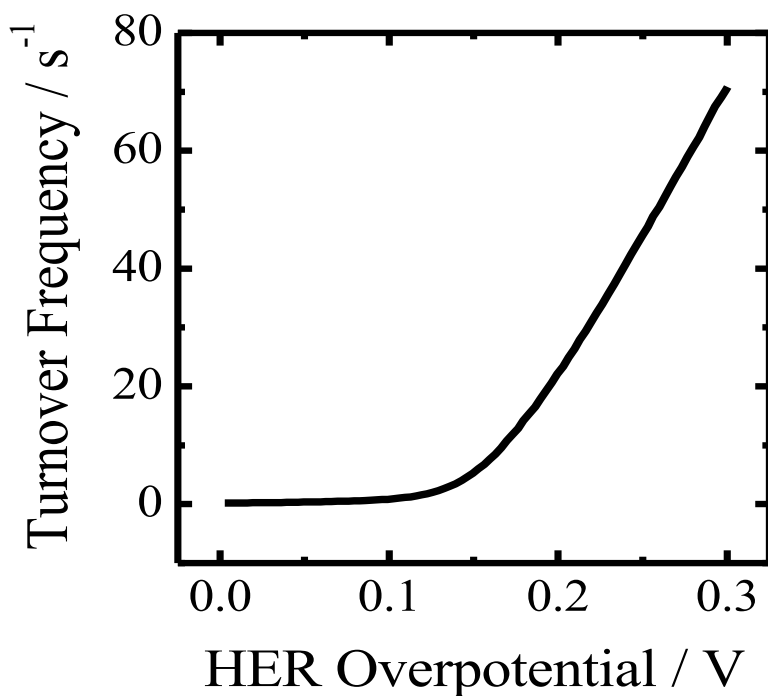


Figure 3.5: Turnover frequency of cobalt selenide films as function of overpotential for the hydrogen-evolution reaction in 0.500 M H_2SO_4 saturated with $\text{H}_2(\text{g})$ derived from the voltammetric data in Figure 3.4A.

The stability of the as-prepared CoSe films during electrochemical hydrogen evolution was assessed by two independent experimental protocols. First, a current

density of -10 mA cm^{-2} was maintained galvanostatically and the electrode potential was monitored as a function of time (Figure 3.6A). Over 16 h of continuous operation, the overpotential required to maintain this current density increased by $\sim 5 \text{ mV}$. Separately, an accelerated degradation study^{3, 19} was performed wherein the electrode potential was swept repeatedly between 0.100 and -0.175 V vs. RHE for 1000 full cycles. Voltammograms recorded before and after cycling (Figure 3.6B) revealed that the overpotential required to achieve current densities of -10 mA cm^{-2} and -25 mA cm^{-2} increased by less than 5 mV in both cases. The catalytic stability of the CoSe films during the HER in $0.5 \text{ M H}_2\text{SO}_4$ is consistent with that displayed by polycrystalline cobalt diselenide films prepared by treating metallic cobalt films with Se vapor, but is in contrast to that displayed by electrodeposited amorphous Co-S films which quickly dissolve under these conditions.^{2, 3} These observations are consistent with the fact that in solutions with $\text{pH} < 4$, Se is cathodically stable until at least -0.4 V vs. RHE , whereas the reduction of S to H_2S is thermodynamically possible at potentials $> 0 \text{ V vs. RHE}$.²⁰

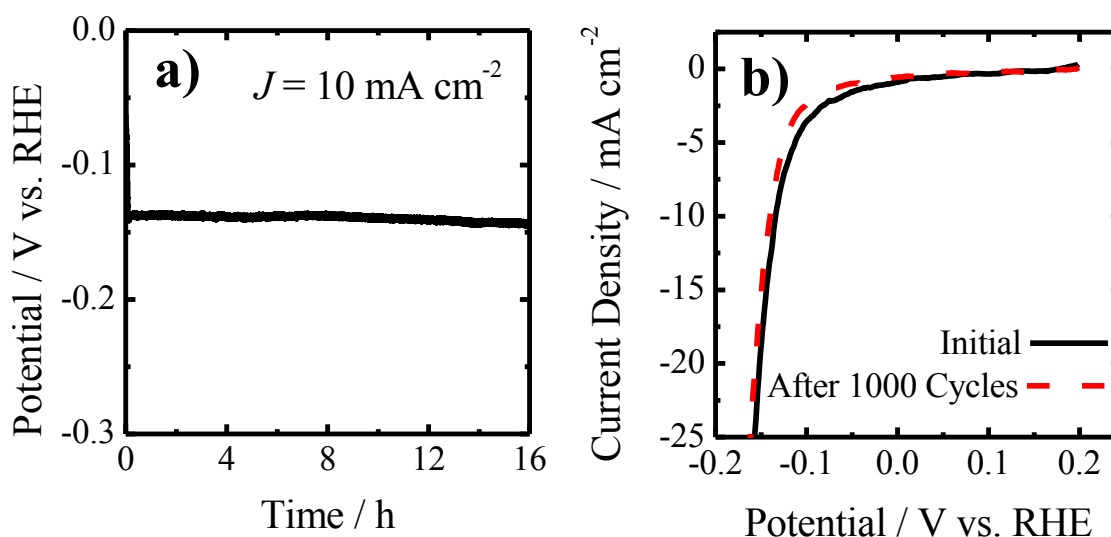


Figure 3.6: (A) Potential applied to a cobalt selenide film as a function of time during galvanostatic electrolysis at -10 mA cm^{-2} in $0.500 \text{ M H}_2\text{SO}_4$ (B) Polarization curves of a cobalt selenide film acquired before and after 1000 accelerated full potential cycles between 0.100 V and -0.175 V vs. RHE.

3.3 Comparison with other HER Catalysts

The $\sim 135 \text{ mV}$ overpotential for effecting current densities of -10 mA cm^{-2} in $0.500 \text{ M H}_2\text{SO}_4$ exhibited by the cobalt selenide films described in this work compares well to the values for other stable and highly-active catalyst materials in acidic media that are composed of Earth-abundant elements. Defective and disordered ultrathin nanosheets of MoS_2 as well as nanosheets of the 1T-MoS_2 polymorph have been demonstrated to achieve -10 mA cm^{-2} with overpotentials in the range of $180 - 190 \text{ mV}$.²¹⁻²³ MoS_2 /reduced graphene oxide composites have reached current densities of -10 mA cm^{-2} with an overpotential of $\sim 160 \text{ mV}$.¹⁹ Ni_2P nanoparticles have been shown to drive

current densities of -10 mA cm^{-2} with an overpotential of $\sim 120 \text{ mV}$.²⁴ Notably, the cobalt selenide films described herein were prepared entirely at room temperature and ambient conditions, via a facile electrochemical method. As synthesized, the amorphous Se matrix containing the CoSe may not act as a good electrical conductor, so the activity reported in this work may represent a lower bound on the true electrocatalytic activity of the material.²⁵ Additionally, Mo_2C supported on carbon nanotubes and amorphous MoS_x coated on N-doped carbon nanotubes have been shown to effect current densities of -10 mA cm^{-2} with overpotentials of $\sim 150 \text{ mV}$ and 110 mV , respectively.^{26, 27} Similarly, nanoparticles of CoSe_2 have achieved -10 mA cm^{-2} with an overpotential of 137 mV when deposited on a high-surface area, porous, three-dimensional electrode (carbon fiber paper).⁴ Fabrication of a similar structured composite with electrochemically prepared cobalt selenide may thus lead to improved performance. Similarly, deposition with dynamic potential-time waveforms, as well as alloying with Fe or Ni as has been done to promote the activity of molybdenum sulfide, could also prove effective for increasing the activity of cobalt selenide-based materials.^{28, 29}

3.4 Conclusion

In conclusion, cobalt selenide films prepared by a simple electrochemical method under ambient conditions have demonstrated significant electrocatalytic activity and stability for catalysis of the HER in strongly acidic aqueous solution. This work suggests that electrochemically synthesized metal chalcogenide materials are promising catalysts for applications involving the HER, especially for applications involving the direct

production of fuels from sunlight in solar-driven water splitting systems.^{30, 31} Moreover, investigations of deposition on structured supports, complex potential-time waveforms for electrodeposition, and alloying with other transition metals, as have been demonstrated for MoS₂, may result in further enhancements of the HER activity of such materials.^{5, 32}

3.5 Experimental

Materials and Chemicals: H₂(g) (99.999%, Air Liquide), H₂SO₄ (J.T. Baker, A.C.S. Reagent), Ti foil (99.7+%, 0.127 mm thick, Sigma-Aldrich), SeO₂ (99.999%, Acros Organics), Co(C₂H₃O₂)₂·4H₂O (98%, Strem Chemicals) and LiCl (≥ 99.0%, Sigma-Aldrich) were used as received. H₂O with a resistivity ≥ 18.2 MΩ cm⁻¹ (Barnsted Nanopure System) was used throughout.

Cobalt Selenide Electrodeposition: Cobalt selenide films were prepared on Ti substrates via electrodeposition. The sealed, single-compartment electrochemical cell equipped with a graphite-rod counter electrode (Alfa Aesar, 99%) and a Ag/AgCl reference electrode (3 M KCl; Bioanalytical Systems) that were collectively controlled by a Bio-Logic SP-200 potentiostat. Squares ~ 2 cm x 2 cm in dimension were cut from the Ti foil and were then sealed into an O-ring compression cell that confined the contact region between the electrolyte, an aqueous solution of 0.065 M Co(C₂H₃O₂)₂, 0.035 M SeO₂ and 0.200 M LiCl (pH = 4.7), and the Ti foil, to a circular area of 0.1 cm². An external electrical contact to the Ti foil was made using an alligator clip. Electrodeposition was effected by potentiostatically biasing the Ti at a potential of -0.45

V vs. the Ag/AgCl reference electrode for 8 h at room temperature. After deposition, the Ti foil pieces were removed from the compression cell and rinsed first with 0.500 M H₂SO₄ and then with H₂O. The area of the Ti substrate that had not been covered by the electrodeposited cobalt selenide was then covered with nitrocellulose-based nail polish to provide electrical insulation.

Electrochemical Conditioning and Analysis: A single-compartment cell equipped with a graphite-rod counter electrode and a saturated calomel electrode (SCE; CH Instruments) and controlled by a Bio-Logic SP-200 potentiostat was used for conditioning and analysis of the electrodeposited material. An O-ring compression seal was used to mount the Ti substrate that supported the electrodeposited material in the cell. All experiments were performed using an aqueous solution of 0.500 M H₂SO₄ that was continuously sparged with H₂(g) and stirred using a magnetic stir bar. The potential of a reversible hydrogen electrode (RHE) relative to the SCE was determined by measuring the potential of a Pt foil (which was annealed in a H₂-air flame immediately prior to use) in the H₂(g)-saturated 0.500 M H₂SO₄ electrolyte. All quoted potentials are referenced against RHE unless otherwise noted. Prior to voltammetric experiments and physical characterization, electrodes were preconditioned by galvanostatic electrolysis at a current density of -10 mA cm⁻² for 1 h. The CoSe mass loading was determined to be 3 mg cm⁻². The uncompensated cell resistance (R_u) was determined from a single-point electrochemical impedance measurement obtained by applying a sine-wave modulated potential with amplitude of 20 mV at a modulation frequency of 100 kHz centered at the open-circuit potential of the cell. All subsequent measurements were corrected for an uncompensated resistance of 85% of the value of R_u . Voltammetric data were recorded at

a scan rate of 1 mV s^{-1} . The electrochemical stability of the cobalt selenide films was assessed using both galvanostatic and accelerated degradation techniques. First, a current density of -10 mA cm^{-2} was maintained galvanostatically and the electrode potential was monitored over the course of 16 h. Separately, the cobalt selenide films were subjected to 1000 full potential cycles between -0.175 V and 0.1 V vs. RHE at a sweep rate of 50 mV s^{-1} . Voltammograms at a sweep rate of 1 mV s^{-1} were recorded before cycling and after completion of the 1000 full potential cycles.

Physical Characterization: Scanning electron microscopy (SEM) was conducted using a FEI Nova NanoSEM 450 at an accelerating voltage of 15 kV with a working distance of 5 mm and an in-lens secondary electron detector. Energy-dispersive X-ray spectroscopy was performed in the SEM at a working distance of 12 mm, using an accelerating voltage of 15 kV and an Oxford Instruments silicon drift detector. Raman spectra were obtained with a Renishaw inVia spectrometer equipped with a Leica microscope, a Leica N Plan 50x objective (numerical aperture = 0.75), an $1800 \text{ lines mm}^{-1}$ grating, and a CCD detector in a 180° backscatter geometry. A 532 nm diode-pumped solid state (DPSS) laser (Renishaw RL532C50) was used as the excitation source and a radiant power of $20 \text{ }\mu\text{W}$ was incident on the sample. X-ray diffraction (XRD) powder patterns were acquired with a Bruker D8 Discover diffractometer equipped with a $\text{Cu K}\alpha$ source and a 2-dimensional Vantec detector. X-ray photoelectron spectra (XPS) were acquired with a Kratos Axis Nova spectrometer at a base pressure of 10^{-9} torr with monochromatic $\text{Al K}\alpha$ excitation at 1486.7 eV. High-resolution spectra were obtained using a pass energy of 40 eV. CasaXPS software (CASA Ltd) was used to fit peaks in the XP spectra, and peak fitting was performed assuming a Shirley background and

symmetric Voigt line-shapes comprised of Gaussian (70%) and Lorentzian (30%) functions. The peak fitting was constrained to maintain both a 2:3 ratio between the areas of the Se 3d_{3/2} and Se 3d_{5/2} lines and to maintain a 0.85 eV separation between the binding energies of these two lines.

Calculation of turnover frequencies: Turnover frequencies of the cobalt selenide films for the hydrogen-evolution reaction were calculated the method previously reported for an amorphous molybdenum sulfide catalyst film.³⁵ The number of surface sites per unit area was estimated by calculating the area occupied by a CoSe unit in freboldite to determine the number of surface sites for a planar material and then scaling this value by the roughness factor of the cobalt selenide film (13, determined via electrochemical capacitance measurements). The selenium-selenium distance in frebdolite is 0.361 nm. Based on the arrangement of selenium atoms in the frebdolite basal plane, each Se atom, and thus each CoSe unit, occupies 0.13 nm². Thus, freboldite has approximately 8 x 10¹⁴ surface sites per cm² in the basal plane. From this, it is estimated that the cobalt selenide films had approximately 1 x 10¹⁶ surface sites per cm². The total number of hydrogen evolution turnovers was analytically derived from the current density via the conversion factor 3.1 x 10¹⁵ H₂ s⁻¹ mA⁻¹. The turnover frequency is then the total number of turnovers divided by the number of active sites. Figure 3.5 presents a plot of turnover frequency as function of hydrogen-evolution reaction overpotential derived from the data in Figure 3.4A.

3.6 References

1. Y. F. Xu, M. R. Gao, Y. R. Zheng, J. Jiang and S. H. Yu, *Angew. Chem. Int. Ed.*, 2013, **52**, 8546-8550.
2. Y. Sun, C. Liu, D. C. Grauer, J. Yano, J. R. Long, P. Yang and C. J. Chang, *J. Am. Chem. Soc.*, 2013, **135**, 17699-17702.
3. D. Kong, J. J. Cha, H. Wang, H. R. Lee and Y. Cui, *Energy Environ. Sci.*, 2013, **6**, 3553.
4. D. Kong, H. Wang, Z. Lu and Y. Cui, *J. Am. Chem. Soc.*, 2014, **136**, 4897-4900.
5. D. Merki, S. Fierro, H. Vrubel and X. Hu, *Chem. Sci.*, 2011, **2**, 1262.
6. J. D. Benck, Z. Chen, L. Y. Kuritzky, A. J. Forman and T. F. Jaramillo, *ACS Catal.*, 2012, **2**, 1916-1923.
7. E. Anastassakis, *Solid State Commun.*, 1973, **13**, 1297-1301.
8. G. Lucovsky, A. Mooradian, W. Taylor, G. B. Wright and R. C. Keezer, *Solid State Commun.*, 1967, **5**, 113-117.
9. S. N. Yannopoulos and K. S. Andrikopoulos, *J. Chem. Phys.*, 2004, **121**, 4747-4758.
10. S. N. Yannopoulos and K. Andrikopoulos, *Phys. Rev. B*, 2004, **69**, 114206.
11. C. E. M. Campos, J. C. de Lima, T. A. Grandi, K. D. Machado and P. S. Pizani, *Physica B*, 2002, **324**, 409-418.
12. V. G. Hadjiev, M. N. Iliev and I. V. Vergilov, *J. Phys. C Solid State*, 1988, **21**, L199-L201.
13. D. Gallant, M. Pézolet and S. Simard, *J. Phys. Chem. B*, 2006, **110**, 6871-6880.

14. J. Tyczkowski, R. Kapica and J. Łojewska, *Thin Solid Films*, 2007, **515**, 6590-6595.
15. H. van der Heide, R. Hemmel, C. F. van Bruggen and C. Haas, *J. Solid State Chem.*, 1980, **33**, 17-25.
16. N. Pentland, J. O. Bockris and E. Sheldon, *J. Electrochem. Soc.*, 1957, **104**, 182-194.
17. B. E. Conway and B. V. Tilak, *Electrochim. Acta*, 2002, **47**, 3571-3594.
18. J. G. N. Thomas, *Trans. Faraday Soc.*, 1961, **57**, 1603-1611.
19. Y. Li, H. Wang, L. Xie, Y. Liang, G. Hong and H. Dai, *J. Am. Chem. Soc.*, 2011, **133**, 7296-7299.
20. M. Pourbaix, *Atlas of Electrochemical Equilibria In Aqueous Solutions*, Pergamon Press, Oxford, 1966.
21. J. Xie, H. Zhang, S. Li, R. Wang, X. Sun, M. Zhou, J. Zhou, X. W. Lou and Y. Xie, *Adv. Mater.*, 2013, **25**, 5807-5813.
22. J. Xie, J. Zhang, S. Li, F. Grote, X. Zhang, H. Zhang, R. Wang, Y. Lei, B. Pan and Y. Xie, *J. Am. Chem. Soc.*, 2013, **135**, 17881-17888.
23. M. A. Lukowski, A. S. Daniel, F. Meng, A. Forticaux, L. Li and S. Jin, *J. Am. Chem. Soc.*, 2013, **135**, 10274-10277.
24. E. J. Popczun, J. R. McKone, C. G. Read, A. J. Biacchi, A. M. Wiltrout, N. S. Lewis and R. E. Schaak, *J. Am. Chem. Soc.*, 2013, **135**, 9267-9270.
25. K. E. Murphy, B. B. Wunderlich and B. Wunderlich, *J. Phys. Chem.*, 1982, **86**, 2827-2835.

26. W. F. Chen, C. H. Wang, K. Sasaki, N. Marinkovic, W. Xu, J. T. Muckerman, Y. Zhu and R. R. Adzic, *Energy Environ. Sci.*, 2013, **6**, 943.
27. D. J. Li, U. N. Maiti, J. Lim, D. S. Choi, W. J. Lee, Y. Oh, G. Y. Lee and S. O. Kim, *Nano Lett.*, 2014, **14**, 1228-1233.
28. D. Merki, H. Vrubel, L. Rovelli, S. Fierro and X. Hu, *Chem. Sci.*, 2012, **3**, 2515.
29. X.-J. Lv, G.-W. She, S.-X. Zhou and Y.-M. Li, *RSC Advances*, 2013, **3**, 21231.
30. S. Haussener, C. Xiang, J. M. Spurgeon, S. Ardo, N. S. Lewis and A. Z. Weber, *Energy Environ. Sci.*, 2012, **5**, 9922.
31. J. R. McKone, N. S. Lewis and H. B. Gray, *Chem. Mater.*, 2014, **26**, 407-414.
32. Z. Chen, D. Cummins, B. N. Reinecke, E. Clark, M. K. Sunkara and T. F. Jaramillo, *Nano Lett.*, 2011, **11**, 4168-4175.

Chapter 4

CoP As An Acid-Stable Active Electrocatalyst For The Hydrogen-Evolution Reaction: Electrochemical Synthesis, Interfacial Characterization And Performance Evaluation

Saadi, F. H.; Carim, A. I.; Verlage, E.; Hemminger, J. C.; Lewis, N. S.; Soriaga, M. P. *The Journal of Physical Chemistry C* **2014**, *118*, 29294. DOI: 10.1021/jp5054452

4.1 Introduction

The previous two chapters have focused on acid-stable, earth-abundant HER catalysts that consist of Group VI transition metals and chalcogenides. Another family of promising hydrogen evolution catalysts that was discovered during my time at Caltech is the transition metal phosphide group. Recently, crystalline nanoparticles of Ni₂P, MoP, and CoP have been reported as acid-compatible HER catalysts that exhibit low overpotentials in acidic electrolytes.¹⁶⁻²¹ Additionally, Ni-P and Co-P alloys have been studied as alkaline-stable HER catalysts, although the exact compositions and activities were irreproducible among different samples.²²⁻²⁶ In this chapter we describe a facile electrochemical method for the synthesis of a cobalt phosphide film that displays high HER activity and significant *operando* acid-stability.

4.2 Cobalt phosphide electrodeposition and characterization

4.2.1 Characterization of films prior to electrocatalysis

Scanning-electron micrographs (SEM) of the as-deposited thin film (Figures 4.1A, 4.1B, and 4.1C) showed the surfaces to be relatively smooth but with micron-sized spherical clusters randomly and loosely distributed throughout. Energy-dispersive X-ray spectroscopy (EDS) indicated that the surface was composed primarily of cobalt and a minor amount of phosphorous in a Co:P ratio of 20:1 (Figure 4.2). EDS also yielded the same 20:1 ratio for the clusters.

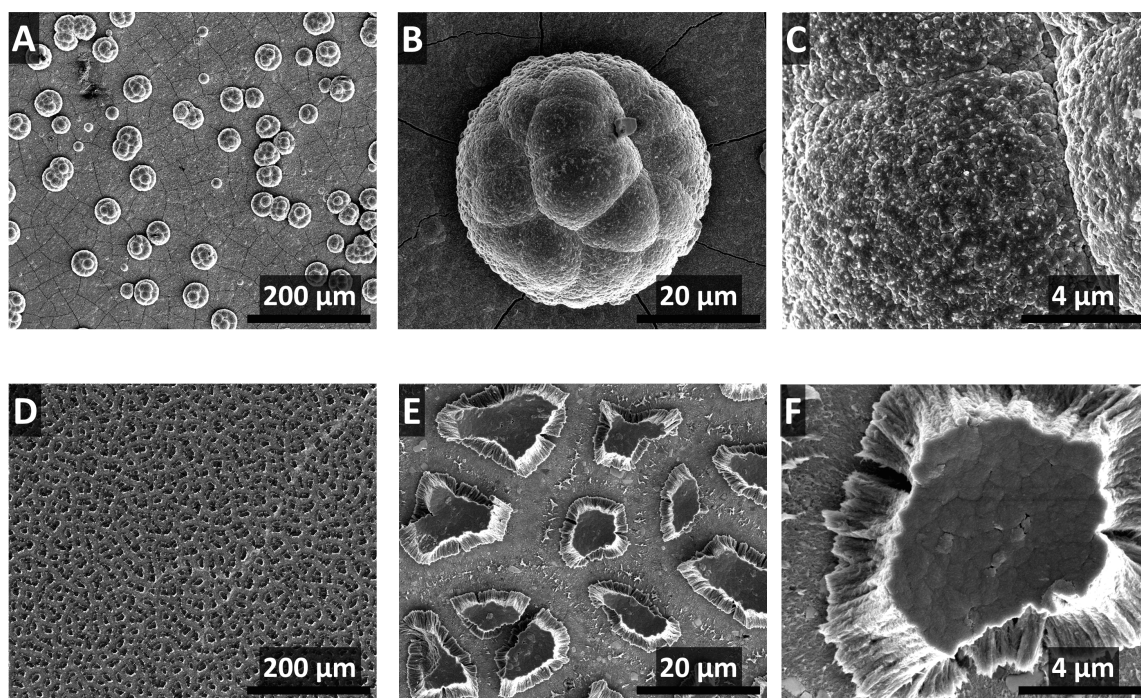


Figure 4.1: Scanning-electron micrographs of the films before (A, B, and C) and after (D, E, and F) voltammetry. A: An As-deposited thin film showed the presence of quasi-spherical clusters on the surface. B and C: The film underneath the particles appeared

uniformly roughened. D: Post-electrolysis film showed close-packed plateau-topped islands on the surface. E and F: The tops of the mesa-like islands were flat and relatively smooth.

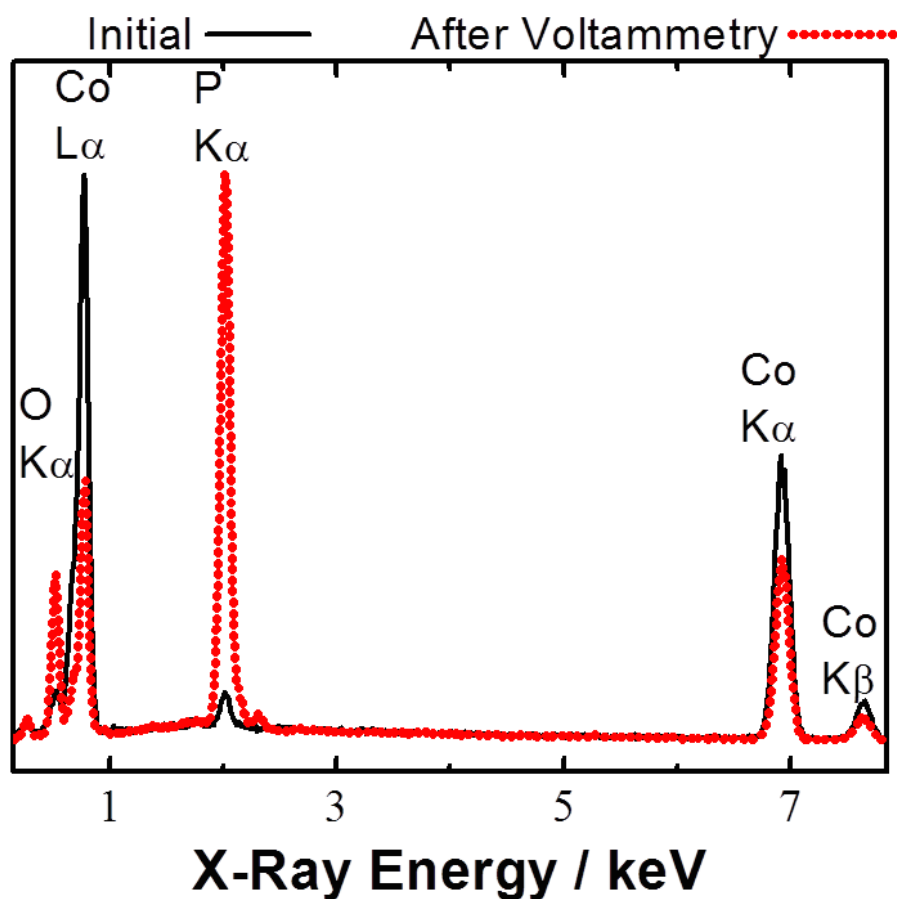


Figure 4.2: Energy-dispersive X-ray spectroscopy of the films before and after voltammetry. The Co:P atomic ratio decreased from 20:1 to 1:1 after the voltammetric experiments.

Figures 4.3A and 4.3B show high-resolution X-ray photoelectron spectra of the samples in the Co and P regions, respectively. The peaks at 778 eV and 793 eV in Figure

4.3A correspond to the $2p_{3/2}$ and $2p_{1/2}$ peaks of zerovalent Co. All of the other peaks are associated with oxidized cobalt, Co_3O_4 ($\text{CoO}\cdot\text{Co}_2\text{O}_3$).²⁸⁻³¹ The large peak in Figure 4.3B at 133 eV is assigned to orthophosphate, probably as the cobalt salt $\text{Co}_3(\text{PO}_4)_2$.^{32,33} The observed broadening is consistent with an unresolved overlap of the $2p_{3/2}$ and $2p_{1/2}$ states.³⁴ Based on Equation (4.1), the Co:P atomic ratio was determined to be 8:1. The latter is considerably smaller than the EDS-determined ratio (20:1) because X-rays emanate deeper from the sample bulk compared to photoemitted electrons. This difference in the Co:P ratio implies surface segregation of phosphorus in the as-prepared sample.

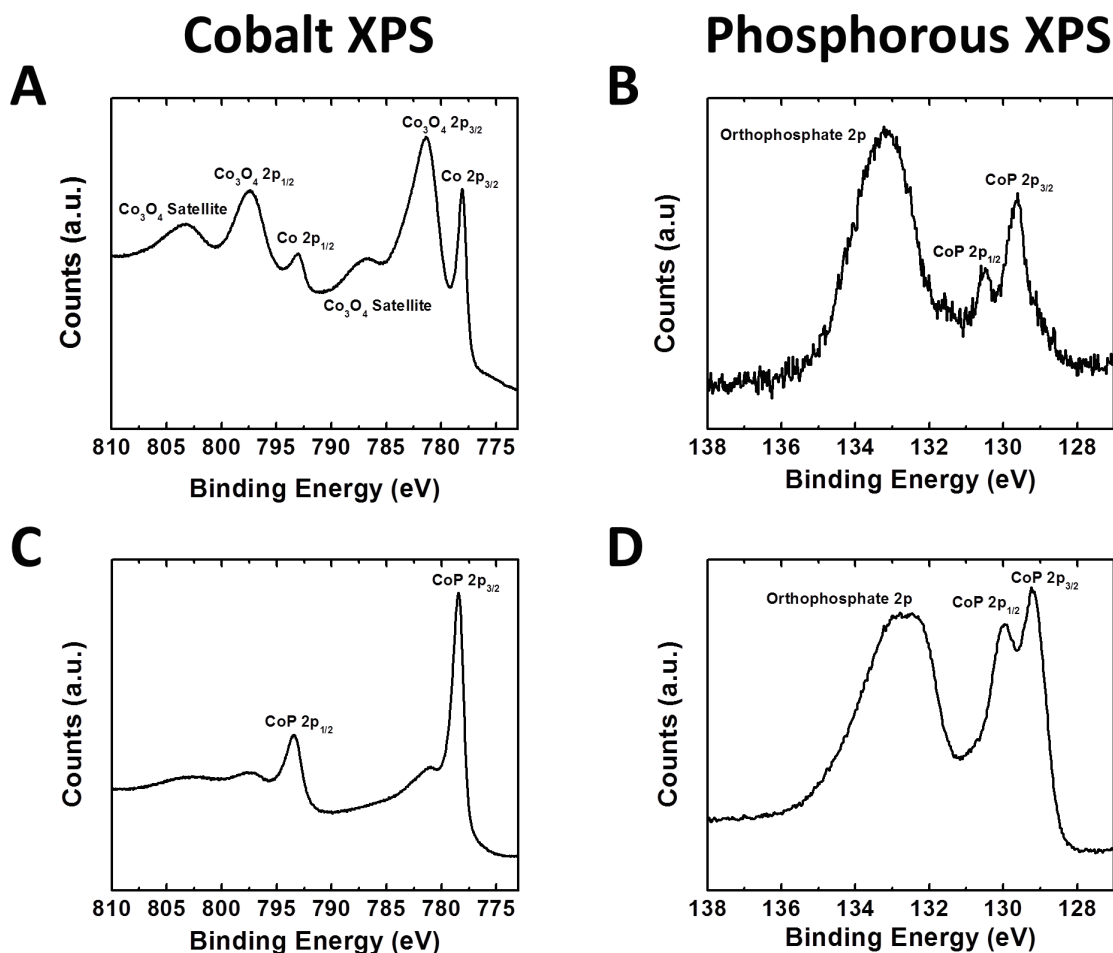


Figure 4.3: High-resolution X-ray photoelectron spectra of (A) Co 2p region of the as-deposited thin film; (B) P 2p region of the as-deposited thin film; (C) Co 2p region after voltammetry; (D) P 2p region after voltammetry.

The Raman spectrum of the as-deposited cobalt phosphide film (Figure 4.4) exhibited a broad, asymmetric band centered at 590 cm^{-1} which is characteristic of amorphous cobalt oxide³⁵. The shoulders at 487 , 522 , and 690 cm^{-1} are consistently assigned to Co_3O_4 stretching modes (E_g , F_{2g} , and A_{1g}).³⁶ Additional peaks at 925 , 981 and 1067 cm^{-1} were also observed and are consistent with P-O stretching modes (ν_1 symmetric, ν_1 symmetric, and ν_3 anti-symmetric respectively).^{37,38}

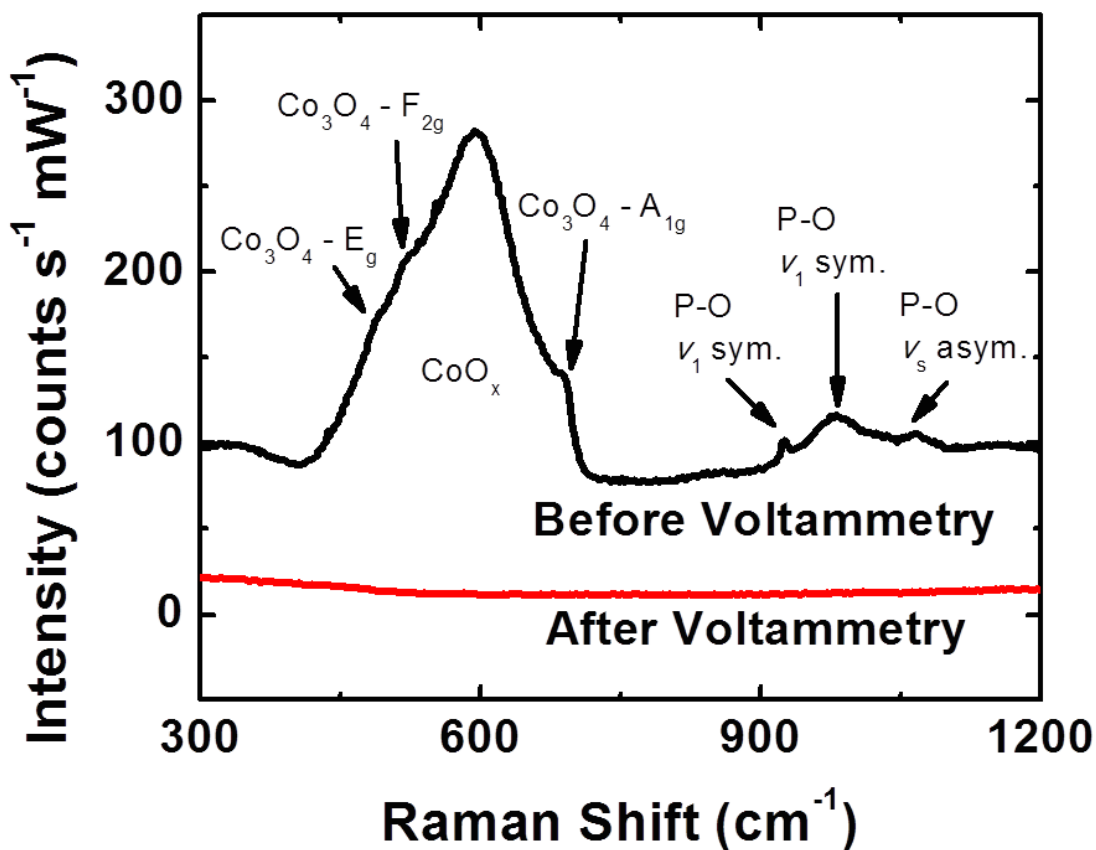


Figure 4.4: Raman spectra before and after voltammetry. The peaks at *ca.* 600 cm^{-1} correspond to Co-O vibrational modes, whereas those at *ca.* 1100 cm^{-1} are attributable to P-O modes.

4.2.2 Electrochemistry

Figure 4.5 displays the cyclic current vs. potential data for the cobalt phosphide thin film in aqueous 0.500 M H_2SO_4 . In the first scan (Figure 4.5A), initially from the open-circuit potential (-0.075 V) to 0.025 V vs RHE, a large anodic current was observed that was not replicated in subsequent runs. After that first cycle, in all experiments, the overpotential (η) needed to drive 10 mA cm^{-2} of cathodic current was 85 mV (RHE). This overpotential was significantly lower than those observed for the Co-on-Cu and pure-Cu control experiments (Figure 4.5B). Figure 4.5C shows a representative steady-state Tafel plot for the cobalt-phosphide film, which yielded a slope of 50 mV dec^{-1} and an exchange current density of 0.20 mA cm^{-2} . Figure 4.5D compares the Tafel plot of the subject compound with those of other HER catalysts. Only platinum outperformed the electrodeposited cobalt-phosphide film under the stated test conditions.

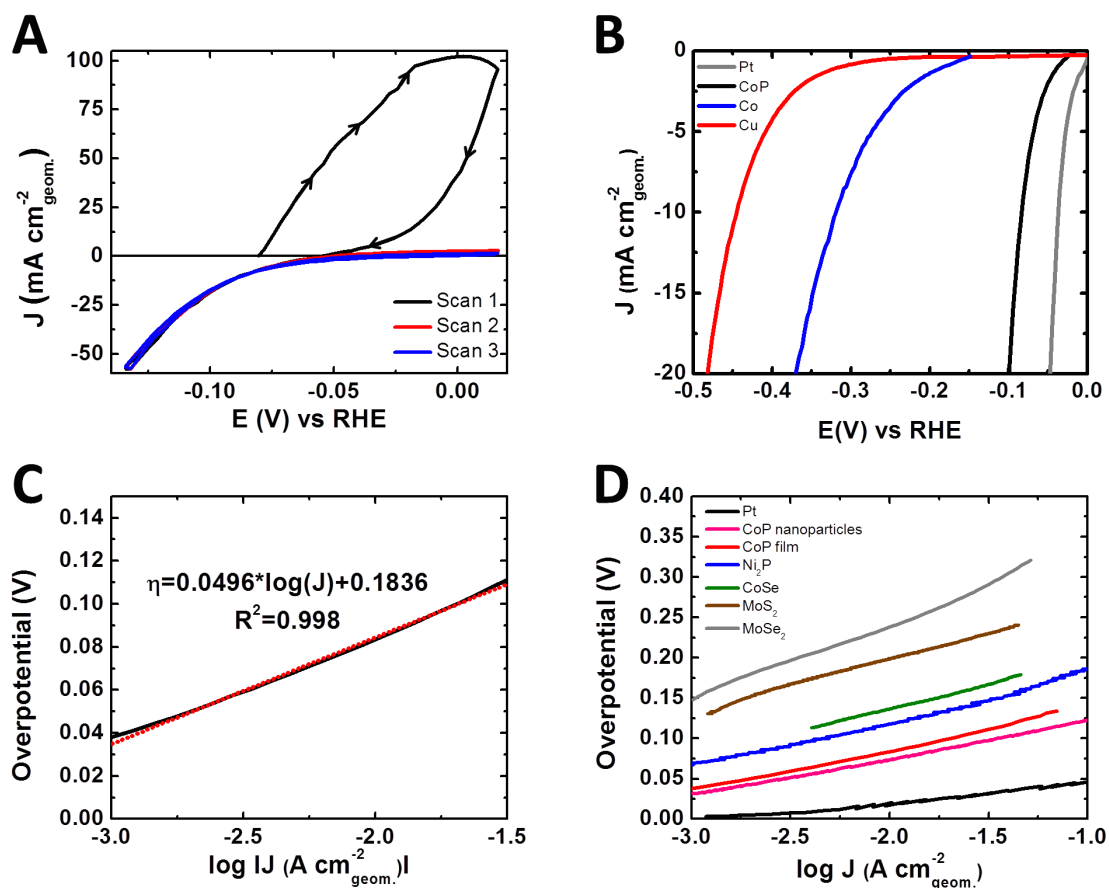


Figure 4.5: (A) Cyclic voltammetric data for cobalt phosphide thin films on glassy carbon in aqueous 0.50 M H₂SO₄. (B) Current density vs potential data for Pt (gray), the third scan of CoP (black), Co (blue) and Cu (red). (C) Tafel plot of CoP from the current density vs potential data in (B). (D) Tafel plots that compare the activity of the film in 0.50 M H₂SO₄ with that of Pt,²¹ CoP nanoparticles,²¹ Ni₂P nanoparticles,²⁰ CoSe thin films,⁴¹ MoSe₂ thin films,⁴² and MoS₂ thin films.⁹

Two methods were implemented to assess the *operando* stability of the catalytically active film in highly acidic environments. In one, the sample was cycled,

uninterrupted, between 0.0 V and -0.14 V vs RHE in 0.5 M H₂SO₄ for 24 h and the ensuing cyclic voltammogram (CV) was compared with that for first cycle (Figure 4.6A). The CV data indicated an increase in η from 85 mV to 100 mV after the day-long test. The other stability-assessment method was based on chronopotentiometry, in which a constant current density of 10 mA cm⁻² was delivered over 24 h while the electrode potential, i.e. the value of η , was monitored (Figure 4.6B). The average increase in η from the two methods was 17.5 ± 4.5 mV.

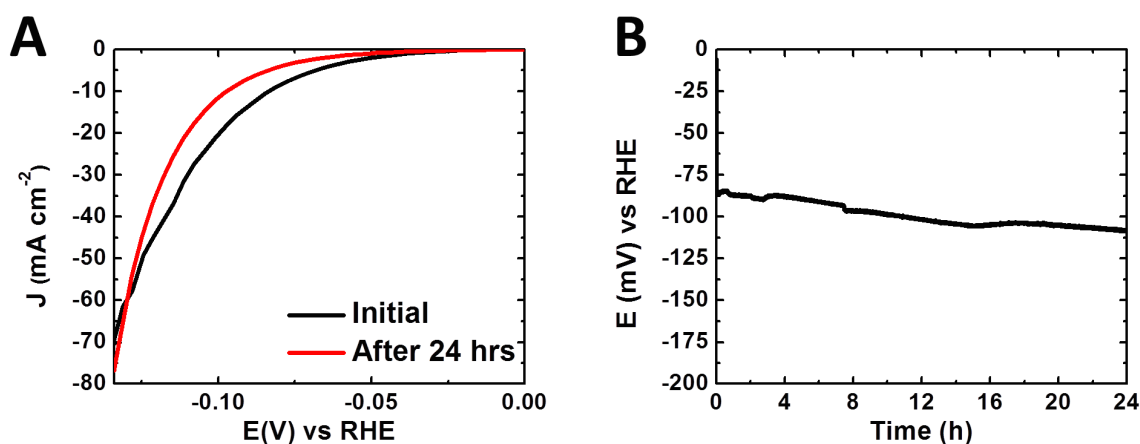


Figure 4.6: (A) Current density vs potential data in 0.50 M H₂SO₄, for the first cycle and after uninterrupted scans over 24 h. (B) Chronopotentiometry in 0.50 M H₂SO₄ at a constant current density of 10 mA cm⁻².

4.2.3 Post-electrochemistry film characterization

Figures 4.1D, 4.1E, and 4.1F show SEM images of the film obtained after the HER catalysis experiments. The most notable difference between these images and the pre-electrochemistry images of Figures 4.1A, 4.1B, and 4.1C is that the film surface was

no longer marred with loosely distributed quasi-spheres but was instead covered with close-packed plateau-topped particles that resembled micron-sized mesas. The tops of the mesa-like particles were relatively flat and smooth. Post-electrochemistry EDS measurements (Figure 4.2) indicated that Co:P ratio in the film decreased twenty-fold to 1:1.

Figures 4.3C and 4.3D, respectively, show high-resolution XPS spectra of the sample in the Co and P regions. Comparison of Figure 4.3C with Figure 4.3A clearly indicates that all peaks attributable to cobalt oxides have diminished; the two major peaks represent Co 2p_{3/2} and Co 2p_{1/2} states in the stoichiometric CoP.^{21,32,39} Close inspection of Figures 4.3B and 4.3D reveals that the relative intensities of the post-electrochemistry phosphide peaks at 129 and 131 eV increased, whereas that of the phosphate peak at 133 eV decreased significantly. Based on Equation (4.1), the atomic ratio of cobalt and phosphorous after the hydrogen-evolution experiments decreased from 8:1 to 1:1, in agreement with the EDS results.

The Raman spectrum (Figure 4.4) after electrochemistry showed the absence of peaks at 600 cm⁻¹, thus providing clear evidence that the catalytically active film did not contain cobalt oxide.

4.3 Discussion

When a clean copper disk electrode is immersed in an aqueous solution of 0.15 M H₃BO₃, 0.10 M NaCl, 0.30 M NaPO₂H₂, and 0.2 M CoCl₂ and applied with a potential of -1.2 V, the following deposition reactions are expected to occur:⁴⁰





A spontaneous Co-P compound formation reaction then occurs to give the net reaction:



While a few stoichiometric compositions of cobalt phosphide are known (e.g., Co_3P and Co_2P),^{25,32} the 1:1 ratio explicitly shown in Equation (4.2) is based upon the post-electrocatalysis XPS, and EDS results. The as-deposited film, whether examined by EDS, XPS or Raman spectroscopy, showed a preponderance of higher-valent Co and P species such as Co_2O_3 , CoO , and orthophosphate salts. This behavior may be a consequence of the air-oxidation of the sample when removed from the deposition solution, rinsed with Nanopure water, and transferred to the XPS instrument.

The large anodic current observed in the first voltammetric cycle is consistent with expectations for the quantitative anodic dissolution of metallic cobalt to the divalent cation, Co^{2+} , which is desorbed into solution. Under HER conditions, dissolution of CoO and Co_2O_3 evidently also takes place as indicated by the complete loss of cobalt oxides, as well as by the significant decrease in the Co:P atomic ratio observed in the post-catalysis XPS and EDS data. The magnitude of the orthophosphate XPS peak in the as-prepared sample was substantially diminished after the HER cycles. This decrease was consistent with expectations for the cathodic reduction of interfacial orthophosphate species; when the film was removed from solution, in the absence of applied potential, the reduced products readily reverted to the orthophosphates. Thus, *ex-situ* surface spectroscopy showed non-zero, but substantially diminished, orthophosphate coverage; this is as expected for samples that were briefly exposed to air during sample transfer. The net result is an example of an *operando* purification, with the deposit changing

chemically from a composite of active and inert substances to solely the catalytically functional material.

For the electrodeposited cobalt phosphide film, spectral results from XPS showed that the binding energy of cobalt was significantly lower than either the Co^{2+} or Co^{3+} species. This is to be expected since a previous study on metal monophosphides has revealed the covalent nature of the cobalt-phosphorous bond.³⁹ The covalently bonded CoP is better represented as $\text{Co}^{\delta+}\text{P}^{\delta-}$, where $\delta+$ and $\delta-$ denote partial, non-integer, charges; consequently, the Co peaks would be closer to those of the zerovalent metal. If the interaction between cobalt and phosphorus were purely ionic, the designation would have been $[\text{Co}^{3+}][\text{P}^{3-}]$, and the Co peak would be that for the Co^{3+} species.

The overpotential (η) necessary to deliver a proton-reduction current density of 10 mA cm^{-2} , a catalytic-activity metric that is an order of magnitude higher than in natural photosynthesis, was 85 mV for electrodeposited CoP. In addition, the CoP electrodeposits displayed stability in acidic environments, in that after 24 h of uninterrupted HER-voltammetric cycles, η increased by only $17.5 \pm 4.5 \text{ mV}$. The results for the electrodeposited CoP micron-sized particles are comparable to those obtained using CoP nanoparticles.²¹ In terms of η , the comparative catalytic performance of the CoP film is as follows (Figure 4.5): $\eta_{\text{Pt}} < \eta_{\text{CoP Film}} = \eta_{\text{CoP NP}}, \eta_{\text{Ni}_2\text{P}} < \eta_{\text{CoSe}_2} < \eta_{\text{MoS}_2} < \eta_{\text{MoSe}_2}$.

4.4 Conclusion

Cobalt phosphide was prepared, as a film on a copper substrate, by cathodic deposition from a boric acid solution of Co^{2+} and H_2PO_2^- . Surface structural and

compositional analysis of the film prior to the electrocatalysis measurements indicated that the film consisted of micron-sized spherical clusters located randomly and loosely on a slightly rough surface. The composition of both the clusters and surface consisted of cobalt in the metallic, phosphide, and amorphous-oxide forms ($\text{CoO}\cdot\text{Co}_2\text{O}_3$), and of phosphorus as phosphide and orthophosphate. The higher-valent species that originated from air-oxidation were remediated upon HER electrocatalysis in sulfuric acid. The *operando* film purification yielded a functional electrocatalyst with a Co:P stoichiometric ratio of 1:1. The post-HER surface was densely packed with micron-sized mesa-like particles whose tops were flat and smooth. The CoP electrodeposit showed an overvoltage of 85 mV at a current density of 10 mA cm^{-2} , and exhibited *operando* stability in acidic solution, characterized by an increase in η of 18 mV after 24 h of uninterrupted operation. In terms of η , the comparative catalytic performance of CoP is: $\eta_{\text{Pt}} < \eta_{\text{CoP Film}} \leq \eta_{\text{CoP NP}}$, $\eta_{\text{Ni}_2\text{P}} < \eta_{\text{CoSe}_2} < \eta_{\text{MoS}_2} < \eta_{\text{MoSe}_2}$.

4.5 Experimental

All chemical reagents were analytical grade and used without further purification. Ultra-clean water with resistivity higher than $18.2 \text{ M}\Omega \text{ cm}$ was generated from a Barnstead Nanopure system (Thermo Scientific, Asheville, NC). Unless otherwise specified, all experiments were performed under ambient laboratory conditions.

Rotating-disk electrode substrates. Copper disks (Alfa Aesar, Ward Hill, MA) that were used as deposition substrates were 5 mm diameter, 4 mm thickness, and 99.999 % purity. The disks were metallographically burnished on a LaboPol-5 polisher (Struers

Inc., Cleveland, OH), initially with 15- μ SiC (Buehler, Lake Bluff, IL) and subsequently with progressively decreased grit size (9, 6, 3 to 1 μ) diamond paste. The disks were then cleaned with a 0.06- μ colloidal suspension of silica and sonicated for 5 min in Nanopure water.

Electrochemistry. Electrochemical experiments were performed in a 100-mL four-port glass cell that was equipped with a 99%-pure graphite rod (Alfa Aesar) that served as a counter electrode, and a saturated calomel electrode (SCE) (CH Instruments, Austin, TX) as reference. The SCE was calibrated (266 mV) against a reversible hydrogen electrode (RHE) in 0.5 M H₂SO₄. Potential control was accomplished with a BioLogic SP-200 potentiostat (Biologic, Grenoble, France). The uncompensated cell resistance was determined from a single-point high-frequency impedance measurement and was compensated (85 %) by the built-in positive-feedback software.

The cobalt phosphide film was electrodeposited onto a Cu disk from a 250-mL solution that consisted of 0.928 g (0.15 M) of boric acid, H₃BO₃, (Alfa Aesar), 0.584 g (0.10 M) sodium chloride, NaCl, (Macron Fine Chemicals, Center Valley, PA), 3.48 g (0.30 M) sodium hypophosphite, NaPO₂H₂, Alfa Aesar) and 4.759 g (0.2 M) cobalt chloride, CoCl₂, (Alfa Aesar). The pH of the solution, prior to and after the electrodeposition experiments, was 5.0. The rotating disk electrode (RDE) was rotated at a frequency of 6.67 Hz (400 rpm) with the potential maintained at -1.2 V vs SCE for 15 min. For control experiments, a cobalt-only film was prepared based on the same procedure but in the absence of NaPO₂H₂.

Hydrogen-evolution catalysis measurements were performed in a 0.50 M H₂SO₄ solution that was prepared from 18 M H₂SO₄ (Sigma Aldrich, St. Louis, MO) by use of

ultrapure water. In the HER experiments, the solution and the RDE cell were saturated with 99.999 % H₂(g) (Air Liquide, Plumsteadville, PA) and the RDE was rotated at 26.67 Hz (1600 rpm). Voltammetric data were obtained by cycling the potential between 0.0 V and -0.14 V vs RHE at a scan rate of 1 mV s⁻¹. The *operando* stability of the films was evaluated by continuous cyclic voltammetry over a 24 h period. Chronopotentiometry at constant current density of 10 mA cm⁻² was also performed during which the potential of the cobalt phosphide film was monitored over a 24 h period.

Interfacial Characterization

Scanning-electron micrographs were obtained using a Nova NanoSEM 450 microscope (FEI, Hillsboro, OR) with an accelerating voltage of 15 kV and a working distance of 5.0 mm. Low-magnification micrographs (> 10 nm per pixel) were acquired with an Everhart-Thornley detector whereas higher-magnification micrographs were obtained with a through-the-lens detector. Energy-dispersive X-ray spectra (EDS) were collected in the SEM at an accelerating voltage of 15 kV using a silicon drift detector (Oxford Instruments, Abingdon, United Kingdom). Inca software (Oxford Instruments, Abingdon, United Kingdom) was used to interpret the EDS spectra.

XPS data were obtained using an AXIS Ultra DLD instrument (Kratos Analytical, Manchester, UK) at a background pressure of 1×10^{-9} Torr. High-intensity excitation was provided by monochromatic Al K α X-rays, 1486.6 eV in energy and 0.2-eV resolution at full width at half maximum. Photoelectrons were collected at 0° from the surface normal at a retarding (pass) energy of 80 eV for the survey scans, whereas a pass energy of 20 eV was used for the high-resolution scans. The peak energies were calibrated against the binding energy E_B of the adventitious C 1s peak. For quantitative analysis, the XPS peaks

were fitted using CasaXPS software (CASA Ltd, Teignmouth, United Kingdom) to symmetric Voigt line shapes composed of Gaussian (70%) and Lorentzian (30%) functions that employed a Shirley background.²⁷ For both the Co and P peaks, the fitting was constrained to maintain a 2:1 ratio between the areas of the 2p_{3/2} and 2p_{1/2} peaks, with E_B separations of 0.85 eV and 15 eV for P and Co, respectively. The atomic or molar ratio between Co and P was obtained from Equation (4.1):

$$\frac{N_{\text{Co}}}{N_{\text{P}}} = \frac{A_{\text{Co}}/S_{\text{Co}}}{A_{\text{P}}/S_{\text{P}}} \quad (4.1)$$

where N is the number of atoms, A is the total area of the photoemission peaks, and S the sensitivity factor. Values for S (0.486 for P and 3.59 for Co) were provided by the instrument manufacturer.

Raman spectra of the films were obtained with a Renishaw inVia Raman microprobe (Renishaw, Wotton Under Edge, United Kingdom) equipped with a Leica DM 2500M microscope (Leica Microsystems, Buffalo Grove, IL), a Leica N Plan 50x objective (numerical aperture = 0.75), a 1800 lines mm⁻¹ grating and a CCD detector configured in a 180° backscatter geometry. A 532-nm diode-pumped solid-state laser (Renishaw RL532C50) was used as the excitation and a 20-μW radiant flux was incident onto the surface of the sample.

4.6 References

- (1) Lewis, N. S.; Nocera, D. G. Powering the Planet: Chemical Challenges in Solar Energy Utilization. *Proc. Natl. Acad. Sci. U. S. A.* **2006**, *103*, 15729-15735.
- (2) Lewis, N. S. Toward Cost-Effective Solar Energy Use. *Science* **2007**, *315*, 798-801.
- (3) Turner, J.; Sverdrup, G.; Mann, M. K.; Maness, P.-C.; Kroposki, B.; Ghirardi, M.; Evans, R. J.; Blake, D. Renewable Hydrogen Production. *Int. J. Energ. Res.* **2008**, *32*, 379-407.
- (4) Walter, M. G.; Warren, E. L.; McKone, J. R.; Boettcher, S. W.; Mi, Q.; Santori, E. A.; Lewis, N. S. Solar Water Splitting Cells. *Chem. Rev. (Washington, DC, U. S.)* **2010**, *110*, 6446-6473.
- (5) Gray, H. B. Powering the Planet with Solar Fuel. *Nature Chem.* **2009**, *1*, 7-7.
- (6) Merki, D.; Hu, X. Recent Developments of Molybdenum and Tungsten Sulfides as Hydrogen Evolution Catalysts. *Energy Environ. Sci.* **2011**, *4*, 3878-3888.
- (7) Laursen, A. B.; Kegnæs, S.; Dahl, S.; Chorkendorff, I. Molybdenum Sulfides—Efficient and Viable Materials for Electro - and Photoelectrocatalytic Hydrogen Evolution. *Energy Environ. Sci.* **2012**, *5*, 5577-5591.
- (8) Vrubel, H.; Hu, X. Growth and Activation of an Amorphous Molybdenum Sulfide Hydrogen Evolving Catalyst. *ACS Catal.* **2013**, 2002-2011.
- (9) Benck, J. D.; Chen, Z.; Kuritzky, L. Y.; Forman, A. J.; Jaramillo, T. F. Amorphous Molybdenum Sulfide Catalysts for Electrochemical Hydrogen Production: Insights into the Origin of Their Catalytic Activity. *ACS Catal.* **2012**, *2*, 1916-1923.

- (10) Kibsgaard, J.; Chen, Z.; Reinecke, B. N.; Jaramillo, T. F. Engineering the Surface Structure of MoS₂ to Preferentially Expose Active Edge Sites For electrocatalysis. *Nat. Mater.* **2012**, *11*, 963-969.
- (11) Bonde, J.; Moses, P. G.; Jaramillo, T. F.; Nørskov, J. K.; Chorkendorff, I. Hydrogen Evolution on Nano-Particulate Transition Metal Sulfides. *Faraday Discuss.* **2009**, *140*, 219-231.
- (12) Kong, D.; Wang, H.; Cha, J. J.; Pasta, M.; Koski, K. J.; Yao, J.; Cui, Y. Synthesis of MoS₂ and MoSe₂ Films with Vertically Aligned Layers. *Nano Lett.* **2013**, *13*, 1341-1347.
- (13) Velazquez, J. M.; Saadi, F. H.; Pieterick, A. P.; Spurgeon, J. M.; Soriaga, M. P.; Brunshwig, B. S.; Lewis, N. S. Synthesis and Hydrogen-Evolution Activity of Tungsten Selenide Thin Films Deposited on Tungsten Foils. *J. Electroanal. Chem.* **2014**, *716*, 45-48.
- (14) Kong, D.; Cha, J. J.; Wang, H.; Lee, H. R.; Cui, Y. First-Row Transition Metal Dichalcogenide Catalysts for Hydrogen Evolution Reaction. *Energy Environ. Sci.* **2013**, *6*, 3553-3558.
- (15) Chen, W. F.; Wang, C. H.; Sasaki, K.; Marinkovic, N.; Xu, W.; Muckerman, J. T.; Zhu, Y.; Adzic, R. R. Highly Active and Durable Nanostructured Molybdenum Carbide Electrocatalysts for Hydrogen Production. *Energy Environ. Sci.* **2013**, *6*, 943-951.
- (16) Liu, Q.; Tian, J.; Cui, W.; Jiang, P.; Cheng, N.; Asiri, A. M.; Sun, X. Carbon Nanotubes Decorated with CoP Nanocrystals: A Highly Active Non-Noble-Metal Nanohybrid Electrocatalyst for Hydrogen Evolution. *Angew. Chem.* **2014**

- (17) Tian, J.; Liu, Q.; Asiri, A. M.; Sun, X. Self-Supported Nanoporous Cobalt Phosphide Nanowire Arrays: An Efficient 3D Hydrogen-Evolving Cathode over the Wide Range of pH 0–14. *J. Am. Chem. Soc.* **2014**, *136*, 7587-7590.
- (18) Wang, X.; Xiao, P.; Thia, L.; Alam Sk, M.; Lim, R. J.; Ge, X.; Wang, J.-Y.; Lim, K. H. Molybdenum Phosphide as an Efficient Electrocatalyst for Hydrogen Evolution Reaction. *Energy Environ. Sci.* **2014**.
- (19) Feng, L.; Vrubel, H.; Bensimon, M.; Hu, X. Easily-Prepared Dinickel Phosphide (Ni_2P) Nanoparticles as an Efficient and Robust Electrocatalyst for Hydrogen Evolution. *Phys. Chem. Chem. Phys.* **2014**, *16*, 5917-5921.
- (20) Popczun, E. J.; McKone, J. R.; Read, C. G.; Biacchi, A. J.; Wiltrout, A. M.; Lewis, N. S.; Schaak, R. E. Nanostructured Nickel Phosphide as an Electrocatalyst for the Hydrogen Evolution Reaction. *J. Am. Chem. Soc.* **2013**, *135*, 9267-9270.
- (21) Popczun, E. J.; Read, C. G.; Roske, C. W.; Lewis, N. S.; Schaak, R. E. Highly Active Electrocatalysis of the Hydrogen Evolution Reaction by Cobalt Phosphide Nanoparticles. *Angewandte Chemie International Edition* **2014**, *53*, 5427-5430.
- (22) Burchardt, T. The Hydrogen Evolution Reaction on NiP_x Alloys. *Int. J. Hydrogen Energy* **2000**, *25*, 627-634.
- (23) Burchardt, T.; Hansen, V.; Våland, T. Microstructure and Catalytic Activity Towards the Hydrogen Evolution Reaction of Electrodeposited NiP_x Alloys. *Electrochim. Acta* **2001**, *46*, 2761-2766.
- (24) Paseka, I. Evolution of Hydrogen and Its Sorption on Remarkable Active Amorphous Smooth Ni-P(X) Electrodes. *Electrochim. Acta* **1995**, *40*, 1633-1640.

- (25) Paseka, I.; Velicka, J. Hydrogen Evolution and Hydrogen Sorption on Amorphous Smooth Me-P(X) (Me=Ni, Co and Fe-Ni) Electrodes. *Electrochim. Acta* **1997**, *42*, 237-242.
- (26) Morikawa, T.; Nakade, T.; Yokoi, M.; Fukumoto, Y.; Iwakura, C. Electrodeposition of Ni-P Alloys from Ni-Citrate Bath. *Electrochim. Acta* **1997**, *42*, 115-118.
- (27) Shirley, D. A. High-Resolution X-ray Photoemission Spectrum of the Valence Bands of Gold. *Phys. Rev. B* **1972**, *5*, 4709-4714.
- (28) Biesinger, M. C.; Payne, B. P.; Grosvenor, A. P.; Lau, L. W. M.; Gerson, A. R.; Smart, R. S. C. Resolving Surface Chemical States in XPS Analysis of First Row Transition Metals, Oxides and Hydroxides: Cr, Mn, Fe, Co and Ni. *Appl. Surf. Sci.* **2011**, *257*, 2717-2730.
- (29) McIntyre, N. S.; Cook, M. G. X-Ray Photoelectron Studies on Some Oxides and Hydroxides of Cobalt, Nickel, and Copper. *Anal. Chem.* **1975**, *47*, 2208-2213.
- (30) McIntyre, N. S.; Johnston, D. D.; Coatsworth, L. L.; Davidson, R. D.; Brown, J. R. X-ray Photoelectron Spectroscopic Studies of Thin Film Oxides of Cobalt and Molybdenum. *Surf. Interface Anal.* **1990**, *15*, 265-272.
- (31) Tan, B. J.; Klabunde, K. J.; Sherwood, P. M. A. XPS Studies of Solvated Metal Atom Dispersed (SMAD) Catalysts. Evidence for Layered Cobalt-Manganese Particles on Alumina and Silica. *J. Am. Chem. Soc.* **1991**, *113*, 855-861.
- (32) Nemoshalenko, V. V.; Didyk, V. V.; Senekevich, A. I. *Russ. J. Org. Chem.* **1983**, *28*, 2182.
- (33) Cobo, S.; Heidkamp, J.; Jacques, P.-A.; Fize, J.; Fourmond, V.; Guetaz, L.; Joussetme, B.; Ivanova, V.; Dau, H.; Palacin, S.; Fontecave, M.; Artero, V. A Janus

Cobalt-Based Catalytic Material for Electro-Splitting of Water. *Nat. Mater.* **2012**, *11*, 802-807.

(34) Okamoto, Y.; Nitta, Y.; Imanaka, T.; Teranishi, S. Surface Characterisation of Nickel Boride and Nickel Phosphide Catalysts by X-ray Photoelectron Spectroscopy. *Journal of the Chemical Society, Faraday Transactions 1: Physical Chemistry in Condensed Phases* **1979**, *75*, 2027-2039.

(35) Tyczkowski, J.; Kapica, R.; Łojewska, J. Thin Cobalt Oxide Films for Catalysis Deposited by Plasma-Enhanced Metal–Organic Chemical Vapor Deposition. *Thin Solid Films* **2007**, *515*, 6590-6595.

(36) Hadjiev, V. G.; Iliev, M. N.; Vergilov, I. V. The Raman Spectra of Co_3O_4 . *J. Phys. C* **1988**, *21*, L199.

(37) Frost, R. L. An Infrared and Raman Spectroscopic Study of Natural Zinc Phosphates. *Spectrochimica Acta Part A: Molecular and Biomolecular Spectroscopy* **2004**, *60*, 1439-1445.

(38) Mitchell, P. C. H.; Parker, S. F.; Simkiss, J.; Simmons, J.; Taylor, M. G. Hydrated Sites in Biogenic Amorphous Calcium Phosphates: An Infrared, Raman, and Inelastic Neutron Scattering Study. *J. Inorg. Biochem.* **1996**, *62*, 183-197.

(39) Grosvenor, A. P.; Wik, S. D.; Cavell, R. G.; Mar, A. Examination of the Bonding in Binary Transition-Metal Monophosphides MP (M = Cr, Mn, Fe, Co) by X-ray Photoelectron Spectroscopy. *Inorg. Chem.* **2005**, *44*, 8988-8998.

(40) Plambeck, J. A.; Bard, A. J.; Henning, L. Encyclopedia of Electrochemistry of the Elements. Vol. 3 Vol. 3, 1973.

(41) Carim, A. I.; Saadi, F. H.; Soriaga, M. P.; Lewis, N. S. Electrocatalysis of the Hydrogen-Evolution Reaction by Electrodeposited Amorphous Cobalt Selenide Films. *J. Mater. Chem. A* **2014**, *2*, 13835-13839.

(42) Saadi, F. H.; Carim, A. I.; Velazquez, J. M.; Baricuatro, J. H.; McCrory, C. C. L.; Soriaga, M. P.; Lewis, N. S. Operando Synthesis of Macroporous Molybdenum Diselenide Films for Electrocatalysis of the Hydrogen-Evolution Reaction. *ACS Catal.* **2014**, 2866-2873.

Chapter 5

***Operando* Spectroscopic Analysis of CoP Films**

Electrocatalyzing the Hydrogen-Evolution Reaction

5.1 Introduction and Motivation

In the previous chapter, electrodeposited CoP films were demonstrated to effect the HER at a current density of -10 mA cm^{-2} with $-\eta < 100 \text{ mV}$.¹ So far, however, characterization of this material, as well as related metal phosphides, has relied principally upon *ex-situ* techniques (analysis typically in vacuum or laboratory ambient). In this chapter, electrodeposited CoP films have been interrogated under *in-situ* and *operando* conditions using Raman spectroscopy and Co and P K-edge X-ray absorption spectroscopy (XAS).

5.2 Characterization of CoP films

5.2.1 Potentiostatic and ex-situ characterization of CoP films

CoP films were electrodeposited potentiostatically on planar Cu substrates, from an aqueous solution that contained CoCl_2 and NaPO_2H_2 . Voltammetric, *in-situ*, and *operando* spectroscopic analyses were then performed in $0.500 \text{ M H}_2\text{SO}_4(\text{aq})$ (experimental methods are described in detail in Section 5.4). The steady-state voltammetric response indicated that production of cathodic current densities of 0.5 and

10 mA cm⁻² required overpotentials of -34 and -92 mV (applied biases of -0.300 V and -0.358 V vs. a saturated calomel electrode [SCE]), respectively (Figure 5.1).

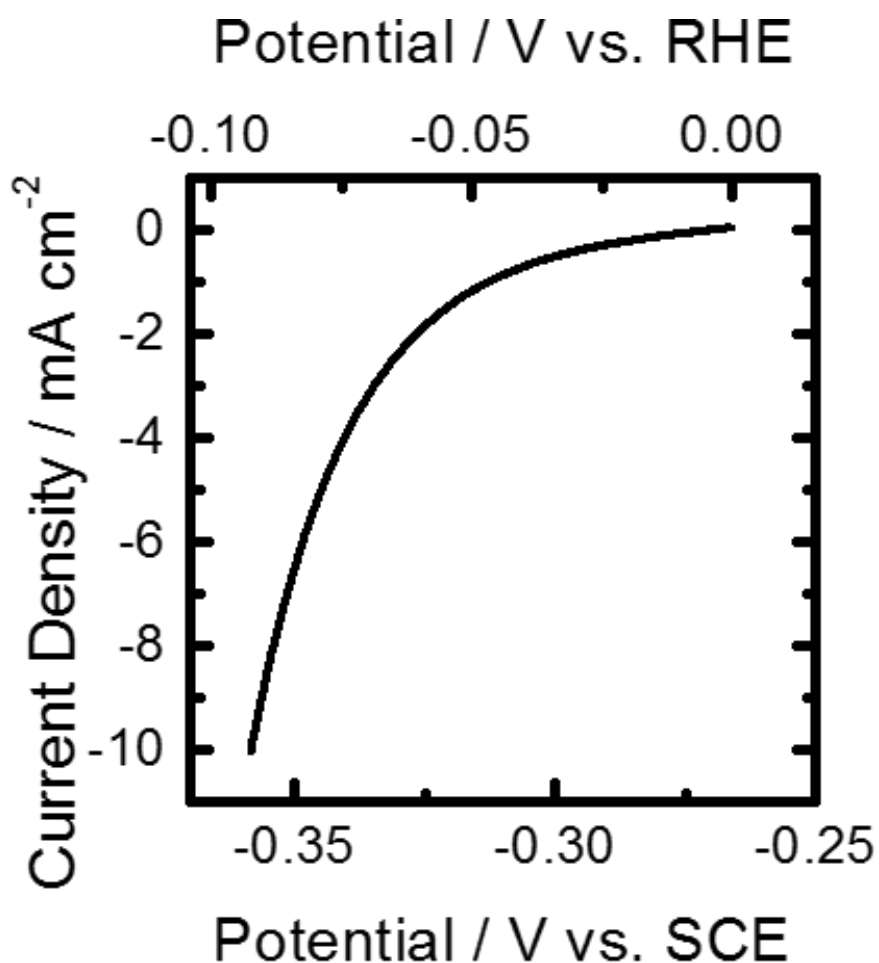


Figure 5.1: Cathodic polarization behavior of a CoP film in 0.500 M H₂SO₄(aq).

Figure 5.2a presents an *ex-situ* Raman spectrum collected from an as-deposited CoP film. A broad band centered at 595 cm⁻¹ is indicative of amorphous cobalt oxide as it has been assigned in literature.² This band also exhibited shoulders at 477, 521, and 677 cm⁻¹, which correspond to Co₃O₄ phonon modes.³ Several Raman modes were observed

in the 970-1200 cm^{-1} spectral region, and are consistent with P-O stretching vibrations in a disordered system.^{4,5} The presence of oxidized Co and P species in the as-prepared film is consistent with prior X-ray photoelectron spectroscopic (XPS) analysis performed in Chapter 4.

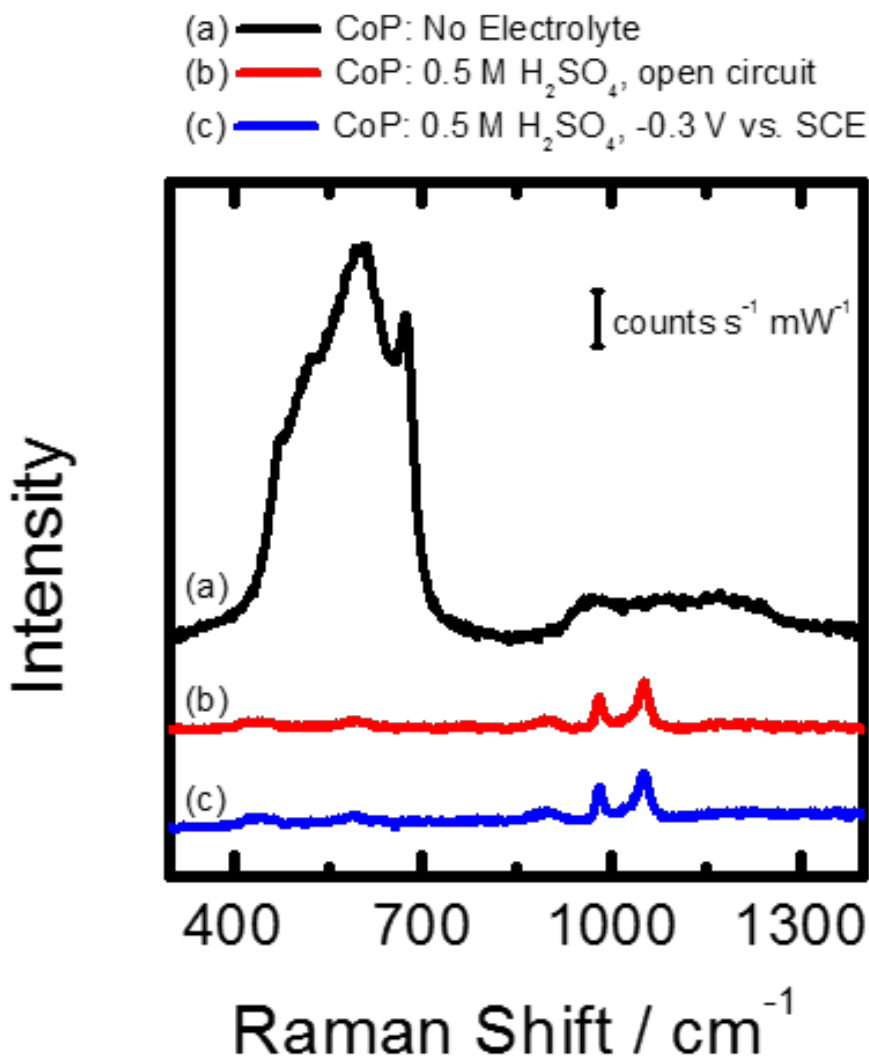


Figure 5.2: Raman spectra of CoP films acquired under the indicated conditions. (a) Ex-situ spectrum of a CoP film prior to contact with $\text{H}_2\text{SO}_4(\text{aq})$ (air ambient, ex-situ). (b) CoP film in 0.500 M H_2SO_4 (aq) at open circuit (in-situ). (c) Same as (b) but at an applied potential of -0.300 V vs. SCE (operando).

The same as-deposited CoP film was then immersed in 0.5 M H₂SO₄ (aq) and an *in-situ* Raman spectrum (open circuit condition) was collected while no externally applied bias was applied (Figure 5.2b). The observed Raman modes centered at 429, 587, 896, 980, 1054 cm⁻¹ are consistent with scattering from the aqueous H₂SO₄ electrolyte.^{6,7} No other signals were observed, including those that correlate in the *ex-situ* Raman spectrum with oxidized Co and P species. After collection of the *in-situ* spectrum, a potential of -0.300 V vs. SCE was applied to the film such that the HER was being actively catalyzed and an *operando* Raman spectrum was acquired (Figure 5.2c). The *operando* spectrum was identical to the *in-situ* spectrum. Before and after collection of the both the *in-situ* and *operando* spectra, significant reflected excitation intensity was observed in a well-defined few- μ m spot, consistent with the high numerical aperture of the objective in the Raman microprobe, indicating that the electrode interface was being interrogated during these analyses. The lack of observed phonon scattering in the *in-situ* and *operando* spectra is consistent with the amorphous nature of electrodeposited CoP materials and with the Pourbaix instability of oxidized cobalt species in strongly acidic media.^{1,8}

To more clearly identify the elemental oxidation states in the active electrocatalyst, Co K-edge and P K-edge XAS were performed in a manner analogous to the Raman investigation. Figure 5.3a-c presents representative *ex-situ*, *in-situ*, and *operando* Co K-edge XAS of electrodeposited CoP films collected in manner similar to the Raman spectra in Figure 5.2a-c. Figure 5.3d-e presents Co K-edge XAS of Co metal and CoO standard materials. The *ex-situ*, *in-situ*, and *operando* CoP spectra all share a

pre-edge feature near 7711 eV that is similar to, but less intense than, that in the Co metal standard. This feature is attributed to metal-to-ligand charge transfer, and resembles the pre-edge feature observed for Ni K-edge XAS of Ni_2P .^{9,10}

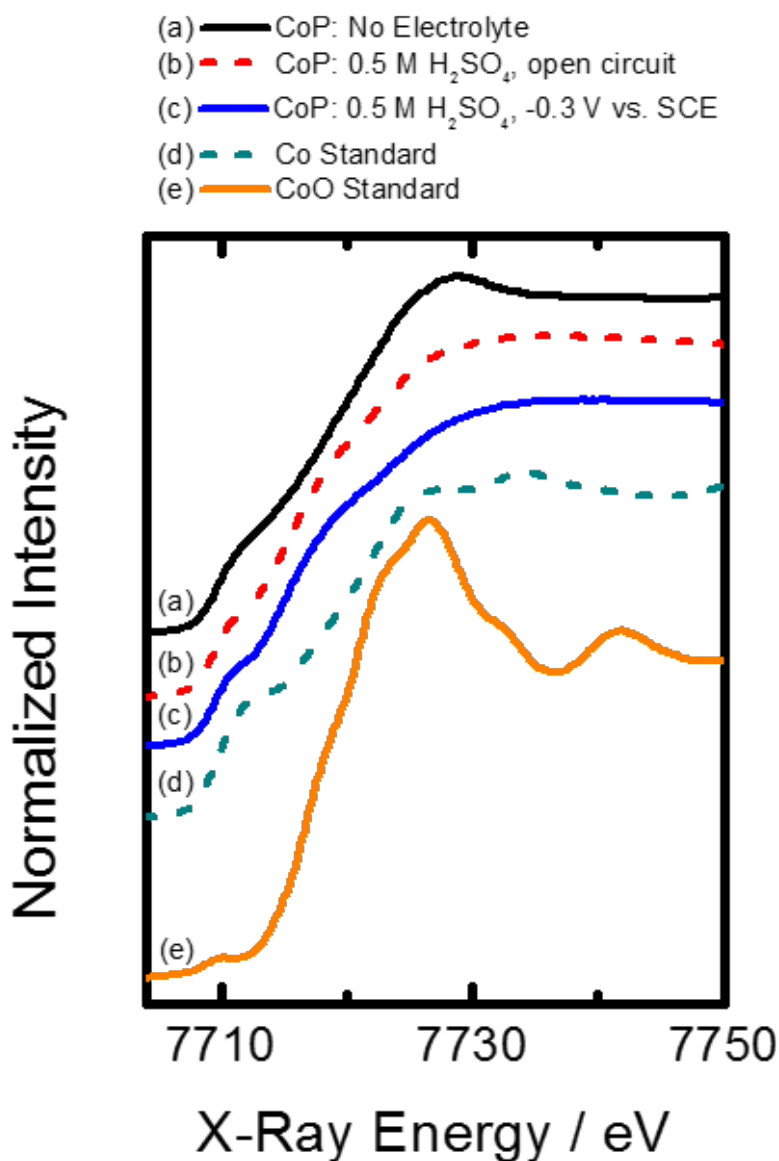


Figure 5.3: Co K-edge X-ray absorbance spectra of both CoP films under the indicated conditions and related spectral standards. (a) Ex-situ spectrum of a CoP film prior to contact with $\text{H}_2\text{SO}_4(\text{aq})$ (air ambient, ex-situ). (b) CoP film in 0.500 M $\text{H}_2\text{SO}_4(\text{aq})$ at

open circuit (in-situ). (c) Same as (b) but at an applied potential of -0.300 V vs. SCE (operando). (d) Co standard. (e) CoO standard.

The *ex-situ* spectrum also exhibited a white line feature at 7727 eV similar to that observed for the CoO standard material, indicating the presence of oxidized Co in the as-prepared material that was not present in the active electrocatalyst. After operation and upon exposure to air, the spectrum of the catalyst changed dramatically and was nearly identical to that of aqueous Co^{2+} , indicating the formation of an oxidized hydrate (Figure 5.4). The CoP is therefore stable only under *in-situ* conditions.

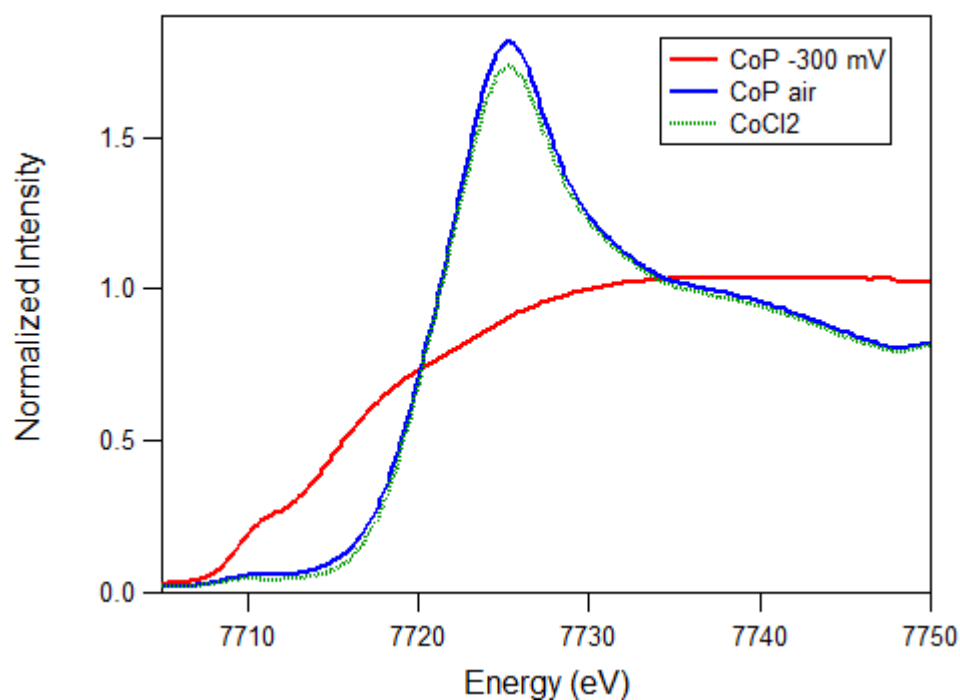


Figure 5.4: Co K-edge XAS of CoP films under the following conditions: (a) spectrum of a CoP film in 0.500 M $\text{H}_2\text{SO}_4(\text{aq})$ at an applied potential of -0.300 V vs. SCE (*operando*).

(b) spectrum of a CoP film exposed to air after *operando* conditions. (c) Reference spectrum of aqueous CoCl_2 .

Fourier-transformed Co K-edge EXAFS, presented in Figure 5.5 showed a first-shell distance of $\sim 2.30 \text{ \AA}$ for the *in-situ* and *operando* catalyst, consistent with reported Co-P distances for amorphous Co-P alloys¹¹ and crystalline Co_2P .¹² These are longer than the typical Co-O distance of $\sim 2.15 \text{ \AA}$ (as shown in the CoO standard), implying direct Co-P interactions in the first shell. There was little indication of long range order, consistent with an amorphous catalyst structure as observed by Raman spectroscopy and previously reported results for electrodeposited CoP. The *ex-situ* catalyst displayed a slightly different EXAFS pattern, consistent with a CoP structure mixed with some metallic and oxidized Co as seen by comparison to Co foil and Co oxide standards. After operation and exposure to air, first shell distances were $\sim 0.29 \text{ \AA}$ shorter, showing a closer match to the CoO standard and consistent with oxidation of Co to form a hydrate.

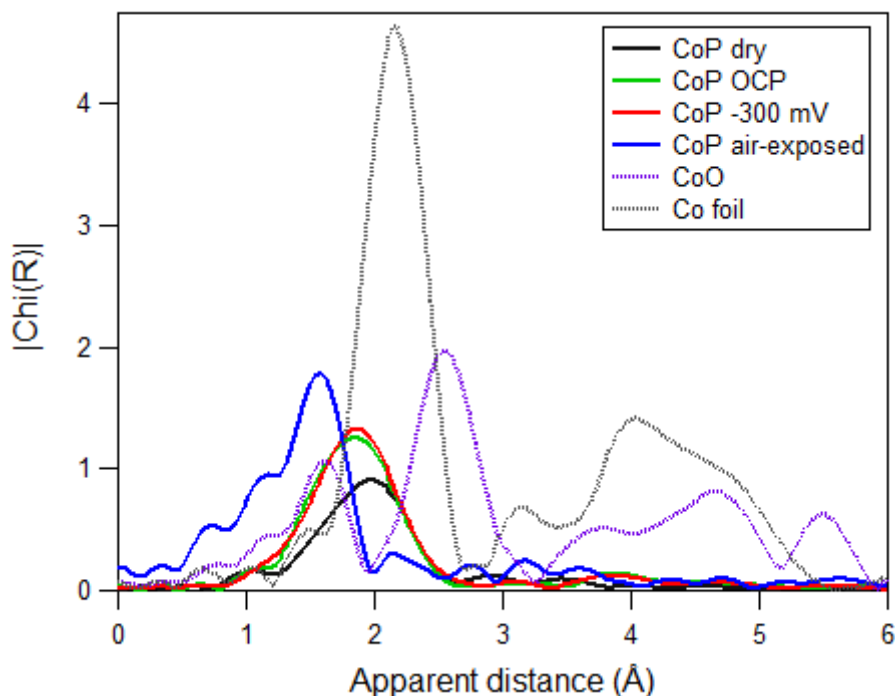


Figure 5.5: Fourier-transformed Co K-edge EXAFS of CoP films under the indicated conditions compared to CoO and Co foil standards, plotted as apparent distance (typically ~ 0.5 Å shorter than the real distance). (a) Ex-situ spectrum of a CoP film prior to contact with H_2SO_4 electrolyte (air ambient, ex-situ). (b) CoP film in 0.500 M $\text{H}_2\text{SO}_4(\text{aq})$ at open circuit (in-situ). (c) Same as (b) but at an applied potential of -0.300 V vs. SCE (operando). (d) CoP film after operation and exposure to air. (e) CoO standard. (f) Co foil standard.

Figure 5.6a-c presents P K-edge XAS directly analogous to the Co K-Edge XAS presented in Figure 5.3a-c. P K-edge XAS of K_3PO_4 , NaPO_2H_2 , and GaP standard materials are also shown in Figure 5.6d-f. The *ex-situ* CoP spectrum exhibited three major features which were centered at 2144.9, 2150.2, and 2152.6 eV. The feature at

2144.9 is a close match to that of the GaP standard, and indicates the presence of CoP. The feature at 2152.6 is a close match to the K_3PO_4 standard, and indicates the presence of a phosphate species in the catalyst. The feature at 2150.2 eV should therefore reflect a phosphorous species in oxidation state intermediate between phosphide and phosphate. This feature is close, but not an exact match, to that observed in the $NaPO_2H_2$ standard. Unfortunately, this standard was unstable under the X-ray beam, decomposing into a phosphate species with a characteristic spectral feature near 2152.2 eV, and a phosphide with a characteristic spectral feature near 2144.9 eV (see SI for details). This instability makes it difficult to determine the exact position of the $NaPO_2H_2$ spectral feature, but it appears to be at ~ 2149.4 eV.

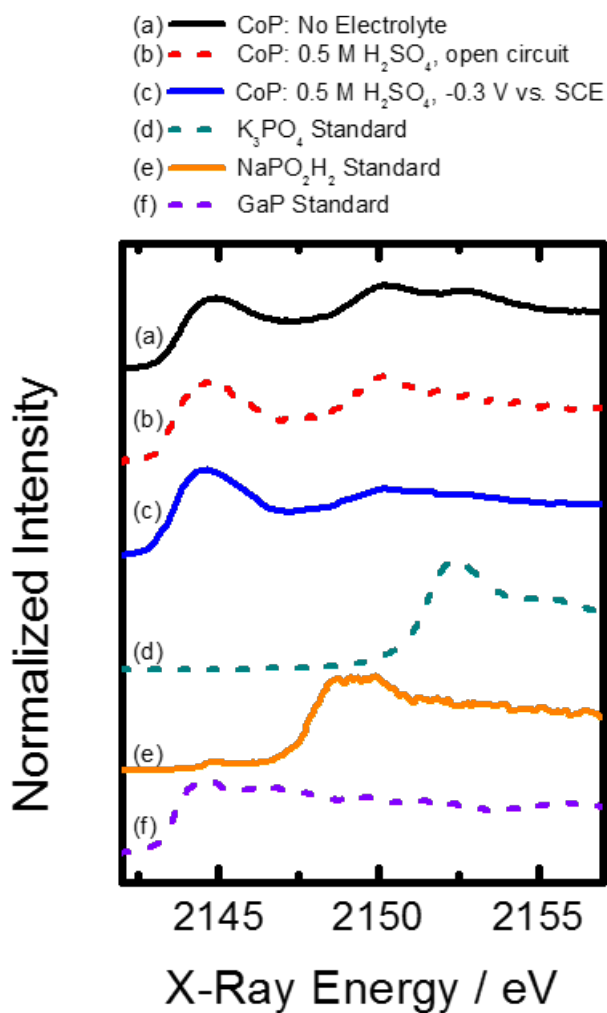


Figure 5.6: P K-edge X-ray absorbance spectra of both CoP films under the indicated conditions and related spectral standards. (a) Ex-situ spectrum of a CoP film prior to contact with H_2SO_4 electrolyte (air ambient, ex-situ). (b) CoP film in 0.500 M $\text{H}_2\text{SO}_4(\text{aq})$ at open circuit (in-situ). (c) Same as (b) but at an applied potential of -0.300 V vs. SCE (operando). (d) K_3PO_4 standard. (e) NaPO_2H_2 standard. (f) GaP standard.

The as-prepared material is therefore composed of P in multiple oxidized and reduced states. Relative to the *ex-situ* spectrum, the spectral features at 2152.6 eV and

2150.2 were attenuated in the *in-situ* and *operando* spectra, but not completely absent, while the feature at 2144.9 (attributed to phosphide) increased in intensity. This behavior is consistent with the Raman analysis, wherein evidence for presence of detectable oxidized P species was only observed in the *ex-situ* examination of the as-prepared material. The cumulative data thus suggest that while *ex-situ* analysis of the electrodeposited film indicates a material composed of multiple phases with Co and P both existing in several oxidation states, the active electrocatalyst is an amorphous material composed of Co in a near-zero valent state and P in a reduced state.

5.3 Conclusion

In summary, CoP films were electrodeposited from an aqueous solution containing CoCl_2 and NaPO_2H_2 . Voltammetric analysis indicated that these films were highly-active catalysts, capable of effecting a -10 mA cm^{-2} current density towards the HER at $-\eta < 100 \text{ mV}$. *Ex-situ* Raman analysis of as-deposited material indicated the presence of several oxidized Co species, including crystalline Co_3O_4 , as well as oxygenated P species but the associated spectroscopic signatures were not observed during *operando* analysis. No phonon scattering was observed during *operando* Raman analysis. Corresponding *ex-situ* Co K-edge and P K-edge XAS also indicated the presence of oxidized Co and P species in addition to a near-zero valent Co species and a reduced P species. The analogous *operando* XAS exhibited disappearance of the absorption edges of oxidized Co and P species. The collective spectroscopic evidence thus indicates that the active electrocatalyst is an amorphous material consisting of Co in a near-zero valent state and P in a reduced state.

5.4 Experimental

Materials and Chemicals All materials and chemicals were used as received from the indicated suppliers without additional purification. H₂O with a resistivity ≥ 18.2 M Ω ·cm (Barnstead Nanopure System) was used throughout.

General Electrochemical Details All electrochemistry was performed using a Bio-Logic SP-200 potentiostat and a cell in three-electrode configuration. A saturated calomel electrode (SCE; CH Instruments) was used as the reference electrode. CoP films were electrodeposited on several Cu substrates for the various analytical methods utilized (described below). Films were deposited from an aqueous solution (pH = 5) of 0.20 M CoCl₂·6H₂O (99.998%, Alfa Aesar), 0.30 M NaPO₂H₂·H₂O (97+%, Alfa Aesar), 0.15 M H₃BO₃ (99.99%, Alfa Aesar), and 0.10 M NaCl (99.0+%, Macron Fine Chemicals). Deposition was effected by biasing the Cu electrode potentiostatically at -1.200 V vs. SCE for 0.50 min at room temperature. All analysis was performed in an aqueous solution of 0.500 M H₂SO₄ (A.C.S. Reagent, J. T. Baker). The uncompensated cell resistance (R_u) was determined from a single-point electrochemical impedance measurement obtained by applying a sine-wave modulated potential with an amplitude of 20 mV at a modulation frequency of 100 kHz centered at the open-circuit potential of the cell. Applied potentials during catalyst analysis were dynamically corrected for an uncompensated resistance of 85% of the value of R_u .

Voltammetric Analysis A single compartment cell and a graphite rod counter electrode (99%, Sigma-Aldrich) were utilized for deposition and analysis. Copper disks with a 5 mm diameter and 4 mm thickness (99.999%, Alfa Aesar) were mounted in PTFE

rotating disk electrode tips (Pine Research Instrumentation) and utilized as catalyst substrates for voltammetric experiments. The tips were mounted on a rotator with the tips suspended such that the Cu surface was immersed in deposition solution. After deposition of a CoP film, all electrodes were removed from the cell, and then the electrodes and the cell were rinsed with H₂O. The cell was then refilled with 0.500 M H₂SO₄ electrolyte and the electrodes replaced. Voltammetric data were then obtained by cycling the potential between -0.266 V and -0.406 V vs. SCE at a scan rate of 1 mV s⁻¹.

Raman Spectroscopy Raman spectra were collected with a Renishaw inVia Raman microprobe equipped with a Leica DM 2500 M microscope, a Leica N Plan L 50x objective (numerical aperture = 0.50), a 1800 lines mm⁻¹ grating, and a CCD detector configured in a 180° backscatter geometry. A 532 nm diode-pumped solid-state (DPSS) laser (Renishaw RL532C50) was used as the excitation source and a 1.58 mW radiant flux was incident on the surface of the sample. A $\lambda/4$ plate was used to circularly polarize the incident excitation. No polarizing collection optics were used. ~ 1 cm square Cu foil (99.9999%, Alfa Aesar) sections were utilized as catalyst substrates for Raman experiments. Single-compartment O-ring compression cells that confined the contact area between the electrolyte and the Cu foil to a circular area of 0.1 cm², and graphite rod counter electrodes, were used for deposition and analysis. After deposition of a CoP film, the Cu foil section was removed from the deposition cell, rinsed with H₂O and dried under a stream of N₂(g). *Ex-situ* Raman spectra were then acquired. The CoP-decorated Cu foil was then placed in the analysis cell with 0.500 M H₂SO₄. The O-ring seal was located on the bottom wall of the analysis cell. The cell was equipped with a glass window on the top face that enabled *in-situ* and *operando* collection of Raman signal.

Raman spectra were acquired *in-situ* after solution was added to the cell. The CoP film was then conditioned by cycling the potential 10 times between -0.266 V and -0.406 V vs. SCE at a scan rate of 15 mV s⁻¹. Raman spectra were then obtained under *operando* conditions by acquiring spectra while the electrode was under potential control.

X-ray Absorption Spectroscopy Co K-edge X-ray absorption spectra (XAS) were performed at Beamline 7-3 at the Stanford Synchrotron Radiation Lightsource (SSRL) at SLAC National Accelerator Laboratory. Monochromatic incoming radiation was obtained using a Si(220) double crystal that had been detuned to 50% of the flux maximum at the K-edge, to attenuate higher harmonics. The incident beam intensity was monitored by a N₂-filled ionization chamber that was positioned between the source and the sample. Fluorescence signal was collected at 90 degrees from the source propagation vector using a 30-element Ge detector (Canberra Industries). P K-edge XAS measurements were performed at Beamline 14-3 at the SSRL. Monochromatic X-rays were produced using a Si(111) double crystal. The incident radiation intensity was monitored via a He-filled ionization chamber that was positioned between the source and the sample. Fluorescence signal was collected at 90 degrees from the source propagation vector using a Vortex 4-element silicon drift detector (Hitachi High-Technologies Science).

Ex-situ Co K-Edge XAS of Co and CoO (99.998%, Alfa Aesar) and P K-Edge XAS of K₃PO₄·7H₂O (98%, VWR), NaPO₂H₂·H₂O (99%, Sigma Aldrich) and GaP were acquired as standards. Powder standards (all except for Co and GaP) were diluted with BN to minimize overabsorption effects. P K-edge XAS were acquired under a He ambient to prevent atmospheric X-ray attenuation.

3 mm square, 0.5 μm thick Si_3N_4 membranes, enclosed by a 10 mm square Si frame, were utilized as X-ray transparent substrates. Electron-beam evaporation was used to deposit a 2 nm thick Ti adhesion layer and a 100 nm Cu film on one side of the framed Si_3N_4 membranes. A deposition rate of 2 \AA s^{-1} , with the base pressure 5×10^{-6} Torr and a substrate temperature of $100 \text{ }^\circ\text{C}$ were utilized. A two compartment H-cell was utilized for deposition and analysis, as described elsewhere.^{13, 14} Briefly, a porous glass frit was used to divide the two compartments. An Ir foil (99.7%, Goodfellow) counter electrode was utilized and isolated in one of the two compartments. The reference electrode was placed in the other compartment. The compartment that housed the reference electrode had a square opening. The framed, Cu-coated Si_3N_4 membranes were affixed to the cell in this location by use of epoxy, with the Cu-coated portion of the electrode facing into the cell (Loctite Instant Mix). After deposition of a CoP film, the counter and reference electrodes were removed from the cell, and then the electrodes and the cell were rinsed with H_2O . *Ex-situ* XAS of the CoP films were then acquired. During XAS acquisition, the excitation X-rays were directed at 45 degrees to the exposed Si_3N_4 face. For the P K-edge XAS experiments, the entire cell was enclosed in a He-filled bag to prevent atmospheric X-ray attenuation. After collection of the *ex-situ* spectra, the cell was refilled with 0.500 M $\text{H}_2\text{SO}_4(\text{aq})$ and the electrodes were replaced. The CoP film was then conditioned by cycling the potential 10 times between -0.266 V and -0.406 V vs. SCE at a scan rate of 15 mV s^{-1} . XAS were then obtained under *operando* conditions while the electrode was under potentiostatic control.

Spectra were subjected to baseline correction and intensity normalization using the Athena software package based on IFEFFIT.^{15, 16} For the CO K-edge EXAFS, the

background was fit using a five-domain cubic spline and removed, and the resulting oscillations were plotted in k-space and then Fourier-transformed into real space for analysis.

5.5 References

1. F. H. Saadi, A. I. Carim, E. Verlage, J. C. Hemminger, N. S. Lewis and M. P. Soriaga, *J. Phys. Chem. C*, 2014, **118**, 29294-29300.
2. J. Tyczkowski, R. Kapica and J. Łojewska, *Thin Solid Films*, 2007, **515**, 6590-6595.
3. V. G. Hadjiev, M. N. Iliev and I. V. Vergilov, *J. Phys. C Solid State Phys.*, 1988, **21**, L199-L201.
4. R. L. Frost, *Spectrochim. Acta Mol. Biomol. Spectrosc.*, 2004, **60**, 1439-1445.
5. P. C. H. Mitchell, S. F. Parker, K. Simkiss, J. Simmons and M. G. Taylor, *J. Inorg. Biochem.*, 1996, **62**, 183-197.
6. R. M. Bell and M. A. Jeppesen, *J. Chem. Phys.*, 1935, **3**, 245.
7. R. A. Cox, Ü. L. Haldna, K. L. Idler and K. Yates, *Can. J. Chem.*, 1981, **59**, 2591-2598.
8. M. Pourbaix, *Atlas of Electrochemical Equilibria In Aqueous Solutions*, Pergamon Press, Oxford, 1966.
9. K. K. Bando, T. Wada, T. Miyamoto, K. Miyazaki, S. Takakusagi, Y. Koike, Y. Inada, M. Nomura, A. Yamaguchi, T. Gott, S. Ted Oyama and K. Asakura, *Journal of Catalysis*, 2012, **286**, 165-171.
10. T. Kawai, S. Sato, W. Chun, K. Asakura, K. Bando, T. Matsui, Y. Yoshimura, T. Kubota, Y. Okamoto and Y. Lee, *Physica Scripta*, 2005, **2005**, 822.
11. G. CARGILL III and R. Cochrane, *Le Journal de Physique Colloques*, 1974, **35**, C4-269-C264-278.

12. S. Rundqvist, *Acta Chem. Scan*, 1960, **14**, 1961-1979.
13. Y. Gorlin, B. Lassalle-Kaiser, J. D. Benck, S. Gul, S. M. Webb, V. K. Yachandra, J. Yano and T. F. Jaramillo, *J. Am. Chem. Soc.*, 2013, **135**, 8525-8534.
14. S. Gul, J. W. Ng, R. Alonso-Mori, J. Kern, D. Sokaras, E. Anzenberg, B. Lassalle-Kaiser, Y. Gorlin, T. C. Weng, P. H. Zwart, J. Z. Zhang, U. Bergmann, V. K. Yachandra, T. F. Jaramillo and J. Yano, *Phys. Chem. Chem. Phys.*, 2015, **17**, 8901-8912.
15. B. Ravel and M. Newville, *Journal of synchrotron radiation*, 2005, **12**, 537-541.
16. M. Newville, *Journal of synchrotron radiation*, 2001, **8**, 322-324.

Chapter 6

Costs of Transporting Electrical and Chemical Energy

6.1 Introduction

The transport of energy is an integral component of the global energy economy. Primary and secondary energy supplies are typically transported for long distances by merchant ships (tankers and cargo vessels), pipelines, or electrical wires. Fossil hydrocarbons are the predominant energy supplies that are used and transported today, however, transport of energy from renewable sources, including hydrogen and redox-flow electrolytes, may become increasingly important in the future.

Oil, natural gas, and coal are the primary sources for 80% of the world's energy.¹ Oil and gas are always moved in part through pipelines, with large fractions transported over long distances by tankers and/or rail. Coal is moved in railcars and by ship.

Pipelines account for a major percentage of both domestic and international energy transport, and are used to supply gases (e.g. natural gas) and liquids (e.g. oil). In 2013, approximately 8.5 billion barrels of crude oil were transported across 160,000 miles of oil pipeline in the United States,^{2,3} and over 744 million cubic feet of natural gas were transported in over 300,000 miles of natural gas pipelines.^{3,4} Tankers are also used to transport oil and, increasingly, to transport liquefied natural gas (LNG). In 2005, over 60% of all petroleum consumed was transported in tankers.⁵ Pipelines are used to

transport fuels over land and tankers over water, so the two methods are often to supplement each other.

Electrical energy is transported from generation to load using conducting transmission wires. Over 4 trillion kilowatthours of electricity is annually generated and transmitted in the United States.⁶ High voltage alternating current (AC) is used for the majority of long distance electricity transmission. High voltage direct current (HVDC) has efficiency advantages and has long been proposed as a potentially economically competitive mode of transmission.⁷ Transmission lines are generally supported by tall above ground supports and occasionally are placed underground, where they are less affected by weather but incur additional costs.⁸

Strong interest in renewable energy has led to several proposed future energy transportation scenarios, including 100% grid electrification⁹ and widespread installation of hydrogen pipelines.^{10,11} When considering future energy infrastructure alternatives, it is important to include their differing energy transportation costs. Herein we summarize and compare the estimated costs for building and transporting different energy sources across new infrastructure. Costs are compared on a dollar per unit power per unit distance basis, and on a dollar per unit of energy per unit distance basis, using expected operating lifetimes.

6.2 Costs of Energy Transport

6.2.1 Oil Pipelines

Oil that is transported over land primarily moves through 24” to 48” diameter pipelines.¹² The project cost of constructing an oil pipeline, as estimated by averaging the construction cost of large numbers of pipelines, is approximately 61 \$/ft³, with an operating lifetime of 40 years.¹² The capital cost breakdown (Figure 6.1) shows, on average, an even split between material and labor costs, irrespective of pipeline diameter and length.¹² It is important to note that these breakdowns are averages and have high variability between projects. The cost of transporting oil in pipelines can therefore be estimated using the energy density of oil, 38.5 GJ/m³.¹³ (Table 6.1). Costs were calculated for fluid velocities ranging from 1- 3 m/s, which correspond to average pipeline velocities. The capital cost was assumed to account for 38%¹⁴ of the total cost of transporting the oil, with the majority of the remaining costs associated with corrosion and pipeline maintenance. This total cost estimate for transporting oil in pipelines is comparable to published values.^{15, 16}

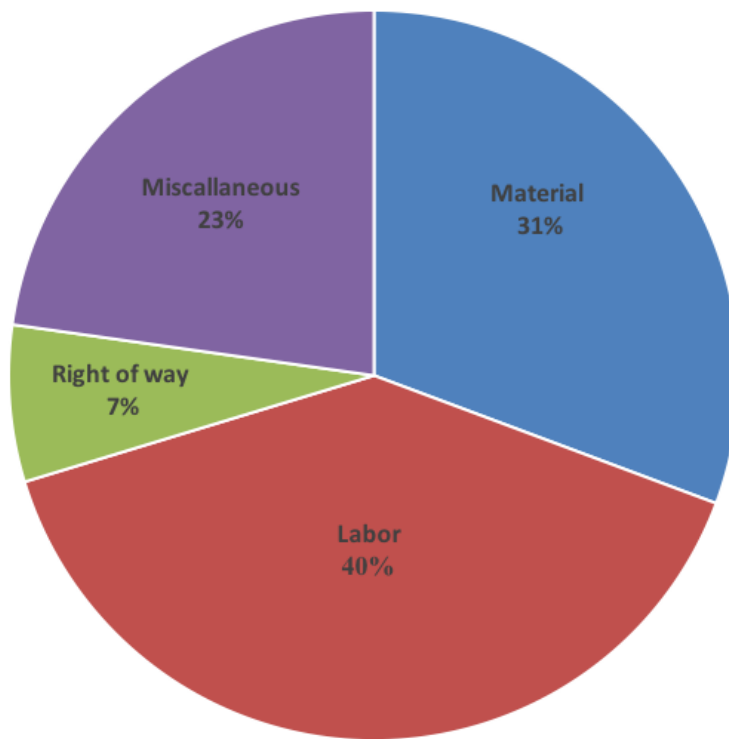


Figure 6.1: Capital cost breakdown for oil pipelines

Pipe Diameter (in)	Cost of pipeline (million \$/mile)	fluid velocity (m/s)	Energy density of oil (GJ/m ³)	Flow rate (m ³ /s)	Energy flow rate (GW)	Cost (\$/km kW)	lifetime (years)	Capital Cost (\$/1000 km-GJ)	Total Cost (\$/1000 km-GJ)
36	2.3	1.00	38.50	0.66	25.28	0.06	40	0.04	0.12
36	2.3	2.00	38.50	1.31	50.56	0.03	40	0.02	0.06
36	2.3	3.00	38.50	1.97	75.83	0.02	40	0.01	0.04

Table 6.1: Cost of transporting oil in pipelines

6.2.2 Natural Gas Pipelines

Most natural gas is transported in pipelines. Long-distance natural gas pipelines are usually maintained at high pressures (~65-90 bar)^{11, 17} with fluid velocities of ~10 m/s.¹⁸ Natural gas is predominately methane, which is reasonably treated as an ideal gas with an energy density of approximately 47 MJ/kg.¹⁹ The costs of construction and use of natural gas pipelines were estimated from three separate reports^{10, 11, 20} (Table 6.2). The capital cost of natural gas pipelines has similar a cost breakdown to that of oil pipelines.²¹ By analogy to oil pipelines, assuming that the capital cost accounts for 38% of the total cost, and assuming a lifetime of 40 years, the total cost per unit distance for transport of gas through pipelines is similar, but higher, than the cost for oil pipelines. These cost estimates are also comparable to previous reports.²²

Pipe diameter (in)	Cost of pipeline (million \$/mile)	Fluid velocity (m/s)	Pressure (bar)	Heat of Combustion (MJ/kg)	Cost (\$/km kW)	Lifetime (years)	Capital Cost (\$/1000 km-GJ)	Total Cost (\$/1000 km-GJ)
20	1.44	10	65	47	0.22	25	0.28	0.75
36	2.91	10	65	47	0.14	25	0.18	0.47
20	1.44	10	90	47	0.16	25	0.21	0.54
36	2.91	10	90	47	0.10	25	0.13	0.34

Table 6.2: Cost of transporting natural gas by pipeline

6.2.3 Hydrogen Pipelines

Hydrogen pipelines are used primarily to transport hydrogen as a chemical feedstock for commercial operations. To estimate of the cost of constructing long-distance hydrogen pipelines for energy purposes, the cost was assumed to be similar to that of commercially installed natural gas pipelines. This is an optimistic assumption as the transportation of hydrogen would likely require more expensive steel due to hydrogen embrittlement.¹⁰ The hydrogen pressure was assumed to be ~10-30 bar²⁰ and the fluid velocity was assumed to be approximately 15 m/s.¹¹ Hydrogen is assumed to behave as an ideal gas with an energy density of 120 MJ/kg.¹⁹ Both the capital and total costs of transporting energy via hydrogen in pipelines are estimated to be an order of magnitude greater than natural gas (Table 6.3), primarily due to the lower heat of combustion per mole as well as the lower pressures utilized in hydrogen pipelines.

Pipe diameter (in)	Cost of pipeline (million \$/mile)	Fluid velocity (m/s)	Pressure (bar)	Heat of Combustion (MJ/kg)	Cost (\$/km kW)	Lifetime (years)	Capital Cost (\$/1000 km-GJ)	Total Cost (\$/1000 km-GJ)
20	1.44	15	15	120	2.02	25	2.57	6.75
36	2.91	15	15	120	1.27	25	1.61	4.24
20	1.44	15	30	120	1.01	25	1.28	3.38
36	2.91	15	30	120	0.63	25	0.80	2.11

Table 6.3: Cost of transporting hydrogen in pipelines

6.2.4 Pipelines for Alternative Chemicals

In addition to transporting oil, large diameter pipelines may also be utilized for transporting chemical energy in the form of redox flow battery electrolytes or liquid organic hydrogen carriers (LOHC). The cost of transporting several redox flow systems and LOHCs can be estimated using their energy densities, which are typically much lower than the energy density of oil.²³⁻²⁷ The costs of these pipelines were calculated by assuming similar diameters, materials, and fluid velocities to oil pipelines. Table 6.4 shows the capital costs of transporting alternative chemicals in pipelines. The cost of transporting redox flow electrolytes is several orders of magnitude greater than for oil, due to the relatively low energy density. LOHCs benefit from significantly higher energy density than redox flow electrolytes, resulting in much lower costs of transportation.

	Pipe Diameter (in)	Cost of pipeline (million \$/mile)	fluid velocity (m/s)	Energy density of electrolyte (GJ/m ³)	Cost (\$/km kW)	Lifetime (years)	Capital Cost (\$/1000 km-GJ)	Total Cost (\$/1000 km-GJ)
Vanadium Flow	36	2.28	1	0.09	23.94	40	18.91	49.77
Vanadium Flow	36	2.28	2	0.09	11.97	40	9.46	24.89
High density Vanadium Flow	36	2.28	1	0.15	14.60	40	11.53	30.35
High density Vanadium Flow	36	2.28	2	0.15	7.30	40	5.77	15.17
Zinc-polyiodide	36	2.28	1	0.6	3.59	40	2.84	7.47
Zinc-polyiodide	36	2.28	2	0.6	1.80	40	1.42	3.73
Zinc-bromide	36	2.28	1	0.25	8.55	40	6.75	17.78
Zinc-bromide	36	2.28	2	0.25	4.28	40	3.38	8.89
Dodecahydro-N-ethylcarbazole/N-ethylcarbazole	36	2.28	1	7.24	0.30	40	0.24	0.63
Dodecahydro-N-ethylcarbazole/N-ethylcarbazole	36	2.28	2	7.24	0.15	40	0.12	0.31
Decalin/naphthalene	36	2.28	1	6.82	0.32	40	0.25	0.67
Decalin/naphthalene	36	2.28	2	6.82	0.16	40	0.13	0.33

Table 6.4: Cost of transporting energy as redox flow battery electrolyte by pipeline

6.2.5 Oil Tankers

Oil is generally transported long distances over water in tankers that vary in carrying capacity from small 45 dry weight ton (DWT) ships to very large crude carriers (VLCC) with capacities of ~160-320 DWT. VLCC's account for the majority of crude oil shipments across the globe.²⁸ The average lifetime of a tanker is estimated to be 25 years,²⁹ the average speed was assumed to be ~10 knots³⁰ and the utilization percentage (fraction of time that the tanker carries cargo) was assumed to be 40%. Table 6.5 summarizes the cost of energy transport as oil in tankers. While tankers vary quite significantly in size and cost, their capital costs are relatively similar and rather small (an order of magnitude less than the capital cost of oil pipelines).³¹ The total cost of oil transportation was estimated by averaging the cost of several tanker route rates,^{15, 32} and

was found to be comparable to that of oil pipeline transportation, implying that the variable costs constitute a very large portion of the total costs. The greater variable costs are likely due to high maintenance and personnel cost.

Name	Cost of tanker (million \$)	capacity (million bbl)	barrel of oil equivalent (GJ/bbl)	average speed (knots)	Cost (\$/km kW)	Lifetime (years)	Capital Cost (\$/1000 km-GJ)	Total Cost (\$/1000 km-GJ)
Panamax	30	0.54	6.1	10	0.004	30	0.006	0.04
Aframax	49	0.69	6.1	10	0.006	30	0.007	0.06
Suezmax	52	1.26	6.1	10	0.003	30	0.004	0.03
VLCC	94	1.96	6.1	10	0.004	30	0.005	0.04

Table 6.5: Cost of transporting oil by tanker

6.2.6 Liquefied Natural Gas Tankers

While tankers typically transport liquid crude oil and its refined products, ships (and trains) capable of carrying liquefied natural gas (LNG) are increasingly used, taking advantage of abundant and relatively low-cost natural gas. Several unique challenges make energy transportation as LNG more expensive than for oil in tankers, including the need for dedicated ports as well as highly trained personnel who are capable of handling the highly flammable liquefied natural gas. The costs were calculated by assuming that LNG tankers, relative to oil tankers, had similar lifetimes, speeds, utilization percentages,

and ratio of capital cost to total cost. Additionally, a 30% loss of LNG was assumed during the liquefaction. The cost of LNG tankers was estimated from published data.^{31, 33} The total cost of energy transport as LNG in ships was found to be nearly equivalent to that of natural gas transmission in pipelines. This estimate is consistent with available data on the cost of LNG tanker transportation.^{22, 34}

Cost of tanker (million \$)	capacity (thousand m ³)	barrel of oil equivalent (GJ/m ³)	average speed (knots)	Cost (\$/km kW)	Lifetime (years)	Capital Cost (\$/1000 km-GJ)	Total Cost (\$/1000 km-GJ)
71	75	22	10	0.004	30	0.03	0.26
179	125	22	10	0.006	30	0.05	0.4

Table 6.6: Transportation costs for liquefied natural gas (LNG) by tanker

6.2.7 Electrical Transmission Lines

High-voltage transmission lines are the backbone of the electrical energy grid, with more than 450,000 miles of domestic high-voltage transmission lines.³⁵ The cost of moving energy as electricity in transmission lines was estimated from reports analyzing the project cost of different types of power lines (Table 6.7).^{7, 8, 36-38} The total cost of energy transmission via electrical wires was found to be approximately an order of magnitude more expensive than the total cost of energy transmission via oil pipelines. The breakdown of capital cost for electrical transmission lines is estimated in Figure 6.2.³⁹ The cost of electricity transmission can be substantially higher if substations are

needed, and right-of-way costs have the potential to further markedly increase the cost of electricity transmission, with some recent transmission lines having full project costs that are as much as a factor of ten higher than the costs in Table 6.7.³⁸

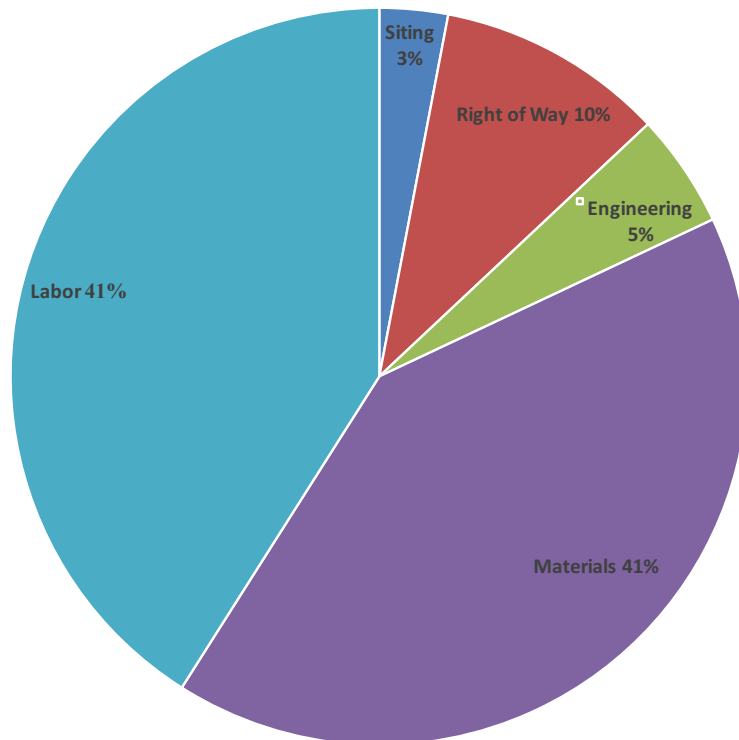


Figure 6.2: Capital cost breakdown for electrical transmission lines

Type	Power (MW)	Current (A)	Cost of transmission line (million \$/mile)	Cost (\$/km kW)	Lifetime (years)	Capital Cost (\$/1000 km-GJ)	Total Cost (\$/1000 km-GJ)
230 kV single	400	1.74	1.44	3.60	40	1.77	3.53
230 kV double	800	3.48	2.30	2.88	40	1.41	2.83
345 kV single	750	2.17	2.02	2.69	40	1.32	2.64
345 kV double	1500	4.35	3.23	2.15	40	1.06	2.11
400 kV double	3190	8	4.65	1.46	40	0.72	1.43
400 kV double	6380	16	8.45	1.32	40	0.65	1.30
400 kV double	6930	17.33	8.45	1.22	40	0.60	1.20
500 kV Single	1500	3	1.92	1.19	40	0.94	1.88
500 kV double	3000	6	1.54	0.95	40	0.75	1.51
500 kV HVDC	3000	6	0.77	0.48	40	0.38	0.75
600 kV HVDC	3000	5	0.81	0.50	40	0.40	0.79

Table 6.7: Estimated cost of transporting electricity

6.3 Overall Comparison, Comment and Conclusion

Figure 6.3 compares the estimated costs of transporting energy resources in different forms. The costs are a combination of many factors, including the end-station costs, maintenance costs and the cost of building and operating the transport system. The cost of transporting energy per unit distance varies by over two orders of magnitude depending on the energy carrier and the method of transportation. Due to their high energy densities, oil and natural gas have an inherent advantage in comparison to alternative transportable fuels such as redox flow battery electrolytes or hydrogen.

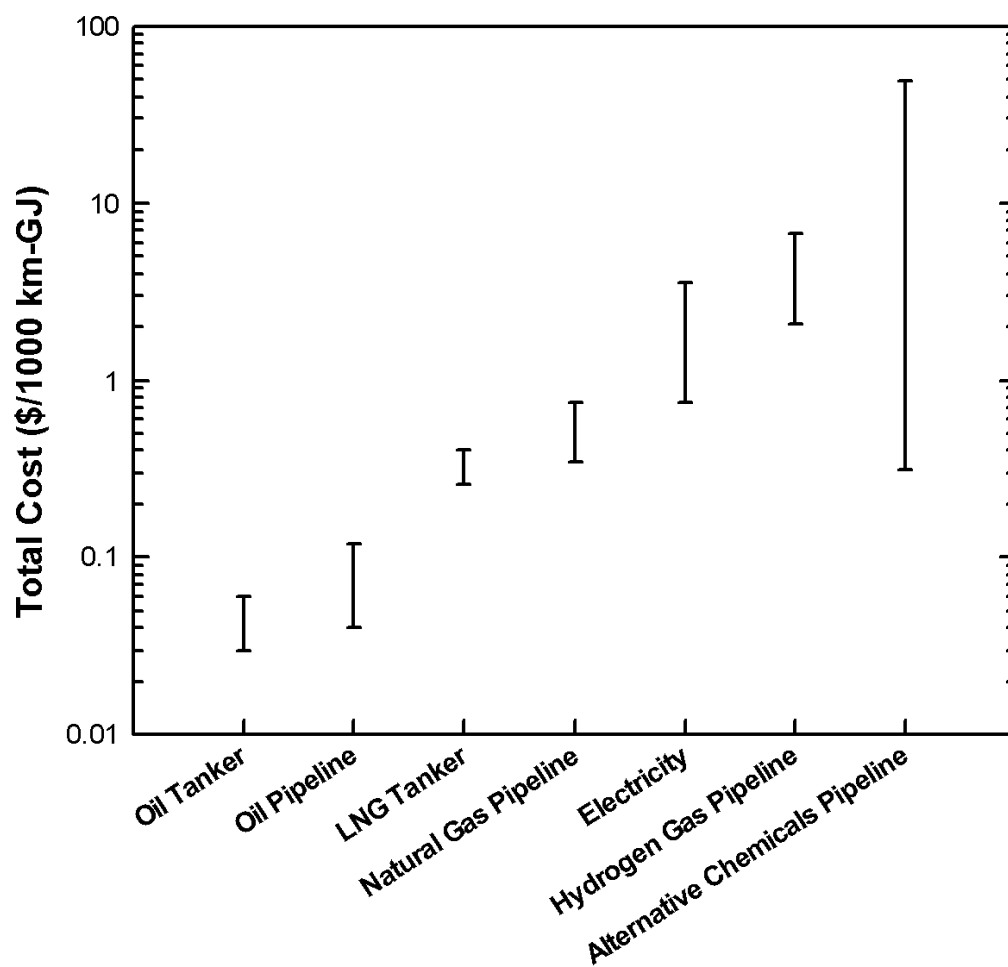


Figure 6.3: Summary of the cost of transportation energy resources in different forms.

6.4 References

1. *Key World Energy Statistics*, International Energy Agency, 2015.
2. U.S. Liquids Pipeline Usage & Mileage Report, Association of Oil Pipelines, 2014.
3. B. o. T. Statistics, *National Transportation Statistics*, U.S. Department of Transportation, 2016.
4. U. S. E. I. Administration, *Natural Gas Annual*, U.S. Department of Energy, 2014.
5. J.-P. Rodrigue, *The Geography of Transport Systems*, New York: Routledge, 2013.
6. U. S. E. I. Administration, *Electric Power Annual*, U.S. Department of Energy, 2016.
7. R. Pletka, J. Khangura, A. Rawlins, E. Waldren and D. Wilson, *Capital Costs for Transmission and Substations*, Black & Veatch, 2014.
8. P. Brinckerhoff, *Electricity Transmission Costing Study*, 2012.
9. M. Z. Jacobson, M. A. Delucchi, G. Bazouin, Z. A. F. Bauer, C. C. Heavey, E. Fisher, S. B. Morris, D. J. Y. Piekutowski, T. A. Vencill and T. W. Yeskoo, *Energy & Environmental Science*, 2015, **8**, 2093-2117.
10. W. Leighty, J. Holloway, R. Merer, B. Somerday, C. S. Marchi, G. Keith and D. White, presented in part at the 16th World Hydrogen Energy Conference, Lyon 2006.

11. S. Baufumé, F. Grüger, T. Grube, D. Krieg, J. Linssen, M. Weber, J.-F. Hake and D. Stolten, *International Journal of Hydrogen Energy*, 2013, **38**, 3813-3829.
12. Z. Rui, P. A. Metz, D. B. Reynolds, G. Chen and X. Zhou, *International Journal of Oil, Gas and Coal Technology*, 2011, **4**, 244-263.
13. R. Toossi, *Energy and the Environment: Resources, Technologies, and Impacts*, Verve Publishers, 2009.
14. D. Webster, presented in part at the National Association of Pipe Coating Applicators, 2010.
15. A. S. Erickson and G. B. Collins, *Naval War College Review*, 2010, **63**, 88-111.
16. A. o. O. Pipelines, <http://www.aopl.org/pipeline-basics/about-pipelines/>, Accessed August, 2016.
17. S. M. Folga, *Natural Gas Pipeline Technology Overview*, Argonne National Laboratory, 2007.
18. P. M. Coelho and C. Pinho, *Journal of the Brazilian Society of Mechanical Sciences and Engineering*, 2007, **29**, 262-273.
19. B. Boundy, S. W. Diegel, L. Wright and S. C. Davis, *Biomass Energy Data Book: Edition 4*, Oak Ridge National Laboratory, 2011.
20. W. A. Amos, *Cost of Storing and Transporting Hydrogen*, National Renewable Energy Laboratory, 1998.
21. S. Natella, R. Deverell, D. Hewitt, S. Revielle, H. Tse, A. Kuske, M. Garvey, J. Edwards, R. Kersely, J. Stuart, M. Rana, A. Jayaram, E. Westlake, K. Iorio and A. Shaw, *The shale revolution*, Credit Suisse, 2012.

22. R. G. Schwimmbeck, presented in part at the 3rd Pipeline Conference, 2008.
23. H. Y. Zhao, S. T. Oyama and E. D. Naeemi, *Catalysis Today*, 2010, **149**, 172-184.
24. M. Amende, C. Gleichweit, K. Werner, S. Schernich, W. Zhao, M. P. A. Lorenz, O. Höfert, C. Papp, M. Koch, P. Wasserscheid, M. Laurin, H.-P. Steinrück and J. Libuda, *ACS Catalysis*, 2014, **4**, 657-665.
25. P. Boer and J. Raadschelders, *Flow Batteries*, Leonardo Energy, 2007.
26. L. Li, S. Kim, W. Wang, M. Vijayakumar, Z. Nie, B. Chen, J. Zhang, G. Xia, J. Hu, G. Graff, J. Liu and Z. Yang, *Advanced Energy Materials*, 2011, **1**, 394-400.
27. B. Li, Z. Nie, M. Vijayakumar, G. Li, J. Liu, V. Sprenkle and W. Wang, *Nat Commun*, 2015, **6**.
28. T. M. Hamilton, Oil tanker sizes range from general purpose to ultra-large crude carriers on AFRA scale
29. The Average Age of Demolished Crude Oil Tankers Hits 21 – Not Much Room Left For Demolition Balancing The Market, Baltic and International Maritime Council, 2012.
30. I. Arnsdorf and A. Nightingale, Bloomberg, 2011.
31. U. secretariat, *Review of Maritime Transport*, United Nations, 2006.
32. M. Jha and N. Christie, in *Bloomberg*, 2015.
33. D. Maxwell and Z. Zhu, *Energy Economics*, 2011, **33**, 217-226.
34. S. Cornot-Gandolphe, IEA (2005): Energy Prices and Taxes, Quarterly Statistics. First Quarter, 2005.
35. Transmission & Distribution Infrastructure, Harris Williams & Co., 2014.

36. K. Inc, Life-Cycle 2012: Connecticut Siting Council Investigation into the Life-cycle Costs of Electric Transmission Lines, Connecticut Siting Council, 2012.
37. M. H. Brown and R. P. Sedano, *Electricity Transmission: A Primer*, National Council on Electricity Policy, 2004.
38. *Transmission Projects: At a Glance*, Edison Electric Institute, 2015.
39. A. E. Power, *Transmission Facts*, 2013.

Publications

Velazquez, J. M.; **Saadi, F. H.**; Pieterick, A. P.; Spurgeon, J. M.; Soriaga, M. P.;
Brunschwig, B. S.; Lewis, N. S., Synthesis and Hydrogen-Evolution Activity of Tungsten
Selenide Thin Films Deposited on Tungsten Foils. *Journal of Electroanalytical
Chemistry* **2014**, *716*, 45-48.10.1016/j.jelechem.2013.11.030

Chmielowiec, B.; **Saadi, F. H.**; Baricuatro, J. H.; Javier, A.; Kim, Y.-G.; Sun, G.;
Darensbourg, M. Y.; Soriaga, M. P., Molecular Catalysis That Transpires Only When the
Complex Is Heterogenized: Studies of a Hydrogenase Complex Surface-Tethered on
Polycrystalline and (111)-Faceted Gold by Ec, Pm-Ft-Irras, Hreels, Xps and Stm. *Journal
of Electroanalytical Chemistry* **2014**, *716*, 63-70.10.1016/j.jelechem.2013.12.025

Baricuatro, J. H.; Kim, Y.-G.; **Saadi, F. H.**; McCrory, C. C. L.; Sanabria-Chinchilla, J.;
Crouthers, D.; Darensbourg, M. Y.; Soriaga, M. P., Heterogenization of a Water-
Insoluble Molecular Complex for Catalysis of the Proton-Reduction Reaction in Highly
Acidic Aqueous Solutions. *Electrocatalysis* **2014**, *5*, 226-228.10.1007/s12678-014-0200-
7

Carim, A. I.; **Saadi, F. H.**; Soriaga, M. P.; Lewis, N. S., Electrocatalysis of the
Hydrogen-Evolution Reaction by Electrodeposited Amorphous Cobalt Selenide Films.

Journal of Materials Chemistry A **2014**, *2*, 13835-13839.10.1039/C4TA02611J

Saadi, F. H.; Carim, A. I.; Velazquez, J. M.; Baricuatro, J. H.; McCrory, C. C.; Soriaga, M. P.; Lewis, N. S., Operando Synthesis of Macroporous Molybdenum Diselenide Films for Electrocatalysis of the Hydrogen-Evolution Reaction. *ACS Catalysis* **2014**, *4*, 2866-2873.10.1021/cs500412u

Saadi, F. H.; Carim, A. I.; Verlage, E.; Hemminger, J. C.; Lewis, N. S.; Soriaga, M. P., Cop as an Acid-Stable Active Electrocatalyst for the Hydrogen-Evolution Reaction: Electrochemical Synthesis, Interfacial Characterization and Performance Evaluation. *The Journal of Physical Chemistry C* **2014**, *118*, 29294-29300.10.1021/jp5054452

Soriaga, M. P.; Baricuatro, J. H.; Cummins, K. D.; Kim, Y.-G.; **Saadi, F. H.**; Sun, G.; McCrory, C. C.; McKone, J. R.; Velazquez, J. M.; Ferrer, I. M., Electrochemical Surface Science Twenty Years Later: Expeditions into the Electrocatalysis of Reactions at the Core of Artificial Photosynthesis. *Surface Science* **2015**, *631*, 285-294.10.1016/j.susc.2014.06.028

Sun, K.; **Saadi, F. H.**; Lichterman, M. F.; Hale, W. G.; Wang, H.-P.; Zhou, X.; Plymale, N. T.; Omelchenko, S. T.; He, J.-H.; Papadantonakis, K. M., Stable Solar-Driven Oxidation of Water by Semiconducting Photoanodes Protected by Transparent Catalytic Nickel Oxide Films. *Proceedings of the National Academy of Sciences* **2015**, *112*, 3612-

3617.10.1073/pnas.1423034112

Baricuatro, J. H.; **Saadi, F. H.**; Carim, A. I.; Velazquez, J. M.; Kim, Y.-G.; Soriaga, M. P., Influence of Redox-Inactive Cations on the Structure and Electrochemical Reactivity of Synthetic Birnessite, a Heterogeneous Analog for the Oxygen-Evolving Complex. *The Journal of Physical Chemistry C* **2015**.10.1021/acs.jpcc.5b07028

Zhou, X.; Liu, R.; Sun, K.; Friedrich, D.; McDowell, M. T.; Yang, F.; Omelchenko, S. T.; **Saadi, F. H.**; Nielander, A. C.; Yalamanchili, S., Interface Engineering of the Photoelectrochemical Performance of Ni-Oxide-Coated N-Si Photoanodes by Atomic-Layer Deposition of Ultrathin Films of Cobalt Oxide. *Energy & Environmental Science* **2015**, 8, 2644-2649.10.1039/C5EE01687H

Sun, K.; McDowell, M. T.; **Saadi, F. H.**; Zhou, X.; Lewis, N. S., Solar & Alternative Energy Protection of Small-Bandgap Semiconductors for Solar-Fuel Production. *SPIE* **2015**.10.1117/2.1201509.006124

Lichterman, M. F.; Sun, K.; Hu, S.; Zhou, X.; McDowell, M. T.; Shaner, M. R.; Richter, M. H.; Crumlin, E. J.; Carim, A. I.; **Saadi, F. H.**, Protection of Inorganic Semiconductors for Sustained, Efficient Photoelectrochemical Water Oxidation. *Catalysis Today* **2016**, 262, 11-23.10.1016/j.cattod.2015.08.017